

O. D. YILMAZ

PREDICTION OF SHEAR LOCALIZATION ONSET
IN MACHINING OF Ti-6Al-4V

THE GRADUATE SCHOOL OF NATURAL AND APPLIED SCIENCES
OF
ATILIM UNIVERSITY

OKAN DENİZ YILMAZ

A MASTER OF SCIENCE THESIS
IN
THE DEPARTMENT OF MANUFACTURING ENGINEERING

DECEMBER 2019

ATILIM UNIVERSITY 2019

PREDICTION OF SHEAR LOCALIZATION ONSET
IN MACHINING OF Ti-6Al-4V

A THESIS SUBMITTED TO
THE GRADUATE SCHOOL OF NATURAL AND APPLIED SCIENCES
OF
ATILIM UNIVERSITY

BY

OKAN DENİZ YILMAZ

IN PARTIAL FULFILLMENT OF THE REQUIREMENTS
FOR
THE DEGREE OF MASTER OF SCIENCE
IN
MANUFACTURING ENGINEERING

DECEMBER 2019

Approval of the Graduate School of Natural and Applied Sciences, Atilim University.

Prof. Dr. Ali Kara
Director

I certify that this thesis satisfies all the requirements as a thesis for the degree of **Master of Science in Manufacturing Engineering, Atilim University.**

Prof. Dr. Sadık Engin Kılıç
Head of Department

This is to certify that we have read the thesis PREDICTION OF SHEAR LOCALIZATION ONSET IN MACHINING OF Ti-6Al-4V submitted by OKAN DENİZ YILMAZ and that in our opinion it is fully adequate, in scope and quality, as a thesis for the degree of Master of Science.

Prof. Dr. Sadık Engin Kılıç
Co-Supervisor

Asst. Prof. Dr. Samad Nadimi Babil Oliaei
Supervisor


Examining Committee Members:

Asst. Prof. Dr. Shahram A. Dizaji
Mechanical Engineering, Ted University

Asst. Prof. Samad Nadimi Babil Oliaei
Mechanical Engineering, Atilim University

Asst. Prof. Dr. Bahram Lotfiasadigh
Manufacturing Engineering, Atilim University

Date: 27.12.2019



I hereby declare that all information in this document has been obtained and presented in accordance with academic rules and ethical conduct. I also declare that, as required by these rules and conduct, I have fully cited and referenced all material and results that are not original to this work.

Name, Last Name : Okan Deniz Yılmaz

Signature :

ABSTRACT

PREDICTION OF SHEAR LOCALIZATION ONSET IN MACHINING OF Ti-6Al-4V

Yılmaz, Okan Deniz

MsD., Department of Manufacturing Engineering

Supervisor : Asst. Prof. Samad Nadimi Babil Oliaei

Co-Supervisor : Prof. Dr. Sadık Engin Kılıç

December 2019, 83 pages

Application of lightweight and energy-saving materials plays a significant role in different industries including automotive, aerospace and biomedical, to name a few. One important lightweight material is Ti-6Al-4V titanium alloy known as the working-horse of the titanium industry, because of its excellent chemical and mechanical properties. In spite of its widespread applications, Ti-6Al-4V is known as a difficult-to-cut material because of its low thermal conductivity, its high chemical affinity with most cutting tool materials, low modulus of elasticity and the formation of shear localized (serrated) chips during machining. The latter is of paramount importance, because of the fact that the consequences of the emergence of serrated chip formation in machining are fluctuations in the machining forces, accelerated tool wear, deterioration of the surface quality, reduced accuracy and out-of-tolerance machined components. The prediction of the onset of shear localization is one of the most challenging problems in the field of machining, i.e. determining the conditions in which the chip morphology is changing from continuous to a periodically varying. The issues associated with shear localized chips were the main driving force in the literature for the development of several material models for the simulation of shear

localization during machining of Ti-6Al-4V titanium alloy. However, the accuracy and capability of the developed models for the prediction of the onset of serrated chip formation during machining Ti-6Al-4V have not been investigated. The aim of this thesis is to evaluate the accuracy of different material models to predict the onset of serrated chip formation during the machining of Ti-6Al-4V. The results of the finite element models are compared with the results of the experiments in terms of machining forces and chip morphology. Ploughing forces are obtained by varying uncut chip thickness at different cutting speeds by using the extrapolation method, and are used to correct cutting and thrust forces. Corrected cutting and thrust forces are used to calculate the Coulomb friction coefficient. Both explicit and implicit finite element codes are used with different material models with/without damage, with/without strain softening. The weakness and strength of each material model have been investigated for the prediction of the critical cutting speed, chip morphology and machining forces. The results of this study revealed that a modified Johnson-Cook material model which includes temperature softening and strain softening in the form of the hyperbolic tangent function is able to give acceptable predictions for the onset of shear-localization during machining of Ti-6Al-4V.

Keywords: Ti-6Al-4V, Machining, Finite Element Method, Shear Localization, Damage.

ÖZ

Ti-6Al-4V İŞLENMESİNDE KESME LOKALİZASYONU BAŞLANGICININ TAHMİNİ

Yılmaz, Okan Deniz

Yüksek Lisans, İmalat Mühendisliği Bölümü

Tez Yöneticisi : Dr. Öğr. Üyesi Samad Nadimi Babil Oliaei

Ortak Tez Yöneticisi : Prof. Dr. Sadık Engin Kılıç

Aralık 2019, 83 sayfa

Hafif ve enerji tasarrufu sağlayan malzemelerin kullanılması otomotiv, havacılık ve biyomedikal vb. gibi farklı endüstrilerde önemli bir rol oynamaktadır. Mükemmel kimyasal ve mekanik özelliklerinden dolayı önemli bir hafif malzeme olan Ti-6Al-4V titanyum alaşımı, titanyum endüstrisinin çalışma atı olarak bilinir. Yaygın olarak kullanılmasına rağmen, Ti-6Al-4V düşük ısı iletkenliği, çoğu kesici alet malzemesiyle yüksek kimyasal afinitesi, düşük esneklik katsayısı ve kesme sırasında lokalize (tırtıklı) talaşların oluşumu nedeniyle kesilmesi zor bir malzeme olarak bilinir. Daha sonra, talaşlı imalatta tırtıklı talaş oluşumunun ortaya çıkması, işleme kuvvetlerindeki dalgalanmalarla, hızlandırılmış takım aşınmasıyla, yüzey kalitesinin bozulmasıyla, hassasiyetin azalmasıyla ve parçaların tolerans dışı işlenmesiyle sonuçlanacağından büyük önem taşır. Kesme lokalizasyonunun başlangıcını öngörme, talaş imalat alanındaki en zorlu sorunlardan biridir, yani talaş morfolojisinin sürekli talaştan değişen bir morfolojiye periyodik olarak değiştiği koşulları belirler. Literatürdeki kesme lokalize talaşları ile ilgili konular, Ti-6Al-4V titanyum alaşımının işlenmesi sırasında kesme lokalizasyonu oluşumunun simülasyonu için çeşitli malzeme modellerinin geliştirilmesinde ana itici güç olmuştur. Bununla birlikte, geliştirilen

modellerin Ti-6Al-4V işleme sırasında tırtıklı talaş oluşumunun başlangıcını öngörme doğruluğu ve kabiliyeti araştırılmamıştır. Bu tezin amacı, Ti-6Al-4V işleme sırasında tırtıklı talaş oluşumunun başlangıcını tahmin etmek için farklı malzeme modellerinin doğruluğunu değerlendirmektir. Sonlu eleman modellerinin sonuçları işleme kuvvetleri ve talaş morfolojisi açısından deney sonuçları ile karşılaştırılmıştır. Kazma kuvveti kesilmemiş talaş kalınlığı değiştirilerek farklı kesim hızlarında ekstrapolasyon yöntemi kullanılarak elde edilir ve kesme ve itme kuvvetlerini düzeltmek için kullanılır. Düzeltilmiş kesme ve itme kuvvetleri, Coulomb sürtünme katsayısını hesaplamak için kullanılır. Hem belirli hem belirsiz sonlu eleman kodları, deformasyon yumuşaması veya yumuşamasız, hasara sahip veya hasarsız, farklı malzeme modelleriyle kullanılmıştır. Her malzeme modelinin zayıflığı ve gücü, kritik kesme hızı, talaş morfolojisi ve işleme kuvvetlerinin tahmin edilebilmesi için araştırılmıştır. Bu çalışmanın sonuçları gösteriyor ki, hiperbolik teğet fonksiyonu formunda sıcaklık ve gerinim yumuşatma içeren değiştirilmiş Johnson-Cook malzeme modelinin, Ti-6Al-4V'nin işlenmesi sırasında kesme lokalizasyonunun başlangıcı için kabul edilebilir bir tahmin verebileceğini ortaya koydu.

Anahtar Kelimeler: Ti-6Al-4V, Talaşlı İmalat, Sonlu Elemanlar Metodu, Kesme Lokalizasyonu, Hasar.



To my Family...

ACKNOWLEDGMENTS

First of all, I would like to express my gratitude to my advisor, Asst. Prof. Dr. Samad Nadimi Babil Oliaei for the support of my M.Sc study, for his patience, motivation and noticeable knowledge. His supervision and assistance helped me in all the time of research and writing of this thesis. Without his supervision and assistance, I would definitely not be able to accomplish this thesis successfully. Besides, I would like to thank the rest of my thesis committee, Asst. Prof. Dr. Shahram A. Dizaji and Asst. Prof. Dr. Bahram Lotfisdigh, for their insightful comments.

The help of Prof. Dr. Sadık Engin Kılıç, Prof. Dr. Bilgin Kaftanoğlu and Dr. Şakir Baytaroğlu is also acknowledged.

Thanks to the powerful technical facilities of Atılım University Manufacturing Laboratory, Bilkent University Microsystem Design and Manufacturing Center and National Nanotechnology Research Center (UNAM) of Bilkent University, this thesis could be fulfilled easily. I felt myself a very privileged person for having the technical assistance of our technician Bülent Aydoğan and Özdemir Dinç. I am very thankful to them for all of the contributions they made.

I shall also thank my friends at Bilkent University and Atılım University, Hatice Dilara Uslu, Ramazan Hakkı Namlu and Alp Yalçın for their worthwhile and excellent times we shared.

Last but not least, I would like to thank my family for their support throughout the course of my master thesis and my life in general.

TABLE OF CONTENTS

ABSTRACT	iii
ÖZ	v
ACKNOWLEDGMENTS	viii
LIST OF TABLES	xi
LIST OF FIGURES	xii
CHAPTER 1	1
1. INTRODUCTION	1
1.1 Finite Element Modeling of the Machining Process	1
1.2 Serrated Chip Formation in Ti-6Al-4V	3
1.3 Mechanism of Shear Deformation zone in Ti-6Al-4V	7
CHAPTER 2	8
2. LITERATURE REVIEW.....	8
2.1 Critical Cutting Speed of Ti-6Al-4V	8
2.2 Mechanism of Shear Deformation zone in Ti-6Al-4V	9
2.3 Experimental Aspect of Shear Localization of Chip Segmentation in Ti-6Al-4V	14
2.4 Computational Simulation of Shear Localization in Ti-6Al-4V	17
CHAPTER 3	20
3. MODELING OF MACHINING SIMULATION OF Ti-6Al-4V BASED ON FINITE ELEMENT APPROACH	20
3.1 Finite Element Modeling	20
3.2 Finite Element Modeling Procedure	21
3.3 Material Models	23
3.4 Friction Modeling	43
CHAPTER 4	45
4. EXPERIMENTAL PROCEDURE AND STUDIES	45

4.1	Edge radius of the original inserts and modified inserts for Friction modeling	45
4.2	Experimental Procedure for Orthogonal Cutting Experiments.....	49
4.3	Influence of Ploughing Cutting and Thrust Force on Coulomb Friction Coefficient	52
4.4	Finite Element Simulation of Critical Cutting Speed of Ti-6Al-4V	57
4.5	Temperature and Force Comparison between FEM and Measured Data	69
CHAPTER 5		76
5.	CONCLUSION	76
REFERENCES.....		78

LIST OF TABLES

TABLES

Table 3.2.1 Thermal and mechanical properties of the tungsten carbide.....	22
Table 3.2.2 Temperature dependent material properties.....	22
Table 3.3.1 Parameters of Johnson-Cook Material Model	24
Table 3.3.2 Parameters of Calamaz (TANH) material Model [4].....	27
Table 3.3.3 Parameters of Modified Material Sima&Ozel Model I, II and III [49] ..	34
Table 3.3.4 Parameters of Yigit Karpat Modified JC Material Model [47].....	36
Table 3.3.5 Thermal softening and damage parameters of Power Law [5]	39
Table 3.3.6 Johnson-Cook damage parameters	40
Table 3.3.7 Parameters of KHL Constitutive Material Model [63]	41
Table 3.3.8 Parameters of Modified KHL Constitutive Material Model.....	42
Table 4.2.1 The experimental conditions of orthogonal cutting experiments.....	49
Table 4.3.1 The experimental conditions of orthogonal cutting experiments.....	52
Table 4.3.2 Coulomb Friction Coefficient using modified inserts with 0°, 4° and 8° rake angle at Cutting Speed of 1 and 40 m/min	56
Table 4.4.1 Summary of the capability and accuracy of different constitutive material models	67

LIST OF FIGURES

FIGURES

Figure 1.2.1 Schematic view of orthogonal cutting	4
Figure 1.2.2 Microscope images of the alpha and beta phases of Ti-6Al-4V alloy.....	5
Figure 2.2.1 Stress&Strain Diagram, Isothermal Hardening, Thermal and Strain Softening	13
Figure 3.1.1 Inputs of the finite element model of the machining.....	20
Figure 3.2.1 Representation of initial boundary conditions of Finite element model	23
Figure 3.3.1 Stress&Strain curves at Strain rate 1 s^{-1} , Temperature $25 \text{ }^{\circ}\text{C}$ using all parameters at Table 3.1	25
Figure 3.3.2 Stress&Strain curves at Strain rate 10^5 s^{-1} and Temperature $500 \text{ }^{\circ}\text{C}$	25
Figure 3.3.3 Stress&Strain curves at Strain rate $2 \times 10^3 \text{ s}^{-1}$ using Johnson and Holmquist parameter [54]	26
Figure 3.3.4 Stress&Strain curves at Temperature $500 \text{ }^{\circ}\text{C}$ using Johnson and Holmquist parameter [54]	26
Figure 3.3.5 Stress&Strain curves for Johnson-Cook (JC) and Calamaz (TANH) model at temperature 598K , strain rate of 10^4 s^{-1} [4].....	28
Figure 3.3.6 Stress&Strain curves for Johnson-Cook (JC) and Calamaz (TANH) model at a strain rate of 10^4 s^{-1} [4]	28
Figure 3.3.7 Stress&Strain curves for J-C and Exponential-Calamaz ($f=0$) model at a strain rate of 10^5 s^{-1} [61].....	30
Figure 3.3.8 Stress&Strain curves for J-C and Exponential-Calamaz ($f=0.05$) model at a strain rate of 10^5 s^{-1} [61]	30
Figure 3.3.9 Stress&Strain curves for J-C and Calamaz-Exponential ($f=0.11$) model at a strain rate of 10^5 s^{-1} [61]	31
Figure 3.3.10 Stress&Strain curves for J-C and Calamaz-Exponential ($f=0.22$) model at a strain rate of 10^5 s^{-1} [61].....	31
Figure 3.3.11 Stress&Strain curves for Modified JC Material Sima&Ozel Model I at different temperature and strain rate [49].....	32

Figure 3.3.12 Stress&Strain curves for Modified JC Material Sima&Ozel Model II at different temperature and strain rate [49].....	34
Figure 3.3.13 Stress&Strain curves for Modified JC Material Sima&Ozel Model III at different temperature and strain rate [49].....	35
Figure 3.3.14 Stress&Strain curves of Yigit Karpat material model at a strain rate of 10^5 s^{-1} and different temperatures [47].....	37
Figure 3.3.15 Stress&Strain curves of at a strain rate of $2 \times 10^3 \text{ s}^{-1}$ and different temperatures [5]	38
Figure 3.3.16 Stress&Strain curves for KHL Model at different temperature and strain rate [63]	41
Figure 3.3.17 Stress&Strain curves for Modified KHL Model at different temperature and strain rate [63]	43
Figure 4.1.1 Edge radius measurement of the original insert [3].....	45
Figure 4.1.2 Edge radius measurement of the 0° rake insert after edge preparation .	46
Figure 4.1.3 Edge radius measurement of the 4° rake insert after edge preparation .	47
Figure 4.1.4 Edge radius measurement of the 8° rake insert after edge preparation .	48
Figure 4.2.1 The experimental setup used for orthogonal cutting experiments.....	49
Figure 4.2.2 Chip cross section obtained at a cutting speed of 2.82 m/min.....	51
Figure 4.2.3 Chip cross section obtained at a cutting speed of 40 m/min.....	51
Figure 4.3.1 Extrapolated Cutting and Thrust Forces versus Uncut Chip Thickness with 0° rake angle modified insert, Cutting Speed 40 m/min	52
Figure 4.3.2 Measured Cutting (blue) and Thrust Forces (pink) versus Uncut Chip Thickness (0.05, 0.75, 0.1 and 0.15) with 0° rake angle insert, $V_c = 1 \text{ m/min}$	53
Figure 4.3.3 Measured Cutting (blue) and Thrust Forces (pink) versus Uncut Chip Thickness (0.05, 0.75, 0.1 and 0.15) with 0° rake angle insert, $V_c = 40 \text{ m/min}$	53
Figure 4.3.4 Measured Cutting (blue) and Thrust Forces (pink) versus Uncut Chip Thickness (0.05, 0.75, 0.1 and 0.15) with 4° rake angle insert, $V_c = 1 \text{ m/min}$	54
Figure 4.3.5 Measured Cutting (blue) and Thrust Forces (pink) versus Uncut Chip Thickness (0.05, 0.75, 0.1 and 0.15) with 4° rake angle insert, $V_c = 40 \text{ m/min}$	54
Figure 4.3.6 Measured Cutting (blue) and Thrust Forces (pink) versus Uncut Chip Thickness (0.05, 0.75, 0.1 and 0.15) with 8° rake angle insert, $V_c = 1 \text{ m/min}$	55

Figure 4.3.7 Measured Cutting (blue) and Thrust Forces (pink) versus Uncut Chip Thickness (0.05, 0.75, 0.1 and 0.15) with 8° rake angle insert, $V_c = 40$ m/min	55
Figure 4.4.1 Johnson-Cook material model result at a high cutting speed of 120 m/min	58
Figure 4.4.2 FEM results using MJ-C model proposed by Calamaz et al. [4].....	59
Figure 4.4.3 FEM results using MJ-C model proposed by Sima&Ozel Model I [49]	60
Figure 4.4.4 FEM results using MJ-C model proposed by Sima&Ozel Model II [49]	61
Figure 4.4.5 FEM results using MJ-C model proposed by Sima&Ozel Model III [49]	62
Figure 4.4.6 FEM results using MJ-C model proposed by Karpat [47].....	63
Figure 4.4.7 FEM results using Power-law material model with temperature-dependent damage: 0.1 and 40 m/min [5]	64
Figure 4.4.8 J-C model with Cockcroft and Latham material failure model result at low cutting speed.....	65
Figure 4.4.9 Johnson-Cook Material Model with J-C damage results.....	66
Figure 4.4.10 The results of FE simulations for different uncut chip thicknesses using MJ-C model proposed by Sima&Ozel model II: Uncut chip thickness of 0.075 mm	68
Figure 4.4.11 The results of FE simulations for different uncut chip thicknesses using MJ-C model proposed by Sima&Ozel model II: Uncut chip thickness of 0.125 mm	69
Figure 4.5.1 Temperature and Force Distribution Graph of YK, Calamaz d1, Calamaz d1.5, Ozel Model1, Ozel Model2, Ozel Model3, Power Law, JC-JC Damage, JC C&L90 and JC C&L240 (top to bottom)	74
Figure 4.5.2 Measured Thrust Forces at $f=0.1$ mm/rev and $V_c = 40$ m/min with 0° rake, 7° Clearance and 5 micrometer inserts	75

CHAPTER 1

1. INTRODUCTION

1.1 Finite Element Modeling of the Machining Process

Modeling and simulation of machining processes are helpful to better understand the process mechanisms and are useful to select proper machining process parameters. The metal cutting operation is related to the mechanical friction, heat generation due to friction and plastic deformation, high plastic strains in the cutting area and large strain rates. These challenging factors are limiting the theoretical models of chip formation. Studies are mostly focusing on computer simulation and modeling of metal cutting to solve unexpected problems arising in the improvement of the technology. Finite element simulations would kindly complement our understanding of the cutting process and help us to design better cutting tools, choose better machining process parameters and improve machinability. Finite element analysis is a pre-defined numerical approximation to understand the response of a continuum to an external such as pressure and heat. The FEM of machining operations requires an accurate definition of different aspects of the process, including machining process parameters, cutting tool parameters, contact conditions and solution method.

The modeling starts with the generation of a constitutive material model of the workpiece and tool which followed by a numerical approximate solution of this theoretical model. The idea of the finite element modeling involves dividing workpiece and tool into a set of divided mesh domains which is known as a mesh element. After that, numerical solution methods are helping to solve each mesh element and to apply the matrix of the solution to the entire geometry to obtain the solution of the main problem. Briefly, FEM is one the way to solve intricate problems that are very difficult or even impossible to be solved using analytical methods. The finite element solution has three steps, pre-processing, processing and post-processing. Pre-processing includes the preparation of coordinates, connection points, boundary conditions, forces and material properties.

The processing part includes the solution of equations and stiffness factors that result in variables. The last step is post-processing that methods give an image of deformed geometry and the solution to the problem. Temperature, stress, strain and force, etc. can be found at this step. The final solution is a mathematical interaction of these three steps.

One of the main benefits of numerical modeling of the cutting process is the availability of a wide range of personal computers (PCs) and workstations to handle the modeling of complex cutting problems. Moreover, material properties can be well-defined as a function of temperature, strain and strain rate. The contact surface between the workpiece and tool can be modeled as sliding and sticking. Cutting and thrust forces, chip morphology, stress, strain, strain rate and temperature can be predicted with acceptable accuracy. FEM has been widely used to model the metal cutting processes since the beginning of 1970 [1]. Various commercial software programs are developed to simulate cutting processes such as ABAQUS [2], DEFORM 2D/3D [3], FORGE 2D [4], AdvantEdge [5], etc. This software implements different algorithms for the simulation of machining operations. Some are based on the implicit formulation (DEFORM 2D/3D) and some of them are explicit (ABAQUS).

One of the challenging issues of metal cutting, where the finite element has been used widely, is the shear localization phenomena, which is shown to appear at titanium and its alloys, Inconel, aluminum alloys and steels [2]. Among these materials, more studies are focused on the modeling of serrated chip formation of titanium alloy Ti-6Al-4V, because of its importance and widespread application in different industries such as aerospace, automotive, biomedical, etc. The studies are largely focused on the shear localization phenomena, while there are very limited works devoted to the prediction of the onset of shear localization, where the geometry of the chip changes from continuous to a shear localized (serrated) type. In this thesis, an attempt has been made to study the onset of serrated chip formation using finite element analysis, with a focus on the effect of different material models on the prediction of the onset of serrated chip formation. The aim is to understand the capability, strength and weaknesses of different material models in predicting the onset of shear localization. The results of finite element models are compared with the experimental data, in terms of chip morphologies and machining forces.

1.2 Serrated Chip Formation in Ti-6Al-4V

Metal cutting is known as a secondary manufacturing process, where the unwanted material is removed in the form of chips to turn the stock material into the desired workpiece. The basic theory behind the metal cutting process is related to force, strain, strain rate, temperature, tool wear, tool clearance and rake angle. Metal cutting procedures like drilling, milling, boring, turning, grinding, reaming and all others are metal removing processes and produces continuous, discontinuous and serrated chips. Therefore, investigation of the chip formation can give a chance to understand the theory of metal cutting machining mechanics. Concentrated defect slips over a shear plane. The deformation of the material occurs when a point on the workpiece reaches the shear plane and passes through the primary deformation zone. When metal crosses the thin shear zone, it then undergoes a significant amount of basic shear. When the chip begins to proceed up along the tool, there isn't require any plastic flow. A small clearance angle of the tool is always better to avoid surface damage to the workpiece. There is a common surface between the rake face of the tool and workpiece, where chip flow occurs. This surface has a contact length of (l_c). The tool is moving in the feed direction with a specific velocity which is known as cutting speed (V_c). The schematic view of orthogonal cutting can be seen in Figure 1.2.1.

The local deformation in the workpiece, which is being cut by the tool results in severe plastic deformation of the uncut chip (t) that continues to become deformed chip thickness t_c . Undeformed chip is also known as a feed. The cutting force F_c proceeds in the direction of cutting speed which is also known as feed force. The thrust force (F_t) is defined as a force that is normal to the direction of the cutting velocity. Ti-6Al-4V which is the most widely used titanium alloy has found widespread applications in different industries including biomedical, aerospace and defense. Properties such as low thermal conductivity and higher chemical reactivity with cutting tool materials make Ti-6Al-4V a difficult-to-cut material. One important observation during machining this alloy is the formation of serrated chips also known as segmented chips or saw-toothed chips.

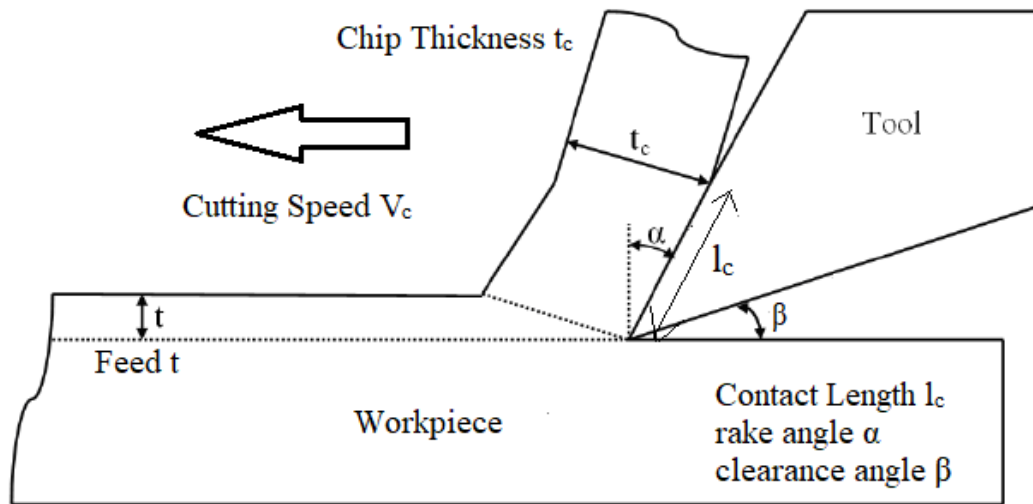


Figure 1.2.1 Schematic view of orthogonal cutting

The presence of serrated chips results in fluctuations in the cutting forces, accelerated tool wear and it can alter the quality of the machined surface [6]. The observations reveal that there is an agreement between the segmentation frequency of the chips and the fluctuation frequency of the cutting forces [7]. Although usage of Ti-6Al-4V increased, they are not cost-effective yet when compared to other mostly used metals because the melting temperature of Ti-6Al-4V is high and there are so many problems that occur when the processing of this material by different manufacturing techniques. To increase the production efficiency along with reducing the manufacturing costs, it is crucial to comprehend mechanical behavior and microstructural analysis. The main difference of Ti-6Al-4V from other titanium alloys is its basic metallurgical characteristics that contain α and β phase while other titanium alloys don't contain these two phases at the same time. Therefore, titanium alloys can be categorized by α -titanium alloys, near α -titanium alloys, α - β titanium alloys, and β -titanium alloys [8].

The α -titanium alloy contains α stabilizers such as aluminum and Tin. Clearly, its microstructure contains mostly α phase that is why it is known as single-phase α -alloy and commercially pure titanium. The α -alloy titanium has superior mechanical properties and creep stability between 25 °C to 300 °C. It is mainly used for corrosion resistance and cryogenic practices. The near α -alloy titanium contains mostly α stabilizers but limited quantities of β stabilizers affect materials microstructures. Ti-2.5Cu, Ti-5Al-2.5Sn, Ti-8Al-1V-1Mo, Ti-6242, Ti-6Al-2Nb-1Ta-0.8 Mo and Ti-5Al-5Sn-2Zr-2Mo can be classified as near α -alloy titanium. The near α -alloy titanium has

similar mechanical properties with α -alloy but they have better creep stability that can operate at higher temperatures of 400 °C to 520 °C.

The α - β alloy contains a mixture of α stabilizers and β stabilizer. Its microstructure can be seen as the α phase fused with the β phase in contact. There is a chance to the heat-treated α - β alloy to strengthen more levels so they can be mostly used for critical applications at temperatures of between 350 °C to 400 °C. Ti-6Al-4V, Ti-6Al-6V-2Sn, Ti-6Al-2Sn-2Zr-2Cr-2Mo, Ti-3Al-2.5V and Ti-8Al-1Mo-1V are mostly known commercially as α - β alloys. The β alloy titanium contains a remarkable amount of β stabilizers such as vanadium, chromium and copper and their better surface hardness, cold formability capabilities, forging, density abilities differ them from other titanium alloys. These β alloys behave mostly the same with α - β alloys at room temperature but they are not superior then α - β alloys at higher temperatures. This Ti-6Al-4V specimen is one of the chips collecting from orthogonal machining experiments. Chips are mounted polymer disk and prepared to see alpha and beta phases of Ti-6Al-4V that can be seen in Figure 1.2.2. It might be specified as beta phases are darker than the alpha phases.

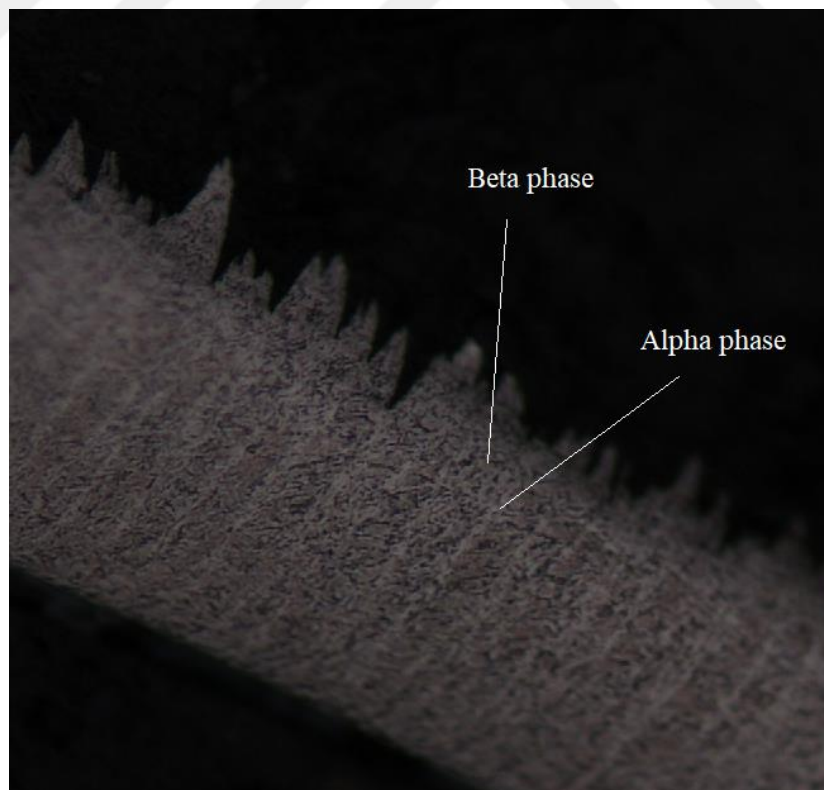


Figure 1.2.2 Microscope images of the alpha and beta phases of Ti-6Al-4V alloy

In Ti-6Al-4V, α and β phases are all solid in titanium solutions. Ti-6Al-4V solution contains a maximum 0.2% percent oxygen (O) atom, a maximum 0.25% percent Iron (Fe) atom, 6% percent aluminum (Al) and 4% percent Vanadium (V) and all other various impurity atoms involving quite small quantities. At 25 °C ambient temperature, the stabilized β phase includes more vanadium (V) than normal 4% percent. At elevated temperature 527 °C, stabilized α phase begins to transform the β phase, after 980 °C temperature reach, the microstructure is all formed of β equiaxed grain structures. The flow stress of Ti-6Al-4V relies on temperature and strain rate extremely [9]. The kinetic and mechanic behavior of α and β phases are different. This results in unpredictable a large number of deformation mechanisms.

Machinability can be defined as a difficulty or easiness with which a material can be cut under specific cutting parameters like feed, uncut chip thickness and cutting speed. The machinability of Ti-6Al-4V has not made usual progress in advanced manufacturing progress but steel, copper and aluminum, etc. metals take a better pace in the manufacturing process and get an enormous amount of machinability chance. Since titanium alloys represent high chemical affinity against all tool materials which cause rapid tool wear at high cutting speeds. Their low thermal conductivity increases the temperature of the tool/workpiece interface which leads to decrease tool life dramatically. Its high melting temperature and low thermal conductivity decrease machinability because it does not soften thermally. Its low elastic modulus deflects workpiece easier and this leads to chatter, tool contact difficulties, and unsatisfactory dimensional tolerances. Vibration is another factor in machining Ti-6Al-4V that decrease material removal rate and increase surface roughness. The maximum cutting speed of titanium alloys is 30 m/min with HSS tool and 60 m/min tungsten carbide tool this is one of the reasons why titanium alloys are difficult to cut material. Most popular other tool materials such as tungsten carbide, cubic boron nitride (CBN) and single/polycrystalline diamond have a high chemical affinity with Ti-6Al-4V and they face wear issues during machining of titanium alloys. Titanium alloys can be machined by using low cutting speed, providing high feed, applying high flow rate coolant flow and tool with specific coating.

1.3 Mechanism of Shear Deformation zone in Ti-6Al-4V

One of the most challenging problems in the field of machining is to determine the onset of serrated chip formation, where the chip morphology is changing from continuous to a periodically varying (cyclic) saw-tooth like [10] [11] [12] [13], also named as segmented chip [14], serrated chip [12] [14], catastrophic shear-type chip [15] or shear localized chip [16]. The periodicity is shown to be affected by the cutting speed, whereby decreasing the cutting speed the nature of the chip changes from periodic (ordered) to aperiodic (disordered) [17]. It is also found out that thermo-mechanical behavior of workpiece tool interaction obviously has an effect on the chip morphology which in turn mostly influence tool life and work piece dimensional tolerances. Chip morphology is generally formed in materials with poor thermal properties and those having limited slip systems (such as hcp metals) and in materials with temperature dependent flow stress due to phase transformation and possible changes in the crystallographic structure [6]. The consequences of the emergence of serrated chip formation in machining could be an accelerated tool wear, deterioration of the surface quality and lowering the accuracy of the of the machined components. Taking into account the effect of serrated chip formation on the cutting performance and its close relationship with tool life, cutting temperature, and fluctuations in the cutting forces along with plastic strain localization, an in-depth understanding of this phenomenon seems to be quite significant for better understanding of the encountered phenomena.

The chip formation mechanism of machining Ti-6Al-4V was discovered to be not the same as the continuous chip formation [18]. Built edge formation on tool edge occurs usually due to adiabatic shearing which results in thermos-mechanical instability. Adiabatic shear is frequently the same as unstable machining was indicated by Recht [19] who found out the thermal softening rate outperforms the strain hardening rate. Damage models and crack formation process theories have represented to explain the cutting mechanism of Ti-6Al-4V which is only feasible at low cutting speeds. FEM simulations of Ti-6Al-4V give a chance to understand deeply mechanism of chip morphology and formation of a chip in detail.

CHAPTER 2

2. LITERATURE REVIEW

2.1 Critical Cutting Speed of Ti-6Al-4V

The onset of serrated chip formation is poorly understood despite extensive studies in the field of metal cutting [20]. Therefore, it is of significant importance to determine the critical conditions for the onset of serrated chip formation to improve productivity, part dimensional accuracy and overall efficiency of the machining process [16] [21]. Although analytical models can be considered as an effective method of studying metal cutting operations, however because of very complex phenomena involved in the machining and their strong interactions such as friction at tool/chip and tool/workpiece interfaces, cutting tool micro geometry and material behavior, analytical models rarely reflect the actual machining conditions. For instance, Xie et al. [22] defined a flow localization parameter (β) to judge the onset of shear localization as a function of material parameters and cutting conditions (cutting speed and feed). They obtained a critical flow localization parameter of 4.41 for Ti-6Al-4V for a material removal rate of 0.004 m²/min. They considered a power-law relation to express shear stress as a function of shear strain, shear strain rate and temperature, which may not reflect the material properties on some occasions. Additionally, their relationship does not incorporate cutting tool micro geometry (for instance cutting edge radius) to calculate flow localization parameter. To capture more details of the complex cutting processes, numerical methods such as finite element modeling are widely used in the literature. According to Recht, the catastrophic shear occurs when the rate of decreasing in the flow stress of the material due to thermal softening becomes higher than the rate of increase in the flow stress due to work hardening in the primary shear zone [19]. Consequently, the deformation will be localized. This catastrophic condition is called an adiabatic slip. When the edge radius becomes comparable to the uncut chip thickness it can result in a more extensive shear zone [23]. The earlier theories on the mechanism of serrated chip formation introduced two different mechanisms of serrated chip formations depending on the type of material being machined [11]. One mechanism relies on the overstraining of the material under compressive stresses

which are called ductile fracture mechanisms and the other was associated with the strain concentration due to thermal softening which is termed as a high-speed ductile fracture. Later, the serrated chip formation has been described by two refined theories, where the first theory expresses that its formation is because of a thermos-plastic instability (Adiabatic shear instability) [16] [17], while the second theory is based on crack formation and propagation within the primary deformation zone [20] [21].

So far there is no study in the literature that compares the accuracy of different developed models to predict the onset of serrated chip formation during machining titanium alloy Ti-6Al-4V. The damage model proposed by Cockcroft and Latham [24] proposes that damage initiation depends on the maximum principal stress rather than generalized stress damage criterion has been used by Ceretti et al. [25] to model serrated chip formation. This criterion can be expressed as:

$$\int_0^{\varepsilon_f} \sigma^* d\bar{\varepsilon} = C$$

where C is the critical value at fracture, σ^* is the maximum principal tensile stress, ε_f is a strain at fracture and $\bar{\varepsilon}$ is the effective strain. In this damage model, parameter C depends on material only and is independent of stress-strain history [26]. For finite element modeling of machining, it is assumed that the critical damage value is constant and it is independent of cutting conditions. On the other hand, Zhen-Bin and Komanduri [27] reported that the critical cutting speed for serrated chip formation is about 9 m/min and the thermal instability may occur above that speed. Most of the research revealed that large plastic deformation causes a highly increase dislocation in the microstructure of the workpiece [28]. Pettersen [29] revealed that if there is grain size change due to flow stress, it increases grain boundary while increasing strain. According to Ding and Guo [30], the recrystallization of Ti-6Al-4V is more apparent when the workpiece material exposes higher strains.

2.2 Mechanism of Shear Deformation zone in Ti-6Al-4V

Finite element simulation of the machining process has studied to overcome the issue of a shear localized, discontinues and continuous chip formation for mesh element separation. Numerous research for shear localized chip formation revealed that maximum shear and principal stress, effective strain and catastrophic shear failure

criterion have been found by using finite element simulation in pretty close matching results. Saw-tooth appearance chips are occurring due to shear localization during machining [22].

The flow localization parameter is highly correlated with cutting conditions such as feed and speed. It can be defined as:

$$F_l = -\frac{\sqrt{3}}{m} \left[\frac{n}{\gamma} + \frac{0.9 \left(\frac{\partial \tau}{\partial T} \right)}{\rho c \left(1 + 1.328 \sqrt{\frac{K_1 \gamma}{V_f}} \right)} \left(n + 1 - \frac{0.664 \sqrt{\frac{K_1 \gamma}{V_c f}}}{1 + 1.328 \sqrt{\frac{K_1 \gamma}{V_c f}}} \right) \right]$$

where m is strain rate parameter, n is strain hardening, K_1 is thermal diffusivity of the workpiece, γ is a shear strain and T is temperature. The feed is defined as f and cutting speed V_c which are highly related to shear localization of chip formation. Flow localization can be used to find out where is localized strain concentration in the material. In order to form the onset of shear localization, strain value must exceed the critical limit. The equation given above can use as a predicting onset of shear localization for specific cutting conditions. Flow localization increases when cutting speed and feed both increases that are meaning that flow localization is linear dependent with feed and cutting speed. Flow localization parameter is found out experimentally that is nearly equal 4.41 and shear banding is possible with these values. The formation of the shear localized chip is linearly dependent with thermal diffusivity, density, strain rate, strain hardening, thermal conductivity and heat capacity. Clearly, when the cutting speed reaches a certain limit then shear localization occurs, the plastic strain rate exceeds the specific limit so tool/workpiece contact friction becomes heavier which results in high heat generation. The machining process might result in adiabatic conditions due to excessive temperature values which soften more the workpiece in local areas. The result of this, thermal softening decreases the effect of strain hardening so the cutting instability appears in the local area of the chip. Therefore, flow localization might be used as a function that gives a chance to calculate and predict the shear localized area.

Ceretti et al. suggested a new damage model based on the Cockcroft and Latham for fracture mechanism [24] [25]. According to their damage model, the damage can be calculated by:

$$C_i = \int_0^{\varepsilon_f} \bar{\sigma} \left(\frac{\sigma^*}{\bar{\sigma}} \right) d\bar{\varepsilon}$$

ε_f is the fracture strain, σ^* is the maximum principal stress. This equation calculates the critical damage (C_i) for each mesh element of the workpiece after that, Cockcroft and Latham damage model predicts the damage and separation.

Hashemi et al. [31] proposed a fracture mechanical model for simulation segmented chip formation and breaking during orthogonal cutting. This model calculates all the stress at each mesh element in the simulation. If the numerical value of stress exceeds the critical point, then they are assuming that crack propagates along the direction normal to the stress tensor. Critical stress can be found by using material fracture strength.

Obikawa and Usui suggested a strain based on the fracture model for serrated chip formation in material modeling of orthogonal cutting Ti-6Al-4V [32]. They claimed that when any mesh element exceeds the material fracture strength, it breaks from the whole which means the crack is propagating. They also indicated that the reason for the serrated chip is related to ductile cracks propagating from the chip surface while machining of Ti-6Al-4V or titanium alloys. Their material fracture model is defined by:

$$\varepsilon_c = -\max \left[\left(0.075 \ln \frac{\varepsilon^{-p}}{100} \right), 0 \right] - \frac{\sigma_{ii}}{37.8} + 00.9 \exp \left(\frac{\theta + 273}{293} \right) \quad , \quad \varepsilon^{-p} > \varepsilon_c$$

ε_c is the critical strain value, ε^{-p} is strain rate, σ_{ii} is hydrostatic pressure and θ is temperature. Rice [33] tried to simulate shear deformed chip formation by using the critical shear strain mechanistic model. They gained so much information from photographs of the serrated chips while taking cutting operation during machining. After that, they proposed that the chip changes its geometry continuously from serrated to continuous when nominal shear strain exceeds material fracture strength.

Iwata et al. [34] proposed a new fracture model based on stress&strain curve while the finite element simulation of orthogonal cutting by:

$$b_3 = \int_0^{\varepsilon_f} (\bar{\varepsilon} + b_1 \sigma_m + b_2) d\bar{\varepsilon}$$

The parameters b_1 , b_2 and b_3 are the functions of metallurgical properties and to get these values to require Split-Hopkinson test bar experiments. Shivpuri et al. [35] developed the energy-based fracture model that is similar to the Cockcroft and Latham model. The idea of the model is the mesh element separation or crack initiation starts when the kinematic energy exceeds integral of stress&strain curve of Ti-6Al-4V while simulating shear deformed chips using the finite element model. This model can be express as:

$$C_i = \int_0^{\varepsilon_f} \bar{\sigma} \left(\frac{\sigma^*}{\bar{\sigma}} \right) d\bar{\varepsilon}$$

The C_i is the tensile properties of workpiece and it is linearly independent of tool material properties or any but it is highly linearly dependent with temperature and microstructure of the workpiece material properties. After mesh element separation occurs when energy value is reached, the crack starts to propagate and initiate. Owen and Vaz [36] investigated the numerical method solver for high-speed machining. They studied the workpiece fracture mechanism due to localized adiabatic strain and also implemented adaptive meshing to improve the result of simulation of Ti-6Al-4V. They explained that material failure due to localized adiabatic strain arises from the cumulative effect of microstructural cracks and plastic deformation. According to their model, they defined two parameters to explain workpiece fracture i.e. failure indicator (I) and energy release (W_r). The material fracture model divides a problem into two as an elastic and plastic, in which the first part is assumed that the equation is linearly elastic whereas the second part of the equation is highly nonlinear that including material model relations.

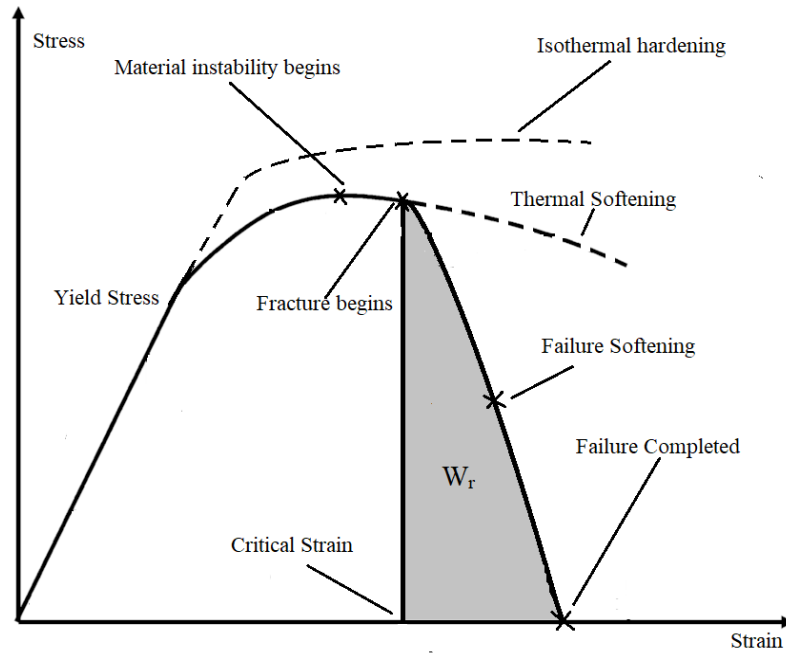


Figure 2.2.1 Stress&Strain Diagram, Isothermal Hardening, Thermal and Strain Softening

Semiatin and Rao [37] proposed a different criterion for shear localization, that model includes a strain hardening, mass heat transfer, flow stress, temperature and strain rate sensitivity to determine the tendency the flow localization. According to literature, it was indicated that the irregular or unstable flow in cutting to be forthcoming when material flow softening is 5 times or greater than strain rate sensitivity. Recht [19] improved a standard criterion of shear instability for localized shear under high dynamic plastic deformation in 1964. The slip can be defined by:

$$0 \leq \frac{\frac{\partial \tau}{\partial \varepsilon}}{\frac{\partial \tau}{\partial \theta} \frac{\partial \theta}{\varepsilon}} \leq 1$$

Komanduri and Hou [16] improved a thermoplastic softening criterion for machining of a Ti-6Al-4V. Their model analyzes the serrated chip with shear localization by including heat transfer and temperature issues in the cutting area. They also implemented a moveable mass heat transfer method to increase the precision of the result. The speed of the machining process when shear localization is about to occur is defined as the critical cutting speed. It was found that the low the depth of cut and high critical cutting speed are suitable for the onset of shear localization. The value of cutting speed and depth of cut for the onset of the shear localization was specified to 0.42 meters per minute and 0.2 millimeters respectively in the machining of Ti-6Al-

4V. A curve fit equation between the critical cutting speed, depth of cut and shear localization was found analytically is given by:

$$V_c = 0.082667 \times a_p^{-1.0054}$$

2.3 Experimental Aspect of Shear Localization of Chip Segmentation in Ti-6Al-4V

Experimental investigation of the machining of Ti-6Al-4V has been studied to measure cutting forces and visualize the segmented chip formation in cutting speed (V_c) lesser than 300 m/min [18] [38]. These experimental works found out the most important features in the machining of Ti-6Al-4V and titanium alloys [18]. Shear localization is mostly occurring due to low thermal properties of titanium alloys and repeating inhomogeneous deformation occurs in the first shear zone. Instability issues while machining the titanium alloys result in the serrated chips. There is an oscillation in the cutting and thrust force in the machining that result in chatter which dramatically decreases the efficiency of surface finish. High temperature at contact surface of tool and work piece and high chemical reactivity of Ti-6Al-4V causes rapid tool wear. Titanium alloys have low elastic modulus compared to other metals and its elastic modulus decreases fast while temperature rising. This results in unwanted deflection while machining micro parts and decreases the dimensional accuracy of the final parts. In literature, there are 2 types of chip formation in machining of Ti-6Al-4V. One study covers plastic instability and localized shear in a shear band which results in shear failure along a workpiece surface. The second study covers built-up edge formation with insignificant deformation by the workpiece ahead of the cutting tool.

Molinari et al. [39] studied on shear localization and chip segmentation in the machining of Ti-6Al-4V. They conducted their experimental at cutting speed in a range from 0.6 m/min to 4380 m/min. They used small depths of cut to prevent tool failure while cutting at a higher speed. All experiments were conducted with tungsten carbide tools with a 0° rake angle and the tools had the flat surface without chip-breaker. In cutting speeds lower than 72 m/min, serrated chip formation occurs due to deformed shear bands which appear as a result of low thermal properties of Ti-6Al-4V. However, at lower cutting velocities, the thermal and strain instability process is not strong enough and shear localization is not clear as at high cutting velocities.

Barry et al. [40] carried out metal cutting experiments to understand the reason of serrated chip formation under orthogonal cutting conditions. Their material was the 25 mm diameter 1.1 mm in width Ti-6Al-4V disk with 330 HV hardness and tool was the uncoated carbide which has a rake and clearance angle of -6° and 12° respectively. They evaluated all serrated chip formation in different cutting conditions in a range of 0.02-0.1 mm/rev feed and 15-180 m/min cutting speed. Even orthogonal cutting experiments conducted at low cutting speed (15 m/min) and uncut chip thickness (0.02 mm), sawtooth serrated chips were observed. Their study found out that an increase in both or either cutting conditions changes chip formation from non-periodic to periodic saw tooth serrated chip formation. Besides, the welding problem between tool and workpiece during cutting occurs and the level of welding increase with cutting speed. They revealed that catastrophic failure of the workpiece occurs not only within the primary shear zone but also inside the weld formed zone between the chip and rake face. Also, the failure of such welds looks to be the reason of when cutting speeds are higher than 30 m/min [38] [40].

Xie and Bayoumi [22] evaluated orthogonal cutting experiments and they focused on the microstructural and metallurgical analysis of Ti-6Al-4V to analyses the chip segmentation and the shear localization. Their cutting condition changed in a range of cutting speeds from 30 to 480 m/min and feed from the 0.03 to 0.5 mm/rev. Their microstructural studies showed that there is no phase transformation due to diffusion but there is a transformation from beta to the alpha because of non-diffusional phase transformation when testing under the X-ray diffraction method. The maximum principal shear originates in a small cutting area rather than in a cutting plane which is not significant in the research of orthogonal cutting. There is always a critical cutting speed for chip formation at which shear localization was observed for each metal. Besides, the frequency of the shear band increases with a feed rate and decreases with cutting speed.

Shivpuri et al. [35] carried out a turning experiment on Ti-6Al-4V at cutting speed of 60,120 and 240 m/min, depth of cut 2.54 mm and feed of 0.127 and 0.35 mm/rev. They also measured the cutting and thrust force of the experiments by using Kistler Type 9121 dynamometer. They used a standard carbide tool with a 15° rake angle and 6° clearance angle. They also found out that the crack propagation causes to occur the

serrated chip formation which takes place in the first shear area on the tool and chip contact face and at lower speeds. Moreover, the crack propagates to the workpiece uncut surface at high-speed machining operations because of temperature in the at the tool face which is greater than that in the workpiece uncut surface. This temperature is higher than the beta phase transform temperature so it results in rearranged microstructure which increases the ductility of the material in the shear area.

Ribeiro et al. [41] conducted a usual turning experiment while machining of Ti-6Al-4V with uncoated carbide tools when the machining parameters are 55, 70 and 110 m/min cutting speeds, 0.1 mm/rev uncut chip thickness and 0.5 mm depth of cut. The ambition of this study was to get an effective range of cutting speed for the best surface finish with minimum surface roughness. The surface roughness is minimum with a cutting speed of 90 m/min.

Lee and Lin [42] coped with a high strain deformation experiment at high temperatures to identify the response of the Ti-6Al-4V. Since they used Split-Hopkinson Test bar setup to perform their experiments at 1000 strain rate and temperature from 700 °C to 1000 °C in intervals of 100 °C. In each test sample, a transformed adiabatic shear band appears in the microstructural analysis which pointed out that a shear localization occurred during deformation. The fracture mechanism of the test samples showed that the workpiece fracture takes place at the adiabatic shear bands and that the thickness and hardness of it changes completely with temperature.

Majorell et al. [9] worked on the deformation mechanism of Ti-6Al-4V that experiments were tested in a range of 350-1100 °C temperature and 0.001-10 s⁻¹ strain rates. The flow stress reduces quickly with the temperature above 500 °C. The phase transformation from α to β phase transus becomes the driving force behind the behavior of the material in a range from 1100-1350 K. This α to β transformation creates variety in the strain rate sensitivity that means sensitivity is higher in the situation of 100% β phase material.

Pérez et al. [43] carried out milling experiments on Ti-6Al-4V alloy to understand the effect of the tool coating and its geometry. They also changed the cutting parameters such as cutting speed, depth of cut and feed per tooth to predict the effect of machinability for milling process. The cutting speed and feed are between 11 and 14

m/min and 0.04 and 0.15 mm/tooth respectively. The milling tool has a helix angles of 30°, 45°, 60°, and the number of teeth of 3, 4, 6 respectively. The tool was uncoated cemented carbide. They concluded that cutting speed is highly effective on tool wear. Besides, while machining at high feed values, it increases feed force, chip deformation and separation. Further, it is better to machine titanium alloys with TiCN coated tool because they discovered that flank wear is less problematic with that coating.

2.4 Computational Simulation of Shear Localization in Ti-6Al-4V

Obikawa and Usui [32] improved a numerical code for the computational simulation of Ti-6Al-4V. In their finite element model, they used linear quadratic isoparametric elements to mesh a cemented carbide and Ti-6Al-4V. The tool was modeled as an undeformable and used just calculated the temperature. The uncut chip thickness and cutting velocity and tool rake angle were 0.25 mm/rev, 30 m/min and 20° respectively. They used Lagrangian formulation to get 2D elastic-plastic dimensional analysis and they discovered a new method to solve unsteady heat conduction and workpiece nonlinearities problems. The Coulomb friction between rake face and tool and catastrophic flow stress of the Ti-6Al-4V also took into account at elevated temperatures and high strain rates. They defined the geometry boundary to predict fracture strain before separation and applied the boundary condition that put on a predetermined path where the crack propagation. Thus, they simulated the saw tooth serrated chip formation. However, these finite element models are not powerful enough to express real physical phenomenon and mechanics of serrated chip formation.

Maekawa et al. [44] simulated the metal cutting process by using iterative convergence method which method has flow trajectory particles. As a nature of the finite element method, the iterative convergence method was composed of a series of finite meshes and paths of the particles. FEM calculation continues step by step moving tool direct to workpiece so force and deformation forms between chip and inserts. Plasticity builds up in the cutting area and the view of a chip is controlling with the experimental view of cutting chips and the simulation is run until simulation and experimental shape of chips the same. In addition to this, the only continuous chip can be simulated. After that, the complex algorithm was developed the simulate serrated and discontinuous chip. First, the plastic strain fail mechanism was develop using the

iterative convergence method so crack first evolved at the tool/workpiece contact face and propagates cutting surface of the workpiece toward the free surface which causes the discontinues or serrated chip formation. They understood that the serrated chip form seen the result of a small plastic strain. Serrated chip formation was not related to adiabatic shear instability.

Owen and Vaz [36] computed high-speed machining of titanium Ti-6Al-4V alloy which focused on the topic of strain localized chip formation, workpiece fracture mechanism and evolution of mesh refinement. Their model controlled the error by using the uncoupled integration using Lemaitre's damage criterion. Their simulations were done by in a range of cutting speed and rake angle between 5 to 20 m/min and -9° to 9° respectively. Their failure mechanism was based on fracture energy that controls the plastic strain and plastic energy to imply a fracture of the model. In their model, the fracture mechanism takes place when plastic strain reaches the workpiece failure strain.

Bäker et al. [45] found out that the effect of the cutting speed and modulus of the elasticity on chip formation. They also indicated that the elastic modulus has a high impact on the way of chip producing. Also, they discovered that while thermal conductivity is increasing, chip formation decreases. They simulated the cutting process by using exact deformation without node separation. The chip covers the tool while the tool is moving directly to the workpiece that is called mesh deleting technique. This is actually known as chip segmentation or chip formation in the metal cutting process. They simulated the cutting process by using high cutting speed, no heat transfers and friction between tool and workpiece. However, their simulation was not practical.

Sandstrom and Hodowany [46] ran their computational model at high-speed orthogonal machining of Ti-6Al-4V by using commercial software at a cutting speed of 600 m/min. Their model showed the result of cutting forces, plastic stress&strain, serrated chip formation, the operation temperature of the workpiece and tool. Their simulation result got a good agreement with experimental data so they measured cutting force for comparison with the simulated machining force. However, their finite element model was looking inaccurate while the simulation of low cutting speed conditions.

Hua and Shivpuri [35] used a Deform 2D/3D software which uses an implicit Lagrangian model for the orthogonal metal cutting process of Ti-6Al-4V. The workpiece was assumed as a visco-elastic material due to high strain fracture taking place in the first and second deformation zone during orthogonal cutting operations. Besides, high fracture material properties were defined around the tool contact face and excessively distorted work piece's cutting surface mesh meshed again if it is required. The tool modeled as a rigid body so thermo-mechanical properties of the tool can be simulated. Also, the thermo-mechanical properties of the workpiece material were simulated by using a dynamic flow stress model. Crack propagation or initiation at the cutting surface was modeled by using the ductile fracture criterion. They ran their simulation at uncut chip thickness 0.127 mm/rev and cutting speed 1.2, 120 and 600 m/min. They expressed that the effective plastic strain shows the location of the shear localization. They indicated that the serrated chip formation while cutting Ti-6Al-4V occurs due to flow localization within the first deformation zone. The main parameters behind the separation of chips were flow localization which causes a fracture. Localized flow stress-strain was the reason for crack initiation and propagation while the secondary fracture area controls the chip segmentation like continuous, discontinuous and serrated chips. Their study showed that discontinuous chip forms below cutting speed of 1.2 m/min and serrated chip formation seen at cutting speed of between 120 m/min to 600 m/min.

CHAPTER 3

3. MODELING OF MACHINING SIMULATION OF Ti-6Al-4V BASED ON FINITE ELEMENT APPROACH

3.1 Finite Element Modeling

Although analytical models can be considered as an effective method of studying metal cutting operations, these models rarely reflect the actual machining conditions because of the very complex phenomena involved in the machining and strong interactions such as friction at tool/chip and tool/workpiece interfaces, cutting tool micro-geometry and material behavior. Therefore, few studies in the literature are devoted to the prediction of the onset of shear localization by analytical methods. An example could be the work of Xie et al. [22], where they defined a flow localization parameter (β) to judge the onset of shear localization as a function of material parameters and cutting conditions (cutting speed and feed). They obtained a critical flow localization parameter of 4.41 for Ti-6Al-4V for an area removal rate of 0.004 (m²/min).

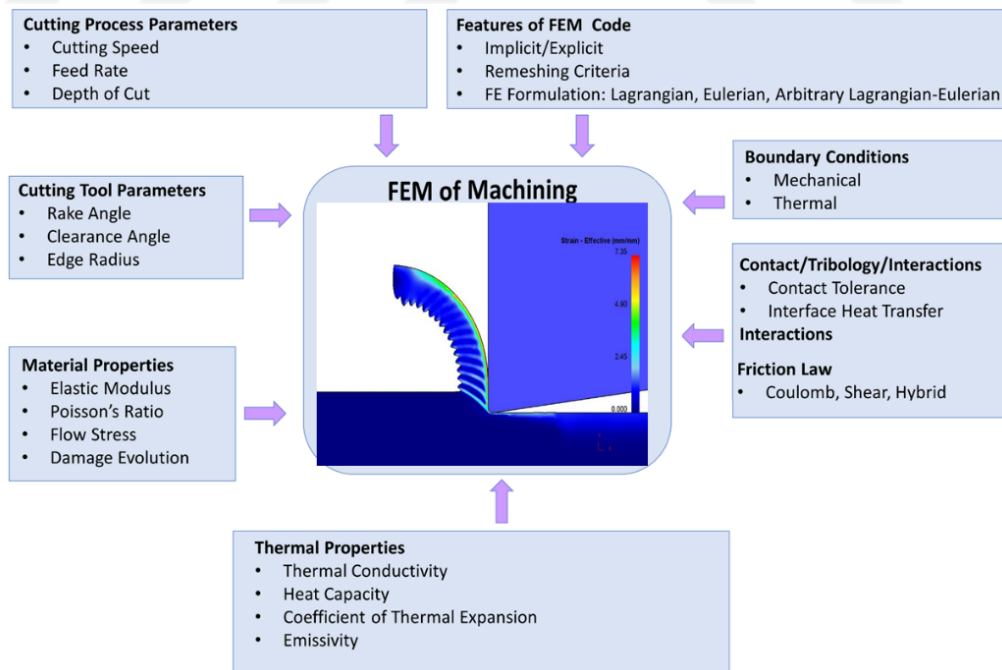


Figure 3.1.1 Inputs of the finite element model of the machining

They considered a power law relation to express shear stress as a function of shear strain, shear strain rate and temperature, which may not reflect the material properties in some occasions. Additionally, their relation does not incorporate cutting tool micro geometry (for instance cutting edge radius) to calculate flow localization parameter. The use of experimental techniques has always faced the challenge of being costly and time consuming and its limitations in parametric studies. For instance, producing cutting tool with a desired edge radius is a tedious and in some occasions impossible task because of the limitations in the manufacturing process and cutting tool materials. Therefore, finite element method is considered as an indispensable tool for the modeling of machining operations [47]. However, the accuracy of the finite element modeling to predict the outputs of the machining largely depends on the inputs of the FE model. Figure 3.1.1 illustrates the required inputs for the finite element modeling of machining. Each input should be carefully fed into the model to get a reasonable and accurate output. Using FEM, valuable information such as cutting and thrust forces, chip morphology, stress, strain, strain rate, temperature, residual stresses and damage can be predicted with acceptable accuracy.

Among various inputs of the FE model given in Figure 3.1.1 material properties (especially the flow stress) and contact/tribology at the interfaces are of paramount importance. One of the strengths of the FEM is that the constitutive material model can be well-defined as a function of temperature, strain and strain rate with a damage criterion. In this study, quartz 3-component dynamometer (Kistler-9265B) is used to record cutting and thrust forces for orthogonal experiments at different cutting speeds and uncut chip thicknesses.

3.2 Finite Element Modeling Procedure

In this study different modeling approaches are used to serve the purpose of the study. The workpiece is modeled as an elasto-plastic material while the cutting tool is defined as an elastic material which is given in Table 3.2.1. A temperature dependent elastic modulus, thermal conductivity and specific heat of the workpiece material is defined as temperature-dependent as given in Table 3.2.2.

Table 3.2.1 Thermal and mechanical properties of the tungsten carbide

Density	Elastic Modulus	Poisson's ratio	Thermal Conductivity	Specific heat
11900 (kg/m ³)	534 (GPa)	0.22	50 (W/mK)	400 (J/kgK)

The generic boundary conditions of the finite element model are shown in Figure 3.2.1. It should be mentioned that in some cases the tool is fixed in X and Y direction, while the cutting tool moves towards the workpiece. A heat transfer coefficient of 10000 (W/m²°C) [47, 48] is used in all simulations of this study. It is worth mentioning that different heat transfer coefficients are used in the literature to simulate orthogonal cutting processes. For instance, Calamaz et al. [4] have used a value of 20000 (W/m²°C), Karpuz [47, 48] have used 10000 (W/m²°C) and Sima and Ozel [49] have used 1000 (kW/m²K) and Oliaei and Karpuz [50] have used 5000 (W/m²°C). This is mainly due to the fact that the simulation time for the machining is very short. Consequently, there is not enough time for heat diffusion and obtaining real temperature distribution [51]. The tuning of heat transfer coefficient is used by Fleischer et al. [52] and Yen et al. [53] with the aim of accelerating the convergence time.

Table 3.2.2 Temperature dependent material properties

Elastic Modulus (MPa)	$E_Y(T) = -57.7xT + 111672$
Thermal Expansion (1/°C)	$\alpha_T(T) = 3x10^{-9}T + 7x10^{-6}$
Thermal Conductivity (W/m/K)	$\lambda(T) = 0.015T + 7.7$
Heat Capacity (N/mm²/°C)	$C_p(T) = 2.7e^{0.0002T}$

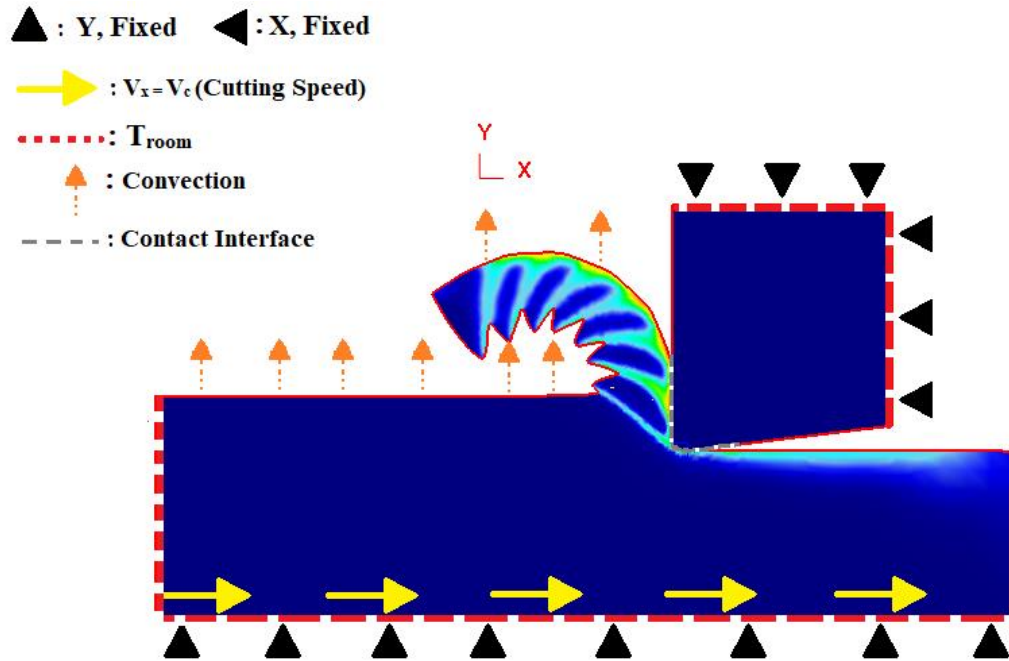


Figure 3.2.1 Representation of initial boundary conditions of Finite element model

3.3 Material Models

Material modeling can be considered as the core of FEM of machining. In finite element models, shear localization is modeled by two different approaches. The first approach is to artificially modify the material flow stress at higher strains and the second approach is to integrate a damage criterion. This is resulted in the development of different material models to serve this purpose, which will be discussed here.

Johnson-Cook Material Model

The material models have established an outline for research and development that modeling the machining condition for evaluating the results. Perhaps the most widely used constitutive material model for the FE modeling of machining is Johnson-Cook (J-C) material model. This model uses three multiplicative, yet distinctive terms to define the thermo-mechanical behavior of the materials as a function of plastic strain (ϵ), strain rate ($\dot{\epsilon}$) and temperature (T).

$$\sigma = (A + B\epsilon^n) \left(1 + C \ln \frac{\dot{\epsilon}}{\dot{\epsilon}_0} \right) \left(1 - \left(\frac{T - T_r}{T_m - T_r} \right)^m \right)$$

The Johnson-Cook constitutive model has included three different unique terms such as elastoplastic term, viscosity and thermal softening term. In the JC model, σ is the

effective stress, ϵ is the plastic strain, $\dot{\epsilon}$ is the strain rate, T , T_m , T_r is the current temperature, melting and room temperature of the workpiece respectively. The other equation constants are the Johnson-Cook model parameters which are changing due thermo-mechanical properties of the workpiece. The material constants A , B , C , n and m identify the physical characteristic of the workpiece which are yield strength, ultimate tensile strength, thermal softening, strain hardening and strain rate sensitivity.

Table 3.3.1 Parameters of Johnson-Cook Material Model

A (MPa)	B (MPa)	C	n	m	Reference
862	331	0.012	0.34	0.8	Johnson and Holmquist, [54]
782.7	498.4	0.028	0.28	1	Lee and Lin [42]
724.7	683.1	0.035	0.47	1	Lee and Lin [55]
870	990	0.011	0.25	1	Shivpuri et al. [56]
968	380	0.0197	0.421	0.577	Li and He [57]
859	640	0.000022	0.22	1.1	Ozel and Zeren [58]
1098	1092	0.014	0.93	1.1	Gregory [59]
997.9	653.1	0.0198	0.45	0.7	Seo et al. [60]

The most used Johnson-Cook material model parameters given in the literature shows in Table 3.3.1.

These Johnson-Cook model constants are used for the analysis of the finite element model to reach effective flow stress and plastic strain. Johnson-Cook model is very convenient to define the high strain rate and temperature behavior with five determined parameters for Ti-6Al-4V alloy. The stress and strain curves can be seen in Figure 3.3.1, Figure 3.3.2, Figure 3.3.3 and Figure 3.3.4.

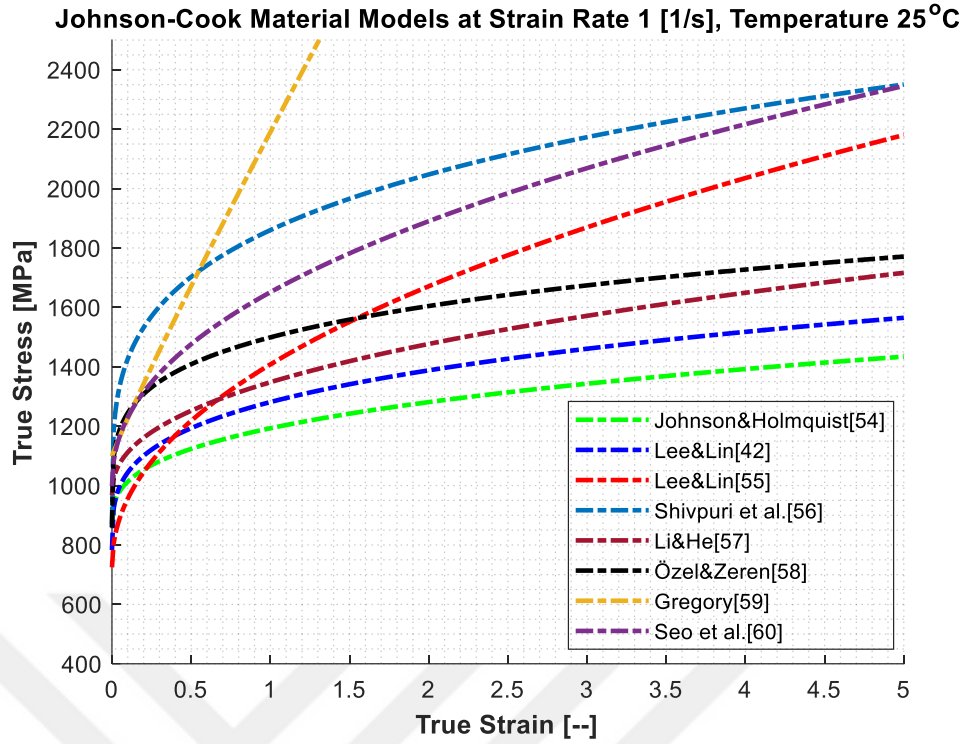


Figure 3.3.1 Stress&Strain curves at Strain rate 1 s^{-1} , Temperature $25 \text{ }^\circ\text{C}$ using all parameters at Table 3.1

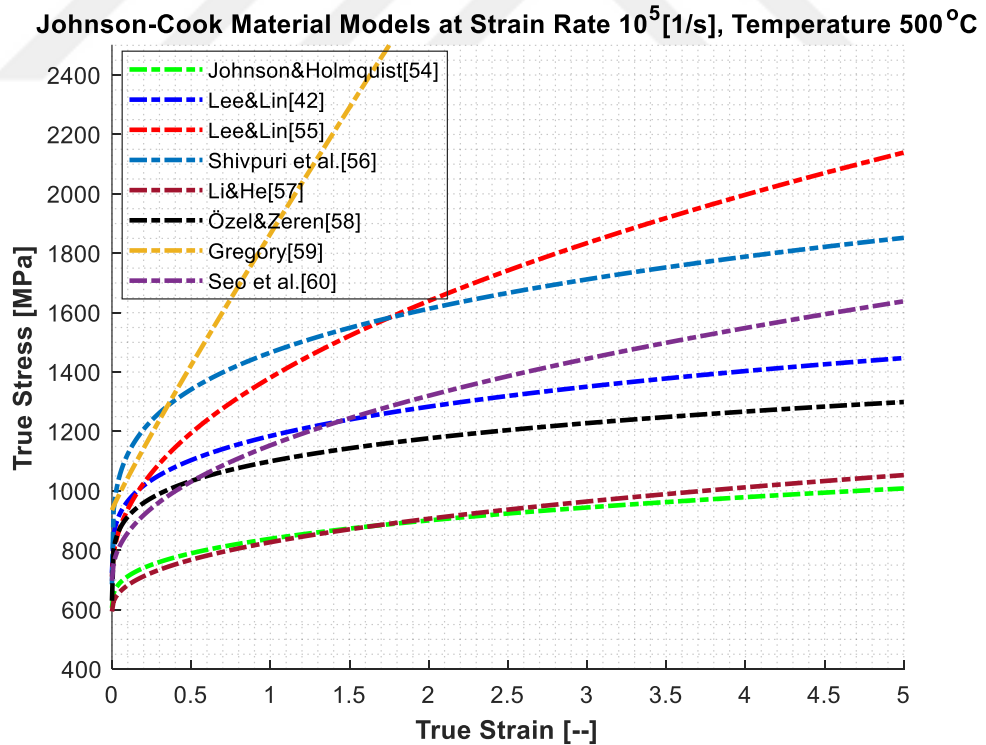


Figure 3.3.2 Stress&Strain curves at Strain rate 10^5 s^{-1} and Temperature $500 \text{ }^\circ\text{C}$

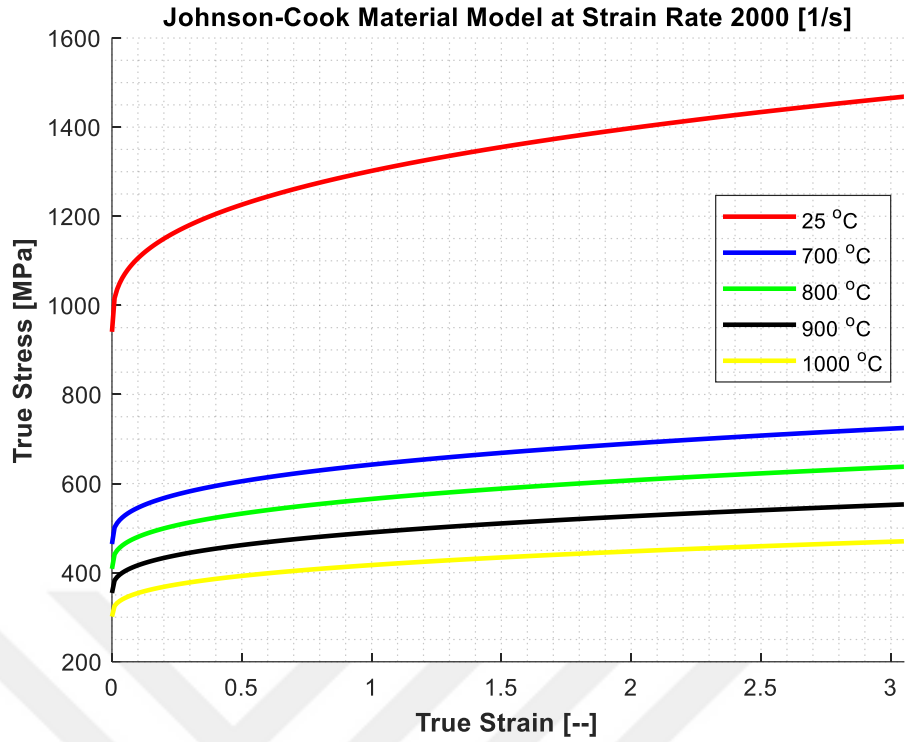


Figure 3.3.3 Stress&Strain curves at Strain rate $2 \times 10^3 \text{ s}^{-1}$ using Johnson and Holmquist parameter [54]

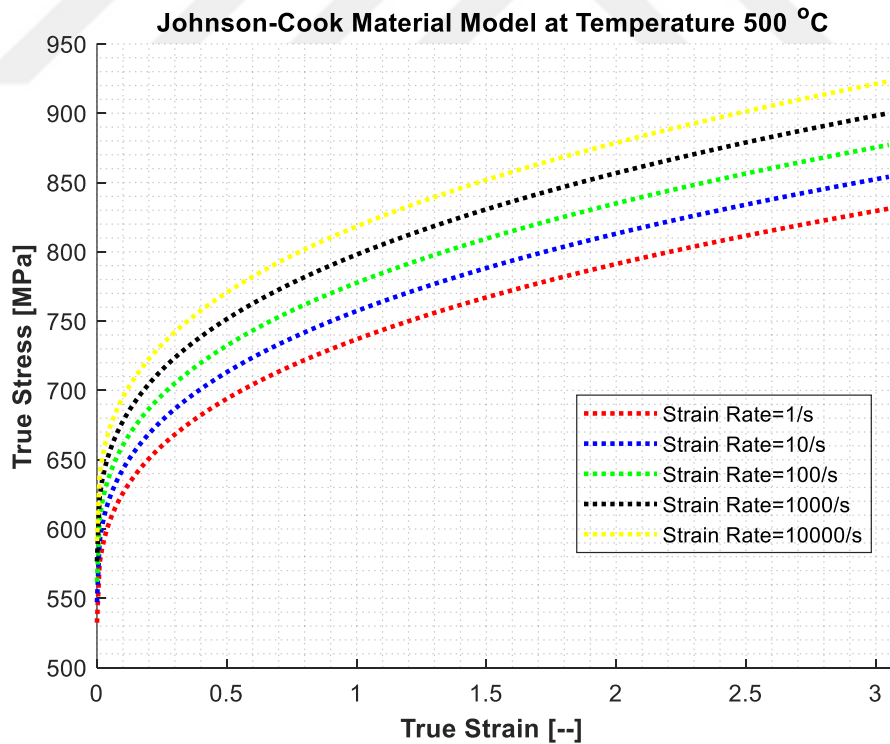


Figure 3.3.4 Stress&Strain curves at Temperature 500 °C using Johnson and Holmquist parameter [54]

Modified Johnson-Cook Material Models Proposed by Calamaz et al. [4, 61]

TANH Function [4]

Calamaz et al. [4] introduced a new term based on the current Johnson-Cook model to present the strain-softening effect. The modified material model is expressed by the following equation:

$$\sigma = \left(A + B\varepsilon^n \left(\frac{1}{\exp(\varepsilon^a)} \right) \right) \left(1 + C \ln \frac{\dot{\varepsilon}}{\dot{\varepsilon}_0} \right) \left(1 - \left(\frac{T - T_r}{T_m - T_r} \right)^m \right) \times \\ (D + (1 - D) \tanh \left(\frac{1}{(\varepsilon + S)^c} \right))$$

where

$$D = 1 - \left(\frac{T}{T_m} \right)^d, \text{ and } S = \left(\frac{T}{T_m} \right)^b$$

According to research followed by [62] showed that effective flow stress decreases while the temperature is increasing. The effective flow stress is increasing at low strain like the J-C model but at high strain, the workpiece begins to soft due dynamic recrystallization mechanisms which result in decreasing effective flow stress. Therefore, a new term in the modified model defines the dynamic recrystallization mechanism of Ti-6Al-4V. The new model has two optional values of parameter d that represent different softening.

Table 3.3.2 Parameters of Calamaz (TANH) material Model [4]

A (MPa)	n	B (MPa)	C	m
968	0.421	380	0.0197	0.577
a	b	c	d	$\dot{\varepsilon}_0$ (1/s)
1.6	0.4	6	1 or 1.5	1

The parameters of the new TANH equation are shown in Table 3.3.2.

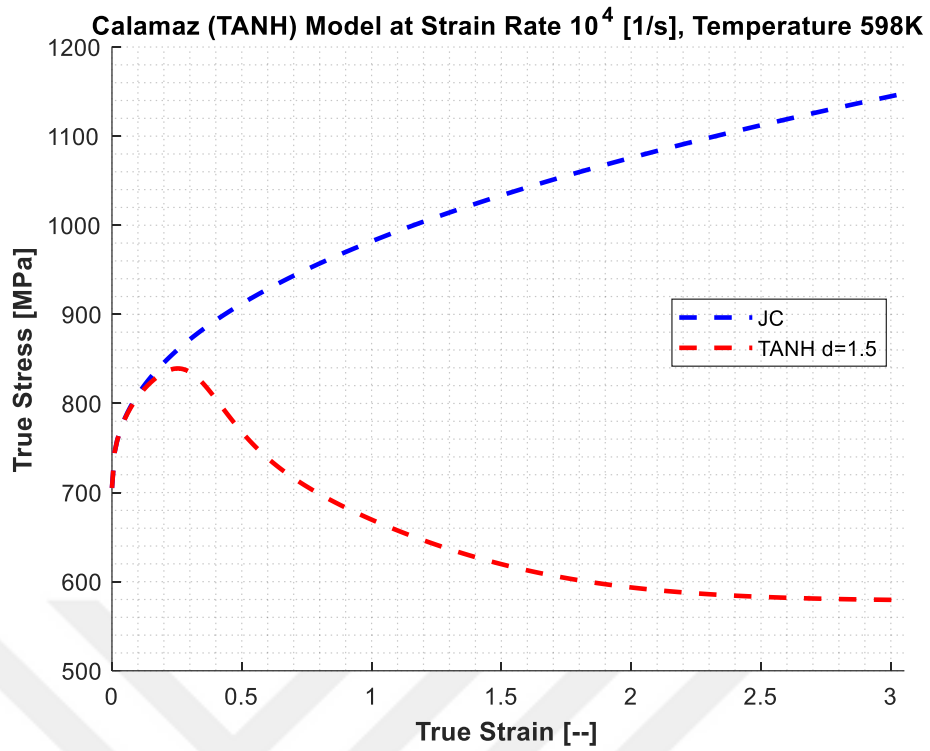


Figure 3.3.5 Stress&Strain curves for Johnson-Cook (JC) and Calamaz (TANH) model at temperature 598K, strain rate of 10^4 s⁻¹ [4]

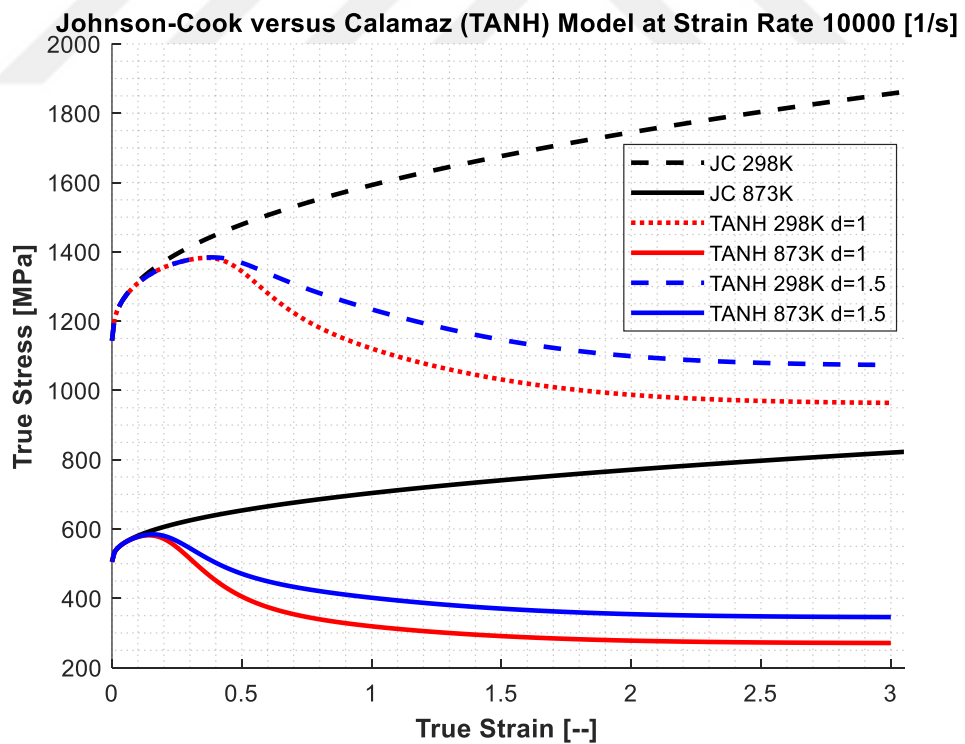


Figure 3.3.6 Stress&Strain curves for Johnson-Cook (JC) and Calamaz (TANH) model at a strain rate of 10^4 s⁻¹ [4]

Figure 3.3.5 and Figure 3.3.6 show the stress-strain curves for different temperatures at 10000 strain rate for the Johnson-Cook model and Calamaz the modified material model (TANH) while $d = 1$ and 1.5 . It shows clearly that when parameter d decreasing, the strain-softening effect becomes dominant.

The TANH model material constant a and c vary the slope of flow stress-strain curves which decreases at high strains for the parameter a and decreases at low strains for parameter c . The TANH material constant b gives the plastic strain value when maximum stress is obtained. The constitutive material constants used in the simulations are a reference to the work of Li and He [57]. The sensitivity relation between flow stress and strain rate is the same for both models because TANH modified model does not take into account any strain rate effect due to dynamic recrystallization mechanisms.

Calamaz-Exponential Function [61]

The second model is very similar to the Johnson-Cook material model which they just introduce a new term to add strain softening at higher strain and strain rate. The new term introduces the strain-softening effect after exceeding 0.3 strain and 1000 strain rate. The new model is given by the following equation:

$$\sigma = \left(A + B \left(\frac{1}{\dot{\epsilon}} \right)^f \left(\epsilon^{(n-0.12(\dot{\epsilon}\epsilon)^f)} \right) \right) \left(1 + C \ln \frac{\dot{\epsilon}}{\dot{\epsilon}_0} \right) \left(1 - \left(\frac{T - T_r}{T_m - T_r} \right)^m \right)$$

where f is a strain-softening controlling parameter that could be between 0 and 0.22. As you can see in Figure 3.3.7, the new material model shows nearly the same behavior as the Johnson-Cook model when the parameter f is equal zero. The new strain-softening term begins to show its effect when the f value is higher than zero. The effect of strain-softening becomes dominant while the f parameter is increasing. Figure 3.3.7, Figure 3.3.8, Figure 3.3.9 and Figure 3.3.10 show the effect of the strain-softening phenomenon when the f parameter is to equal 0, 0.05, 0.11 and 0.22.

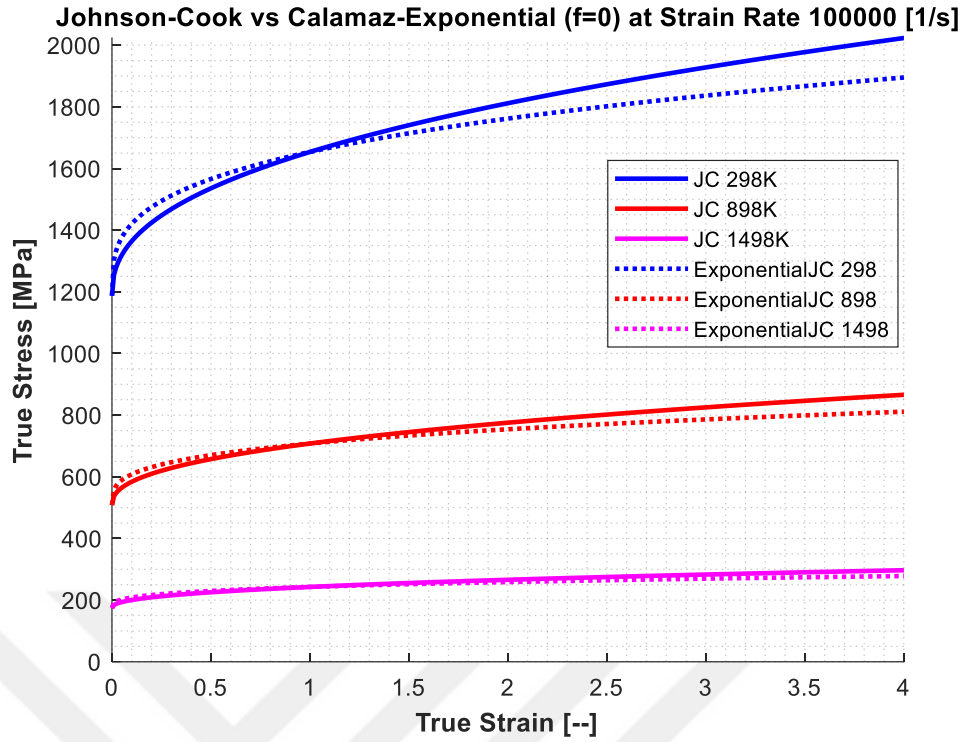


Figure 3.3.7 Stress&Strain curves for J-C and Exponential-Calamaz (f=0) model at a strain rate of 10^5 s^{-1} [61]

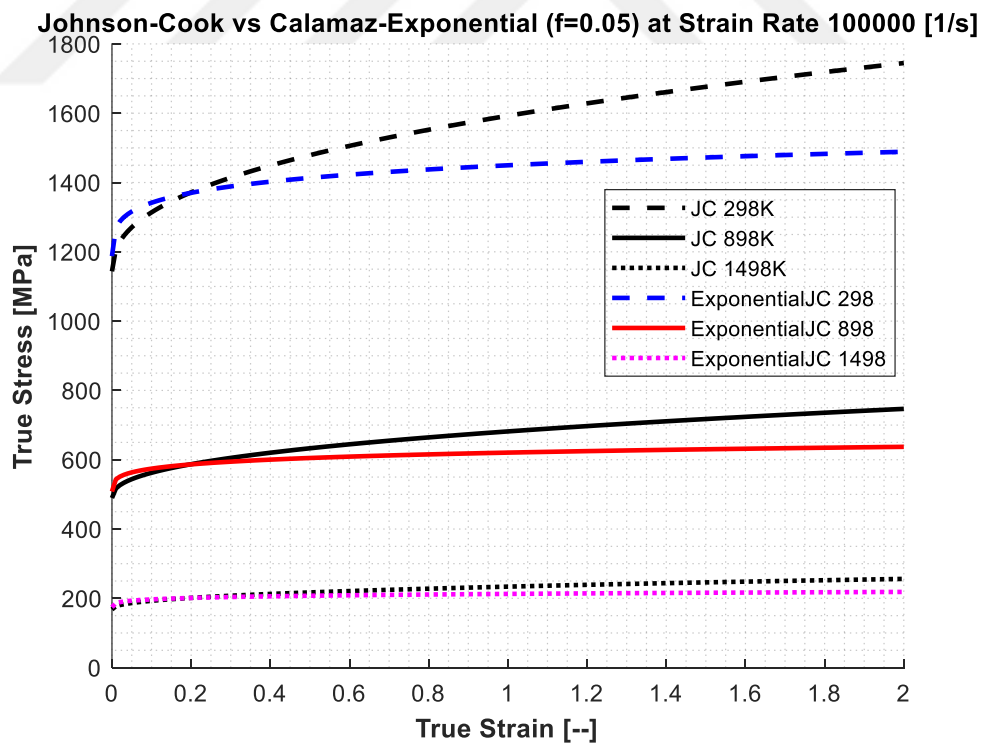


Figure 3.3.8 Stress&Strain curves for J-C and Exponential-Calamaz (f=0.05) model at a strain rate of 10^5 s^{-1} [61]

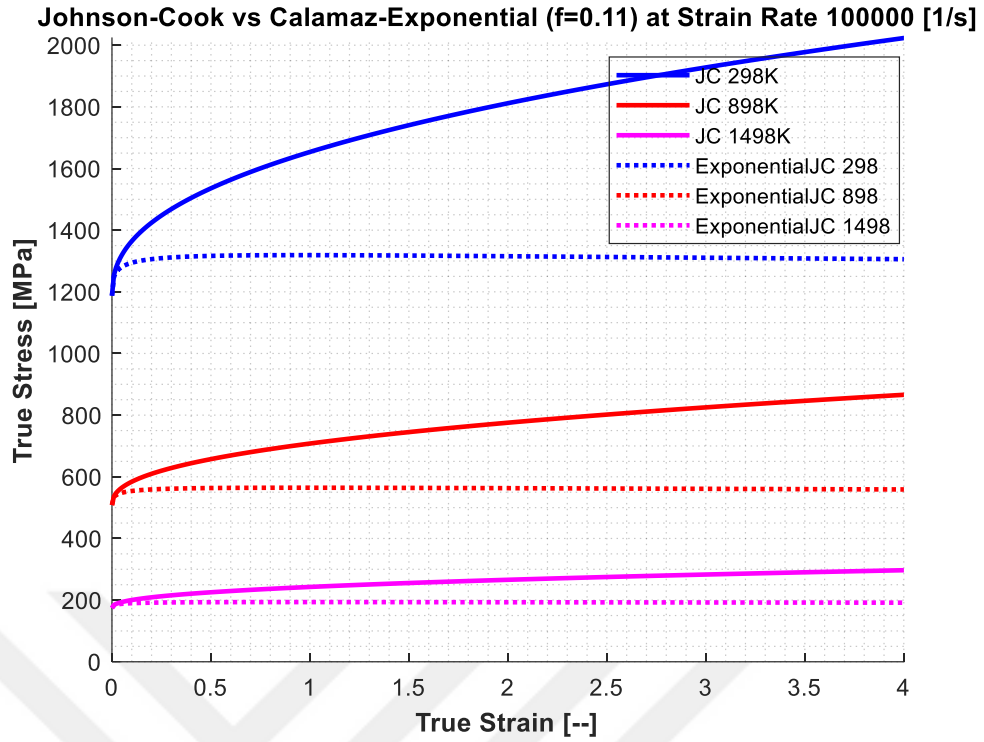


Figure 3.3.9 Stress&Strain curves for J-C and Calamaz-Exponential (f=0.11) model at a strain rate of 10^5 s^{-1} [61]

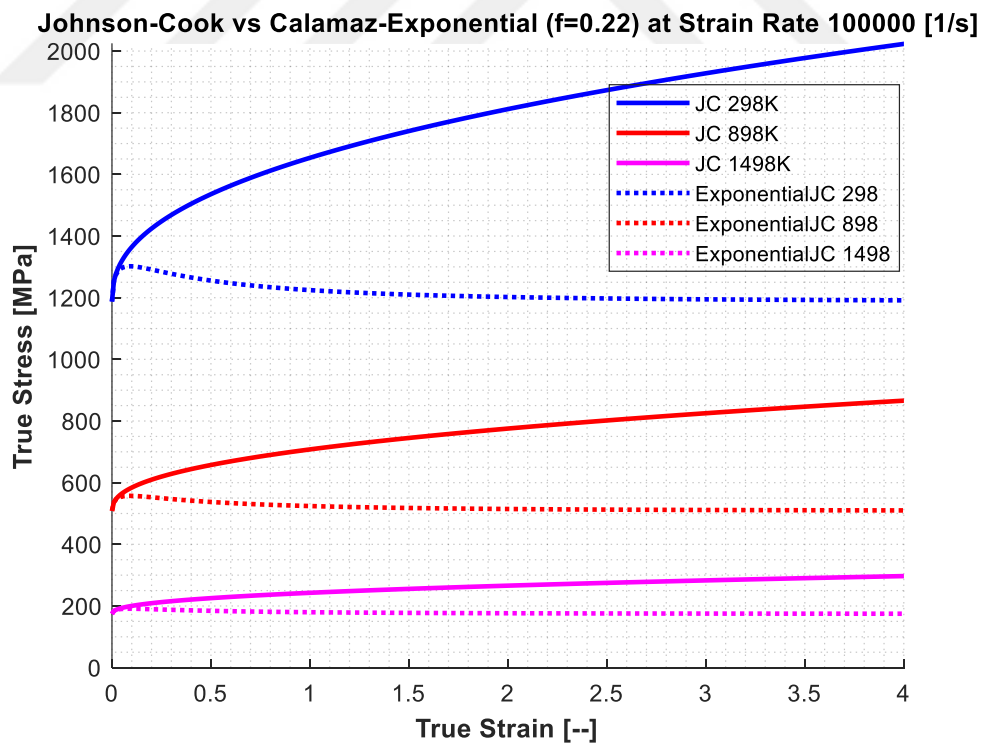


Figure 3.3.10 Stress&Strain curves for J-C and Calamaz-Exponential (f=0.22) model at a strain rate of 10^5 s^{-1} [61]

Modified Johnson-Cook Material Model Proposed by Sima&Ozel [49]

Sima&Ozel Model I

In this Sima&Ozel model I, the J-C parameters in the model are obtained at high strain rates and temperatures by Lee and Lin [42]. In their first modification, a TANH flow softening term is used. The purpose was to leave flow stress at low strains unchanged and introduce different levels of softening at higher strains through parameters p , r , S , and M . The first model is expressed by the following equation:

$$\sigma = [A + B\varepsilon^n] \left[1 + C \ln \frac{\dot{\varepsilon}}{\dot{\varepsilon}_0} \right] \left[1 - \left(\frac{T - T_r}{T_m - T_r} \right)^m \right] \left[M + (1 - M) \left[\tanh \left(\frac{1}{(\varepsilon + p)^r} \right) \right]^S \right]$$

When flow stress reaches the maximum value while a strain is increasing, flow stress begins to decline while increasing strain due to flow softening phenomenon but after reaching critical strain value, flow stress starts again to increase with strain. Figure 3.3.11 shows stress-strain curves at different temperatures and strain rates for the new modified material model.

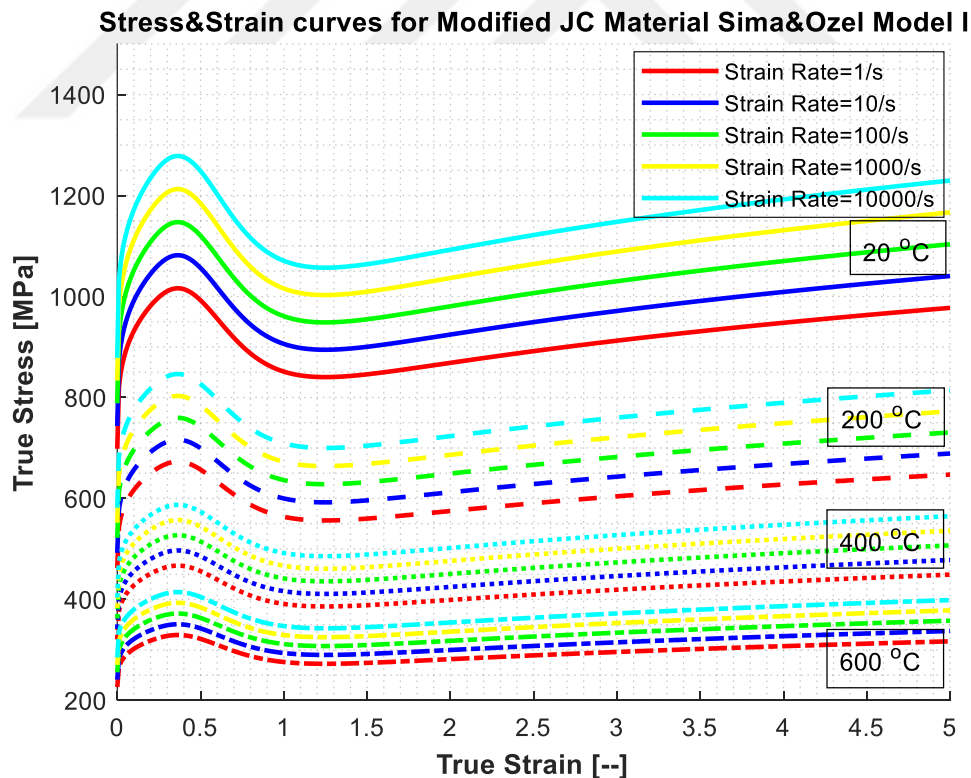


Figure 3.3.11 Stress&Strain curves for Modified JC Material Sima&Ozel Model I at different temperature and strain rate [49]

Strain hardening effect takes in place when the material works below the critical strain value. The parameter M is actually defining the flow softening after reaching a critical strain value 0.5 but the degree of the flow softening is the same every flow stresses at all temperatures.

Sima&Ozel Model II

In Sima&Ozel Model II, a modified material model includes strain-softening phenomenon as well as temperature softening and the parameters. Model II is given in

$$\sigma = [A + B\varepsilon^n] \left[1 + C \ln \frac{\dot{\varepsilon}}{\dot{\varepsilon}_0} \right] \left[1 - \left(\frac{T - T_r}{T_m - T_r} \right)^m \right] [D + (1 - D) \left[\tanh \left(\frac{1}{(\varepsilon + p)^r} \right) \right]^s]$$

where

$$D = 1 - \left(\frac{T}{T_m} \right)^d, \text{ and } p = \left(\frac{T}{T_m} \right)^b$$

The effect of temperature is controlled by the exponent parameters b and d which increase the softening phenomenon of the flow stress at high temperatures. Since strain or temperature softening might be related to phase transformation and dynamic recrystallization of the workpiece at a specific temperature range.

Thermal softening on the flow stress is shown in Figure 3.3.12 which is quite logical. This shows that softening increases with temperature.

Sima&Ozel Model III

Sima&Ozel model III is very similar to Calamaz TANH model which includes softening at elevated strain values with a difference with the model I and II. The J-C parameters used in model II and III is in reference to [42].

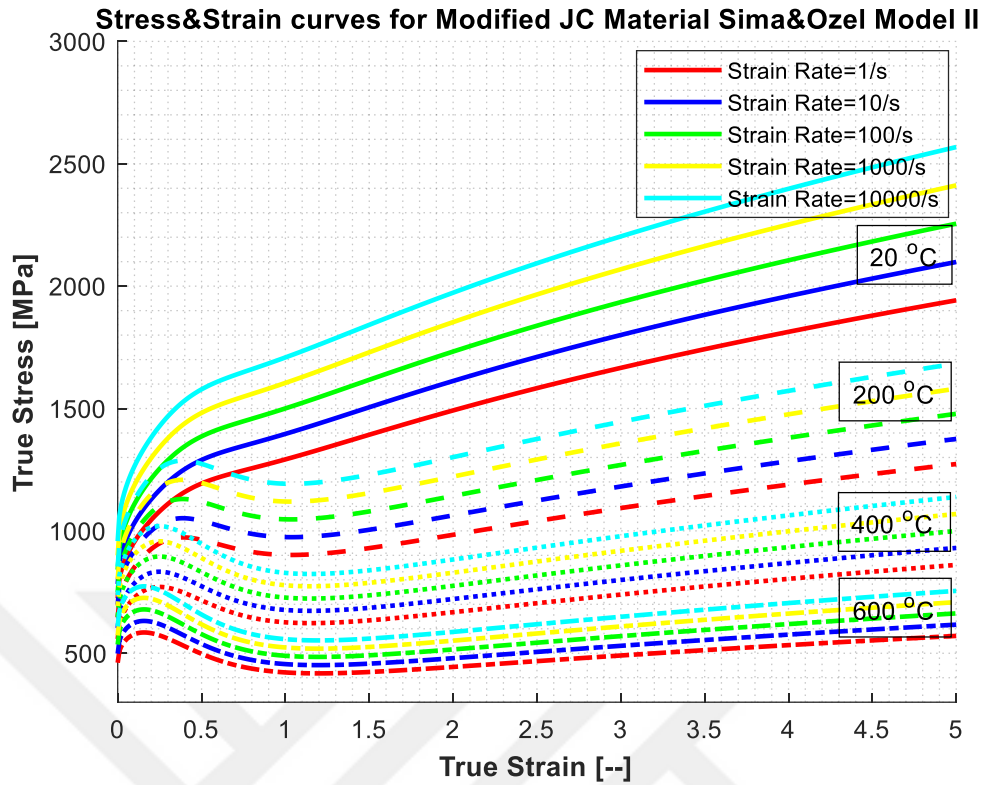


Figure 3.3.12 Stress&Strain curves for Modified JC Material Sima&Ozel Model II at different temperature and strain rate [49]

Table 3.3.3 Parameters of Modified Material Sima&Ozel Model I, II and III [49]

	M	s	a	b	r	d
Sima&Ozel Model I	0.7	4	-	-	-	-
Sima&Ozel Model II	-	1.5	-	2	2	1
Sima&Ozel Model III	-	0.05	2	5	2	1

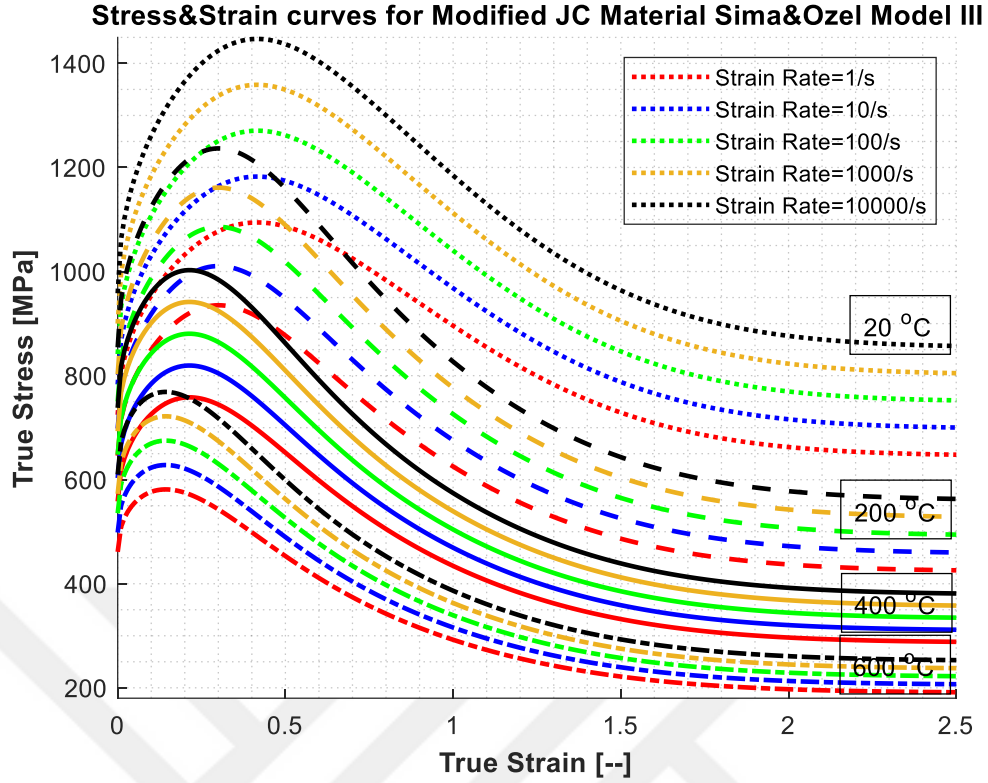


Figure 3.3.13 Stress&Strain curves for Modified JC Material Sima&Ozel Model III at different temperature and strain rate [49]

The Sima&Ozel model III is given below:

$$\sigma = \left[A + B\varepsilon^n \left(\frac{1}{\exp(\varepsilon^a)} \right) \right] \left[1 + C \ln \frac{\dot{\varepsilon}}{\dot{\varepsilon}_0} \right] \left[1 - \left(\frac{T - T_r}{T_m - T_r} \right)^m \right] \left[D + (1 - D) \left[\tanh \left(\frac{1}{(\varepsilon + p)^r} \right) \right]^s \right]$$

where $D = 1 - \left(\frac{T}{T_m} \right)^d$, and $p = \left(\frac{T}{T_m} \right)^b$.

In this model III, the exponent parameter S defines thermal softening. The new term is shown in the equation which includes the thermal and strain softening phenomenon that can be seen in Figure 3.3.13. The new term is controlling the softening behavior at a specific strain range. Table 3.3.3 shows all the parameters used in the Sima&Ozel model I, II and III.

Modified J-C Model Proposed by Yigit Karpat [47]

Another modification to the J-C material model is proposed by Karpat [47, 48]. This material model considers strain softening as a function of temperature, and it was developed such that the influence of strain softening decreases as temperature decreases. The model also considers the coupling relationship between strain and strain rate.

The Karpat model defined as [47]:

$$\sigma = (A\varepsilon^{n^*} + B)(cT_*^2 + dT_* + e) \left(1 - \left[1 - \left(\frac{\ln(\dot{\varepsilon}_0)}{\ln(\dot{\varepsilon})} \right)^q \right] \left[\frac{1}{l \times \tanh(\varepsilon + p)} \right] \right)$$

and $T_* = \frac{T}{T_r}$.

In the model proposed by Karpat, there exist a flow softening function, which starts after a critical strain and temperature. The flow stress under various temperature for Karpat model at a strain rate of 10000 (1/s) is shown in Figure 3.3.14.

$$\sigma_{soft}(\varepsilon, \dot{\varepsilon}, T) = \sigma - (\sigma - \sigma_s)(\tanh(k\varepsilon^*))^r$$

This function is integrated into Karpat modified model equation. After a critical strain value, the proposed function controls the softening behavior of the material. For strain values less than the critical strain value, Karpat modified model equation is valid [47].

Table 3.3.4 Parameters of Yigit Karpat Modified JC Material Model [47]

A (MPa)	n*	B (MPa)	c	d
590	0.27	740	7.1903e-5	-0.0209
q	l	p	$\dot{\varepsilon}_0$ (1/s)	e
0.035	1.1	0.08	800	1.6356

The parameters of Yigit Karpat material model is shown in Table 3.3.4.

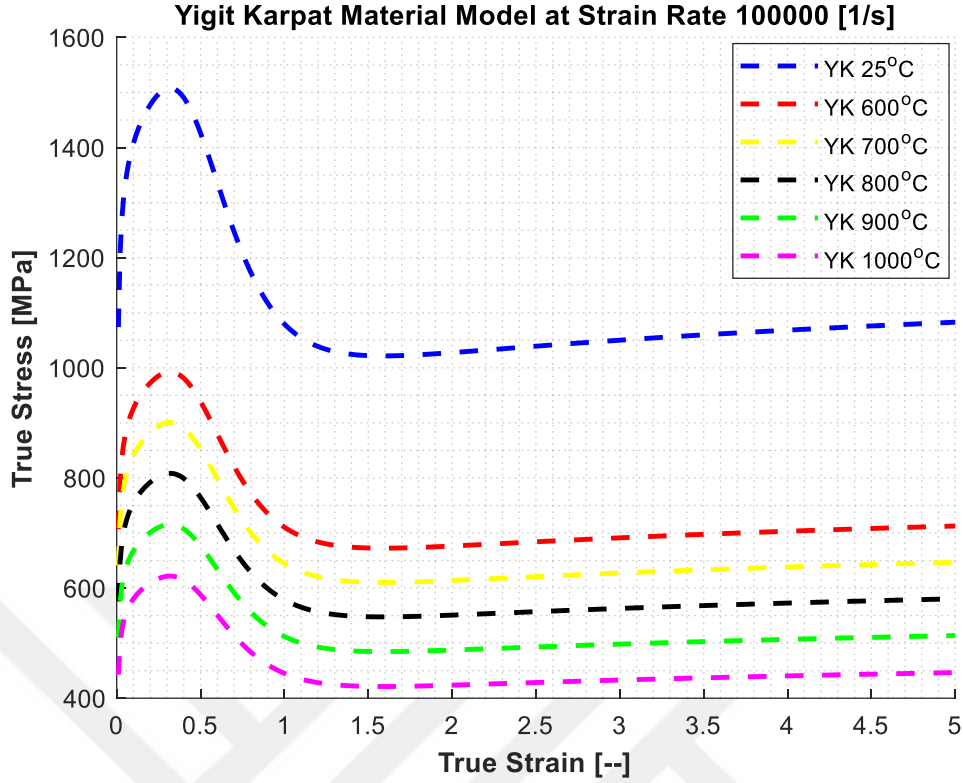


Figure 3.3.14 Stress&Strain curves of Yigit Karpat material model at a strain rate of 10^5 s^{-1} and different temperatures [47]

Power-Law Material Model with Temperature Dependent Damage [5]

The constitutive material model based on the Power Law which includes strain, strain rate and temperature was also considered. Strain hardening and strain rate sensitivity and temperature dependent damage is described by the following [5]:

$$\sigma = f(\varepsilon^p)\Theta(T)\Gamma(\dot{\varepsilon})\varepsilon_{f0}^p$$

$f(\varepsilon^p)$ is the power law strain hardening defined as:

$$f(\varepsilon^p) = \sigma_0 \left(1 + \frac{\varepsilon^p}{\varepsilon_0^p} \right)^{\frac{1}{n}}$$

where, σ_0 is the initial yield strength of Ti-6Al-4V (968 MPa), ε^p is the equivalent plastic strain, ε_0^p is the reference plastic strain (10^{-3}) and n is the strain hardening exponent which is set to 20. Thermal softening term $\Theta(T)$ is defined as a fourth-order polynomial function of temperature as follows as:

$$\Theta(T) = c_0 + c_1T + c_2T^2 + c_3T^3 + c_4T^4$$

The coefficient of the polynomial is given in Table 3.3.5. The rate sensitivity $\Gamma(\dot{\epsilon})$ is a power-law term defined as follows:

$$\Gamma(\dot{\epsilon}) = \left(1 + \frac{\dot{\epsilon}}{\dot{\epsilon}_0}\right)^{\frac{1}{m}}$$

where $\dot{\epsilon}$ is the strain rate, $\dot{\epsilon}_0$ is the reference strain rate (1 s^{-1}) and m is the rate sensitivity coefficient, which is set to 50.5. The damage also defined as a fourth-order polynomial function of temperature as follows as:

$$\epsilon_{f0}^p = d_0 + d_1T + d_2T^2 + d_3T^3 + d_4T^4$$

The damage coefficients are given in Table 3.3.5. The flow stress under various temperatures for the Power law at a strain rate of 10000 ($1/\text{s}$) is shown in Figure 3.3.15.

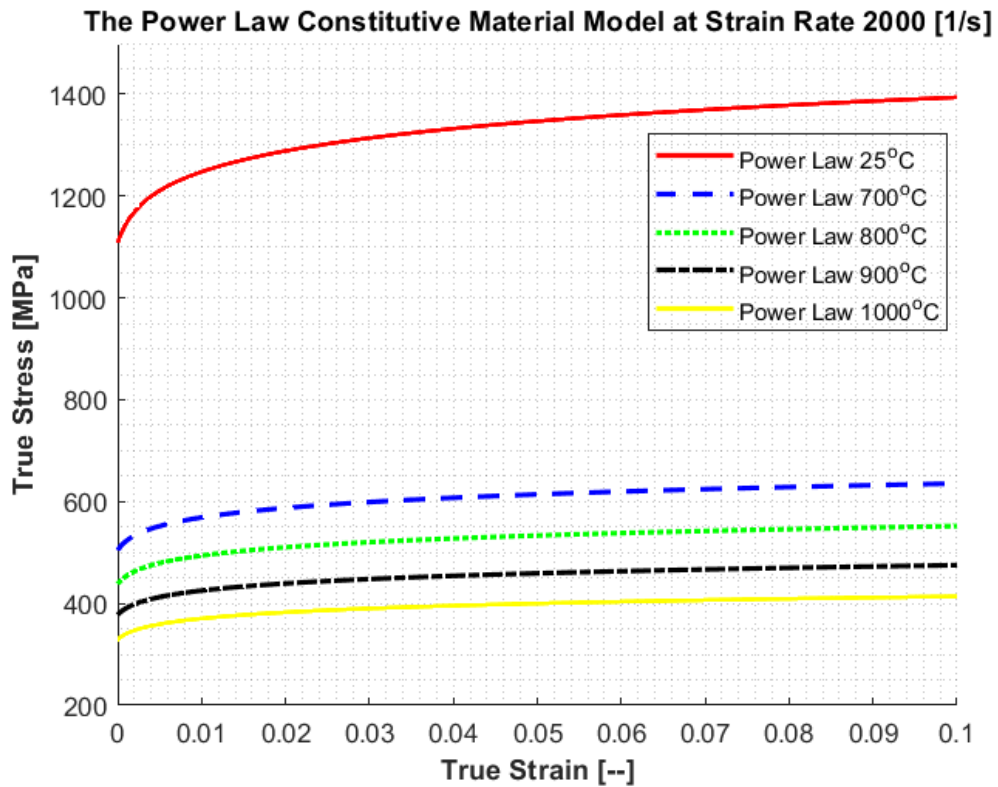


Figure 3.3.15 Stress&Strain curves of at a strain rate of $2 \times 10^3 \text{ s}^{-1}$ and different temperatures [5]

Table 3.3.5 Thermal softening and damage parameters of Power Law [5]

c₀	c₁	c₂	c₃	c₄
1.022	-0.0016	2.45 x 10 ⁻⁶	-2.67x 10 ⁻⁹	1.09 x 10 ⁻¹²
d₀	d₁	d₂	d₃	d₄
0.3033	-0.002784	2.336 x 10 ⁻⁵	-7.728x 10 ⁻⁸	8.632x 10 ⁻¹¹

Damage is the definition of failure when the materials face the high plastic strain than it stands. Damage is very crucial while modeling the machining simulation because machining is itself represent the failure of the workpiece material. It needs to be well defined because the mechanical behavior of shear localization is highly related to elastic to plastic deformation of the workpiece.

Johnson-Cook Material Model with Johnson-Cook Failure Model

The Johnson-Cook material model with J-C damage is another way of simulate the onset of shear localization. The J-C Damage based fracture model is expressed the idea of the cumulative damage law by using equation $w = \sum \frac{\Delta \bar{\epsilon}}{\bar{\epsilon}_f}$ where w is the damage criterion parameter, $\Delta \bar{\epsilon}$ is growth of the effective plastic strain while integrating the cycle and $\bar{\epsilon}_f$ is the effective strain. Damage is initiated when w is reach to 1.

The equation of effective strain is given below:

$$\bar{\epsilon}_f = \left[D_1 + D_2 \exp \left(D_3 \frac{P}{\bar{\sigma}} \right) \right] \left(1 + D_4 \ln \frac{\bar{\epsilon}}{\bar{\epsilon}_0} \right) \left(1 + D_5 \frac{T - T_r}{T_m - T_r} \right)$$

where P is the mean stress of three normal stress, $\frac{P}{\bar{\sigma}}$ is representing stress triaxiality. The fracture strain $\bar{\epsilon}_f$ is calculated by using stress triaxiality, the effective strain rate, the temperature and damage parameters (D_i). The damage parameters (D_i) express the effect of the initial failure strain, exponential constant, triaxiality, strain rate and temperature, respectively. The damage parameters (D_i) can be seen in Table 3.3.6.

Table 3.3.6 Johnson-Cook damage parameters

D₁	D₂	D₃	D₄	D₅
-0.09	0.25	-0.5	0.014	3.87

Energy based failure model is used to model to how material would behave when damage initiate so fracture energy is calculated by using this equation:

$$G_f = \int_{\bar{\epsilon}_0}^{\bar{\epsilon}_f} L\sigma_y d\bar{\epsilon}$$

where $\bar{\epsilon}_0$ is the initial plastic strain which is zero when material deform elastically. J-C damage parameters represent the cumulative fracture of workpiece in the J-C material model. Since, it is not possible to model the fracture only using J-C material model. Any Johnson-Cook material model given at Chapter 3.1 can be used with J-C damage parameters.

J-C Material Model with Cockcroft and Latham Material Failure Criterion

The damage model proposed by Cockcroft and Latham (C&L) proposes that damage initiation depends on the maximum principal stress rather than generalized stress. This damage criterion which considers the crack formation and propagation theory of shear localization been used by Ceretti et al. [25] to model serrated chip formation. This expression for this damage criterion is as follows:

$$\int_0^{\epsilon_f} \sigma^* d\bar{\epsilon} = C$$

where C is the critical value at fracture, σ^* is the maximum principal tensile stress, ϵ_f is a strain at fracture and $\bar{\epsilon}$ is the effective strain. The parameter (C) is calculated by integrating of the stress and strain curve of the material.

The Khan–Huang–Liang (KHL) Constitutive Material Model

This KHL model was created by using experimental data of compression test responses which is quite good to understand the mechanical properties of the materials [63].

$$\sigma = \left[A + B \left(1 - \frac{\ln \dot{\epsilon}}{\ln D_0} \right)^{n_1} \epsilon^{n_0} \right] \left(\frac{\dot{\epsilon}}{\dot{\epsilon}_0} \right)^C \left(\frac{T_m - T}{T_m - T_r} \right)^m$$

In this equation, D_0 is the non-dimensional constant which is changing the strain rate term. Other parameters are just parameters to predict the mechanical behavior of the material. One of the optimization methods was used to get these parameters and they tried to decrease calculation errors between experimental and KHL model flow stress data that is why they choose to use the Genetic Algorithm optimization method to get best-fit parameters.

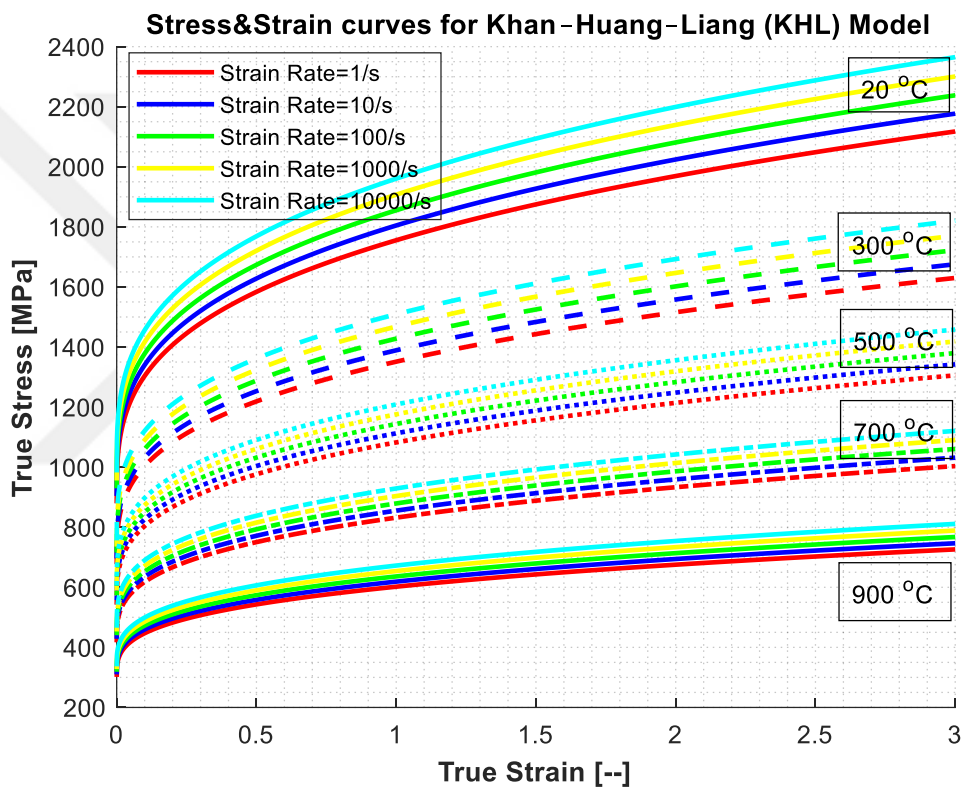


Figure 3.3.16 Stress&Strain curves for KHL Model at different temperature and strain rate [63]

Figure 3.3.16 shows the predicted flow stress at different temperatures and strain rates. The parameter of n_1 is equal to zero which means that changing in strain rate does not affect material behavior overall.

Table 3.3.7 Parameters of KHL Constitutive Material Model [63]

A (MPa)	B (MPa)	n_0	C	m	n_1
878.452	874.778	0.315	0.012	1.417	0

This optimized KHL model predicts flow stress accurately at a wide range of temperature, strain and strain rate effect. Table 3.3.7 shows the parameters of the optimized KHL material model.

The Modified KHL (MKHL) Material Model

Although the KHL model is quite efficient to predict stress and the strain hardening rate of the predicted flow stress, the model is not highly efficient with predicting experimental data at elevated temperatures. That is why they modified the KHL model due to the absence of temperature effect accurately. They realized that the strain hardening effect of the experimental flow stress is smaller than the KHL predicted flow stress at elevated temperatures. Strain hardening effect with increasing with temperature is added as temperature multiplier function and defined as [63]:

$$\sigma = \left[A + B \left(1 - \frac{\ln \dot{\epsilon}}{\ln D_0} \right)^{n_1} \left(\frac{T_0 - T/2}{T_0} \right)^{n_2} \epsilon^{n_0} \right] \left(\frac{\dot{\epsilon}}{\dot{\epsilon}_0} \right)^C \left(\frac{T_m - T}{T_m - T_r} \right)^m$$

where T_0 is between 450° and 700° celsius, the reference strain rate is defined as 1 s^{-1} . The other constants are defined in the material model was optimized again using Genetic Algorithm. All MKHL parameters can be seen in Table 3.3.8. Figure 3.3.17 shows the predicted flow stress at different temperatures and strain rates. MKHL model represent better the mechanical behavior of the material at elevated temperatures.

Table 3.3.8 Parameters of Modified KHL Constitutive Material Model

A (MPa)	B (MPa)	n_0	C	m	n_1	n_2	T_0 ($^\circ\text{C}$)
872.791	906.428	0.327	0.011	1.211	0.012	0.214	456.453

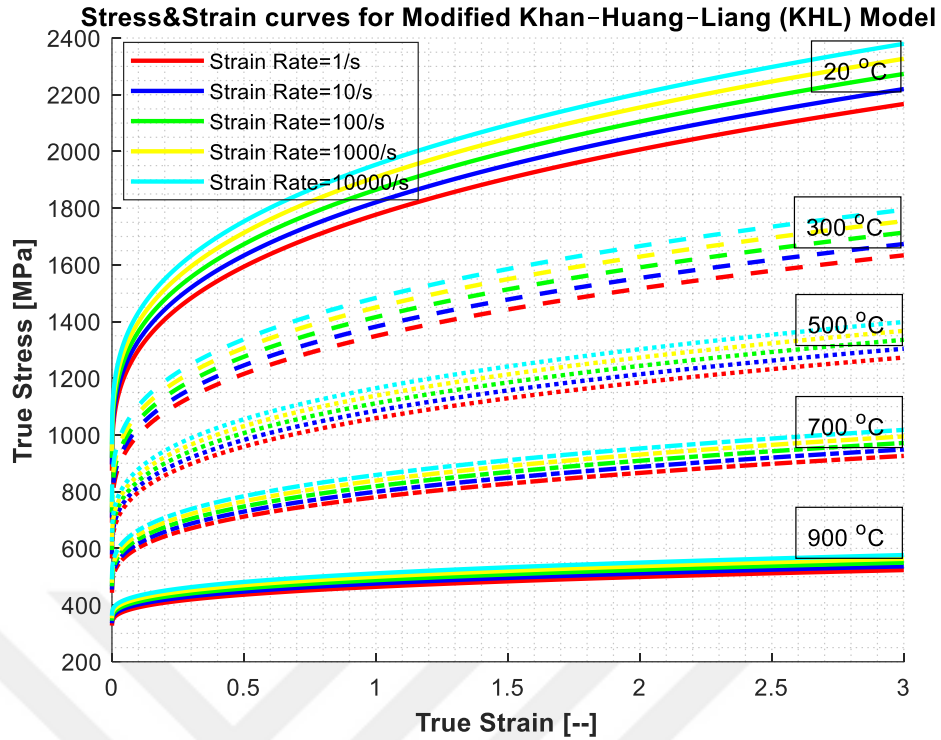


Figure 3.3.17 Stress&Strain curves for Modified KHL Model at different temperature and strain rate [63]

3.4 Friction Modeling

The friction between tool and workpiece is a very important and complicated mechanism. The chip and tool contact face is known as a rake face. Friction at the rake face has a huge effect on temperature, wear mechanism, chip segmentation and burr formation. Therefore, the finite element model needs to be improved to get better cutting force and temperatures by taking into account the friction mechanisms between tool and chip or workpiece. The most commonly used friction theory is coulomb friction model and its defined as:

$$\tau = \mu\sigma$$

In this equation, the friction coefficient (μ) is all constant along the cutting surface which means it does not change along by temperature, strain rate, etc. The shear stress (τ) is equal to multiply principal stress with friction coefficient. The stress value between tool and workpiece needs to be several times higher than the ultimate tensile stress to cut the material. In the orthogonal turning metal cutting, the contact at the rake face mostly occurs in the sticking region which sliding takes place in that region.

The frictional force is linearly independent of feed and thrust force but is linearly dependent on the contact area of the rake face.

Friction at tool/chip and tool/workpiece interface has a significant effect on the prediction of machining process outputs. In order to determine the Coulomb friction coefficient, net cutting force (F_c^c) and thrust force (F_t^c) components are obtained by subtracting ploughing forces (F_c^p, F_t^p) from measured forces (F_c^m, F_t^m) as explained by Guo and Cho [64]:

$$F_c^c = F_c^m - F_c^p$$

and

$$F_t^c = F_t^m - F_t^p$$

The components of the ploughing forces (F_c^p, F_t^p) are obtained using the method of extrapolation to a zero uncut chip thickness. The Coulomb friction model using net cutting and thrust force components is used as follows

$$\mu = \frac{F_c^c \sin \gamma + F_t^c \cos \gamma}{F_c^c \cos \gamma - F_t^c \sin \gamma}$$

where γ is the rake angle of the cutting tool.

CHAPTER 4

4. EXPERIMENTAL PROCEDURE AND STUDIES

4.1 Edge radius of the original inserts and modified inserts for Friction modeling

The edge radius of the uncoated tungsten carbide insert (Sandvik DCMW11 T304H13A) is measured for onset of shear localization experiment. Moreover, the edge radius of the uncoated tungsten carbide insert (Sandvik DCMW11 T304H13A) is modified by using a grinding machine to get three different rake angles (0° , 4° and 8°) to identify the effect of ploughing force on friction.

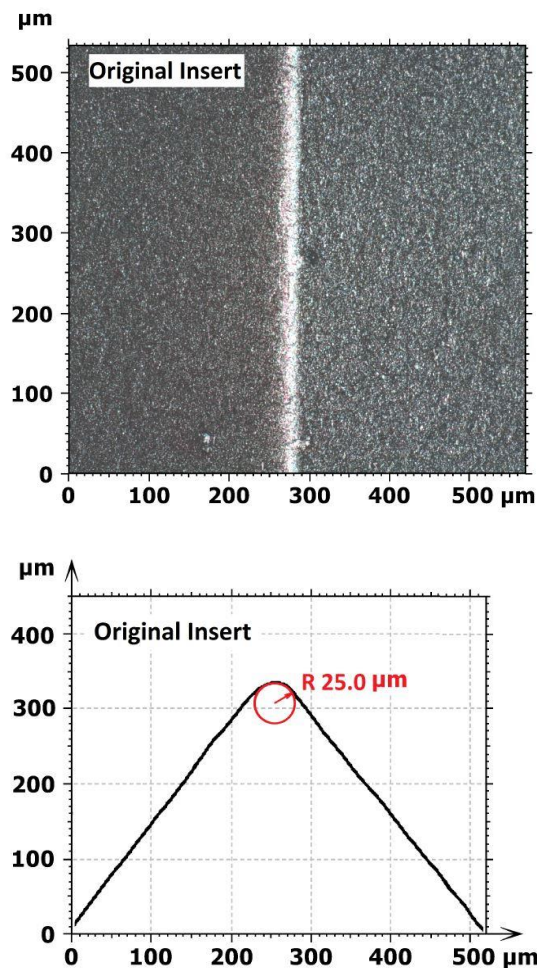


Figure 4.1.1 Edge radius measurement of the original insert [3]

A laser scanning microscope (Keyence VK-X100) was used to measure edge radius. The clearance angle of the insert was not modified and it is the same as the original

inserts clearance angle 7° degree. The microscope image of the original insert can be seen in Figure 4.1.1. Edge radii of the three inserts were measured 5, 5 and 7.5 micrometers respectively.

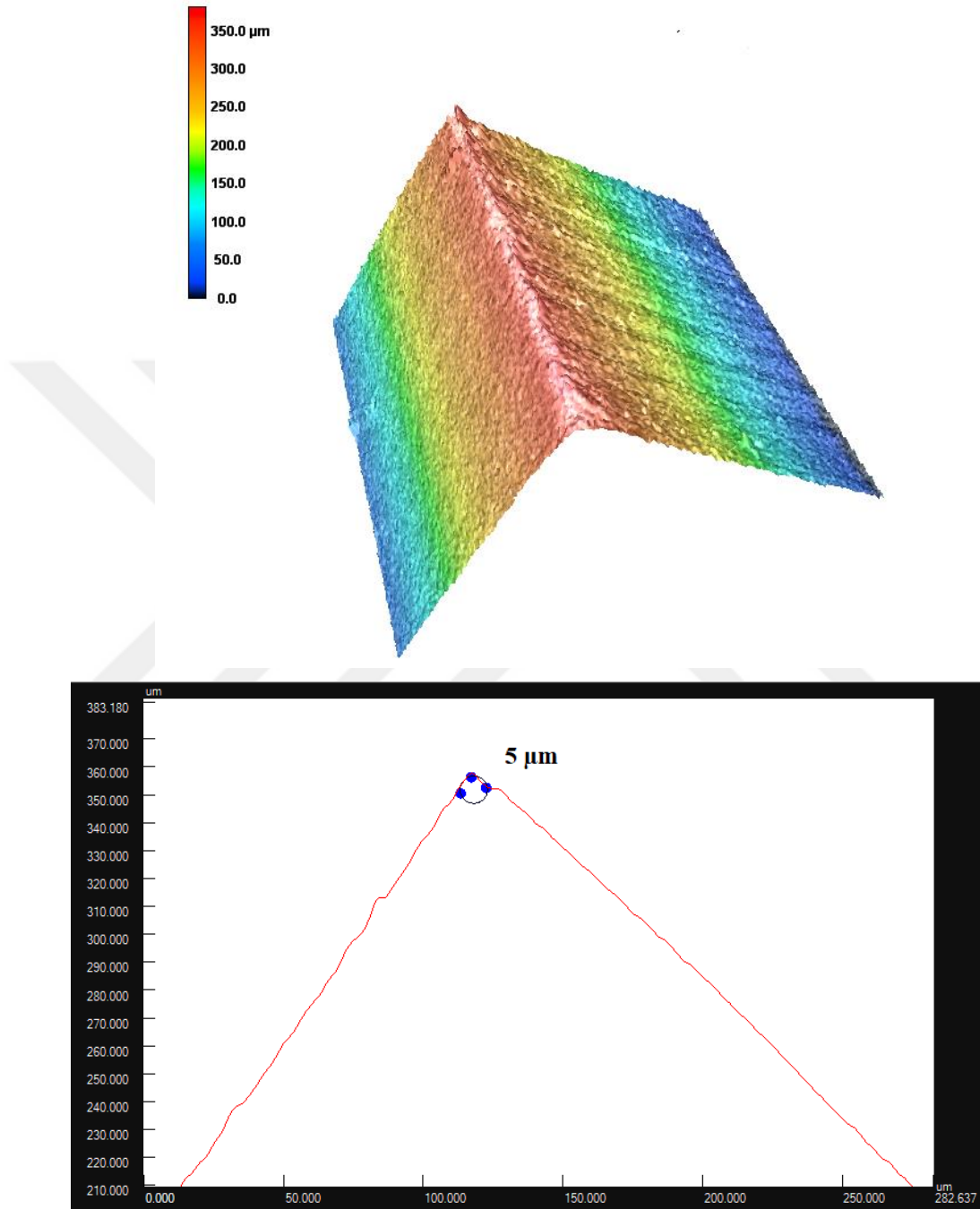


Figure 4.1.2 Edge radius measurement of the 0° rake insert after edge preparation

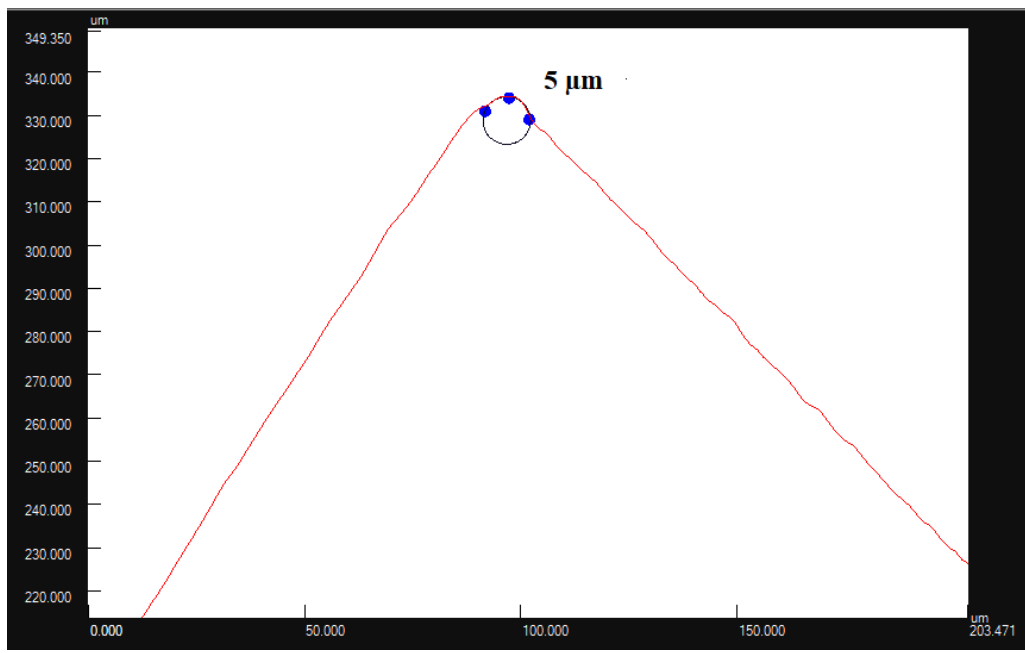
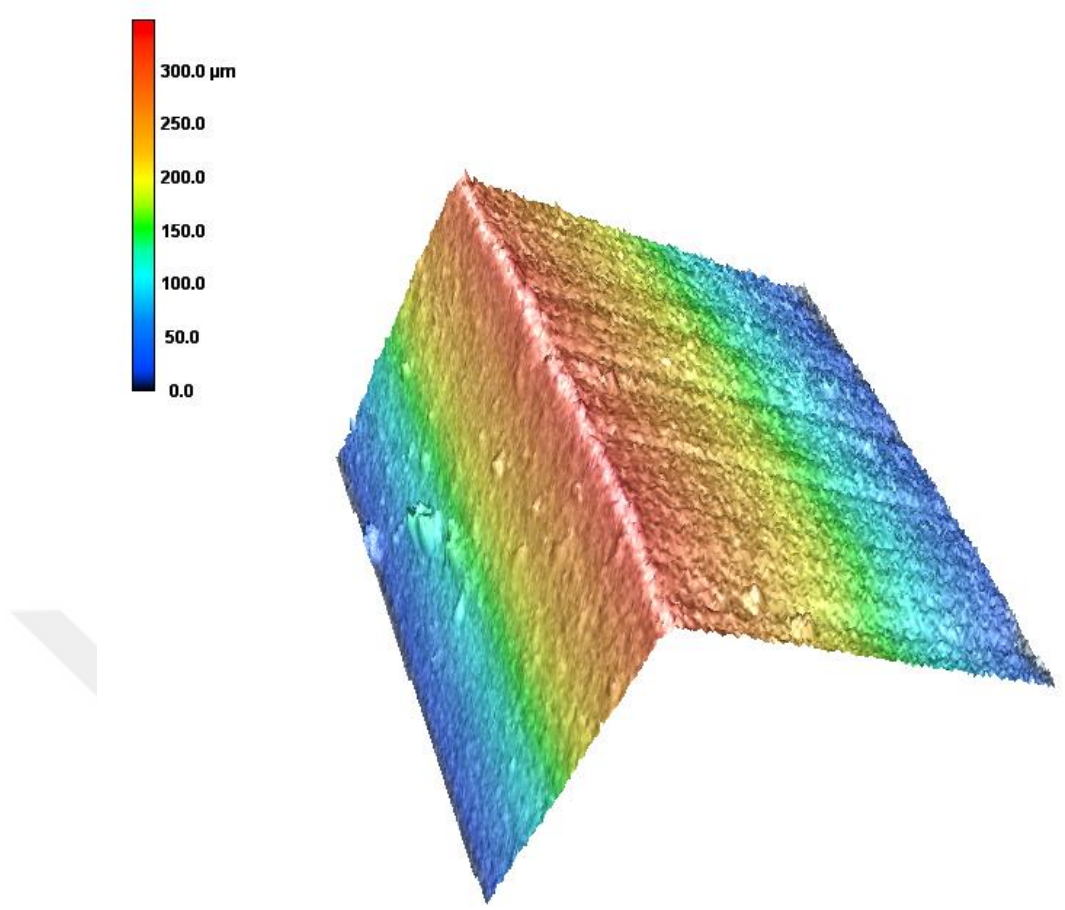


Figure 4.1.3 Edge radius measurement of the 4° rake insert after edge preparation

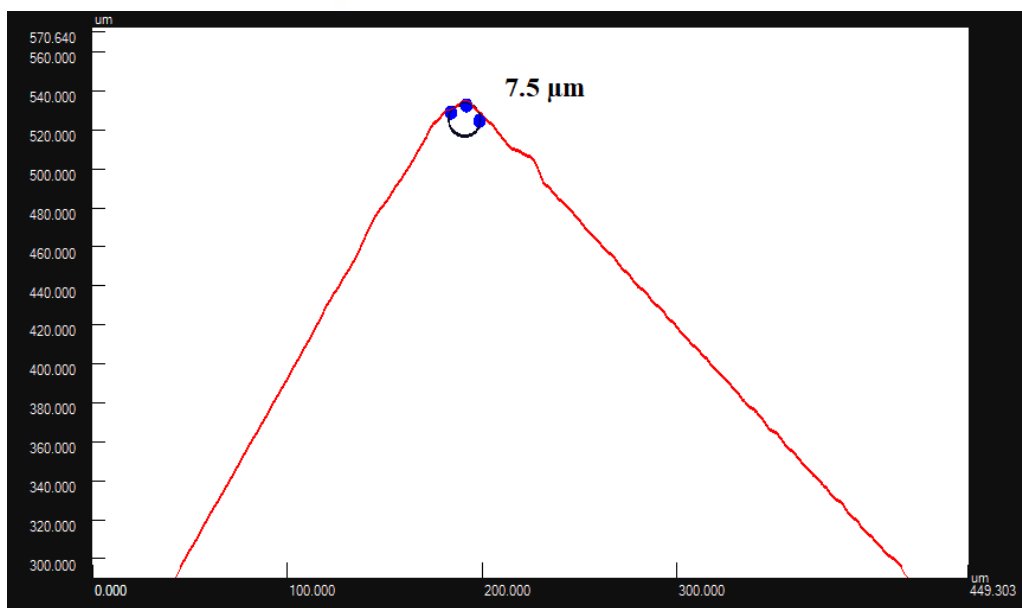
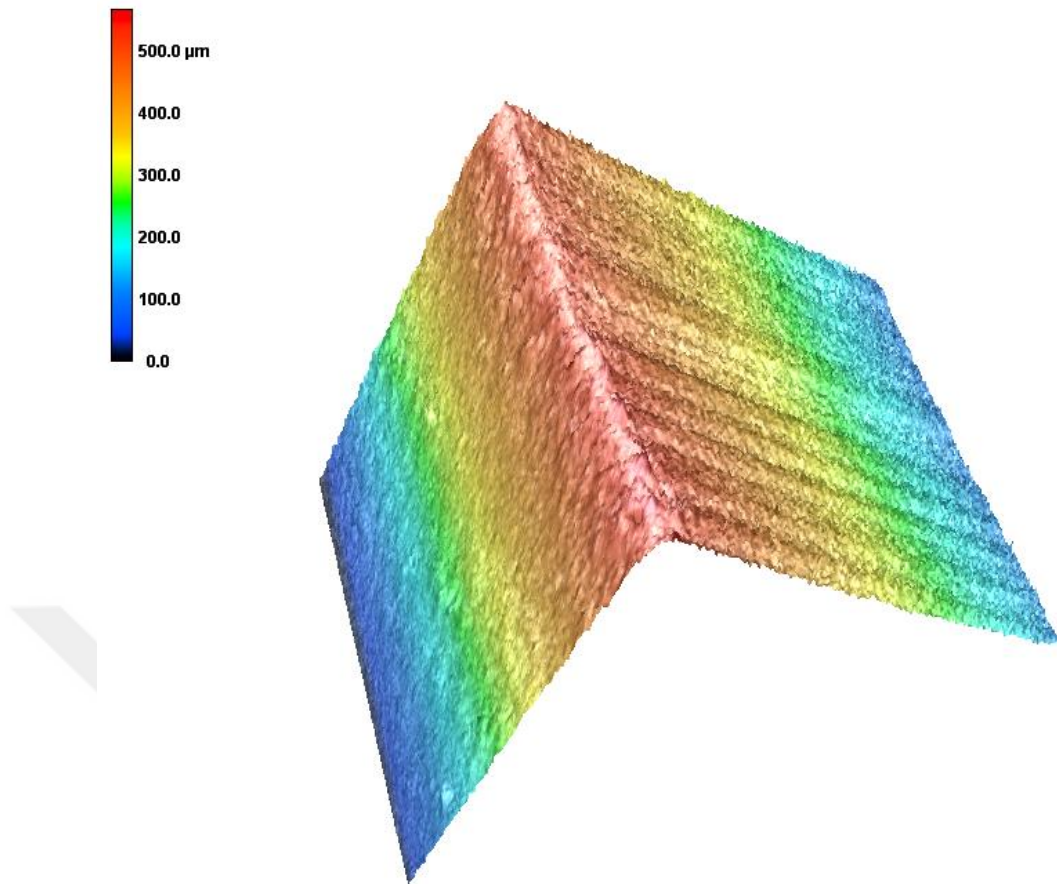


Figure 4.1.4 Edge radius measurement of the 8° rake insert after edge preparation

The laser scanning microscope image of the modified inserts after edge preparation can be seen in Figure 4.1.2, Figure 4.1.3, and Figure 4.1.4.

4.2 Experimental Procedure for Orthogonal Cutting Experiments

The cutting experiments were performed on Akira Seiki Performa Vertical Machining Center (SR2XP) with the BT40 type tool holder. This CNC device is equipped with a spindle with a maximum rotational speed of 11000 revolutions per minute. Titanium Ti-6Al-4V rod 18 mm outer and 16 mm inner diameter were prepared. Titanium specimen rods had 1 mm wall thickness. The depth of the hole was kept at 4 mm maximum due to avoid vibration. The edge radius of the inserts are measured by 3D laser scanning microscope as 25 μm as depicted in Figure 4.1.1. Tool inserts were held by SDACR 1616K 11S tool holder and machining forces are measured using a quartz 3-component dynamometer (Kistler-9265B) with a tool holder type 9441 B, connected to a Kistler charge amplifier (Type 5070) and Kistler DAQ (Type 5697) as shown in Figure 4.2.1.

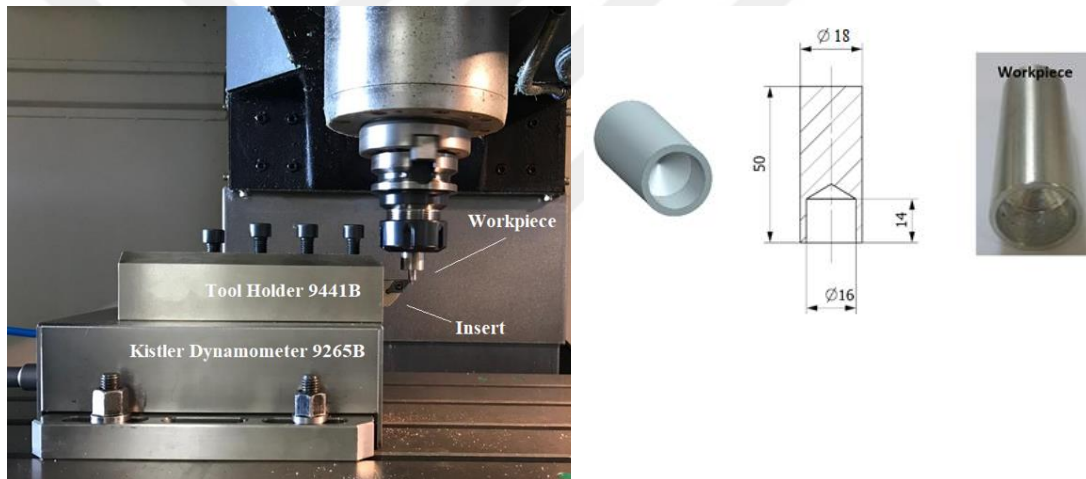


Figure 4.2.1 The experimental setup used for orthogonal cutting experiments

Orthogonal cutting experiments are done using an uncoated tungsten carbide insert (DCMW 11 T3 04H13A) of 0° rake angle and 7° clearance angle.

Table 4.2.1 The experimental conditions of orthogonal cutting experiments

Rake and Clearance Angle	Uncut Chip Thickness [49]	Cutting Edge Radius [μm]	Cutting Speed [m/min]
0° and 7°	0.1	25	2 to 60

A turning tool holder with a cross-section of 30×30 mm and minimum possible overhang is used to ensure a higher rigidity and to minimize cutting tool vibrations. The cutting process is planned for a short period of time (~5 sec.) to eliminate the effect of tool wear. For each experiment, an up-sharp cutting tool is used. The cutting experiments are started at a cutting speed of 60 m/min and has been reduced to about 2 m/min. Experimental test conditions are represented in Table 4.2.1. The experiments at high cutting speeds are used to check the validity of the FEM models and those at lower cutting speeds are used to determine the onset of shear localization. The chips are collected after orthogonal cutting experiments and are mounted using conductive polymer (Phenolic hot mounting resin with carbon filler-PolyFast). The polymer mounted chips are ground using 360, 800, 1200 and 2500 grinding papers. After grinding operations, all the chips are polished using 1 μm Alumina Oxide solution. Etching solution containing 37.5 ml H₂O, 7.5 ml HNO₃ and 5 ml HF is used to reveal the microstructure of the chips. The etched microstructure of the chips is examined using the scanning electron microscope to find the onset of shear localization. Examples of chip microstructures are shown in Figure 4.2.2 and Figure 4.2.3. Adiabatic shear bands are observed at higher cutting speeds, while no shear localization exists at a cutting speed of 2.82 m/min. Therefore, the value of 2.82 is accepted as the critical cutting speed for shear localization onset. It is worth mentioning that, this critical cutting speed is for the cutting tool of 0° rake angle, 7° clearance angle and edge radius of 25 μm for an uncut chip thickness of 0.1 mm. Any change in the cutting tool geometry and cutting conditions will alter the critical cutting speed for the shear localization onset.

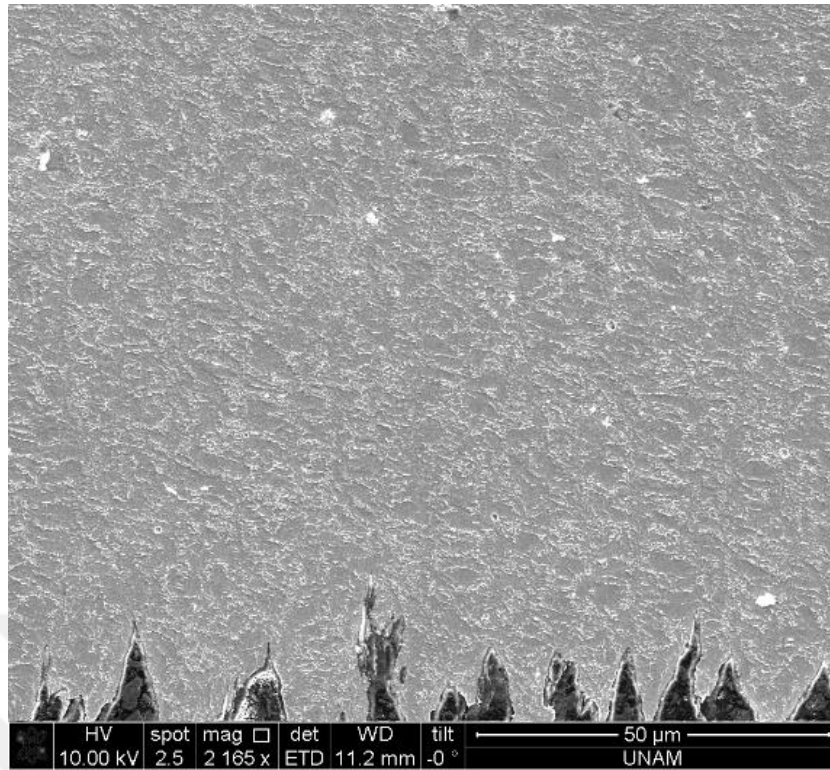


Figure 4.2.2 Chip cross section obtained at a cutting speed of 2.82 m/min

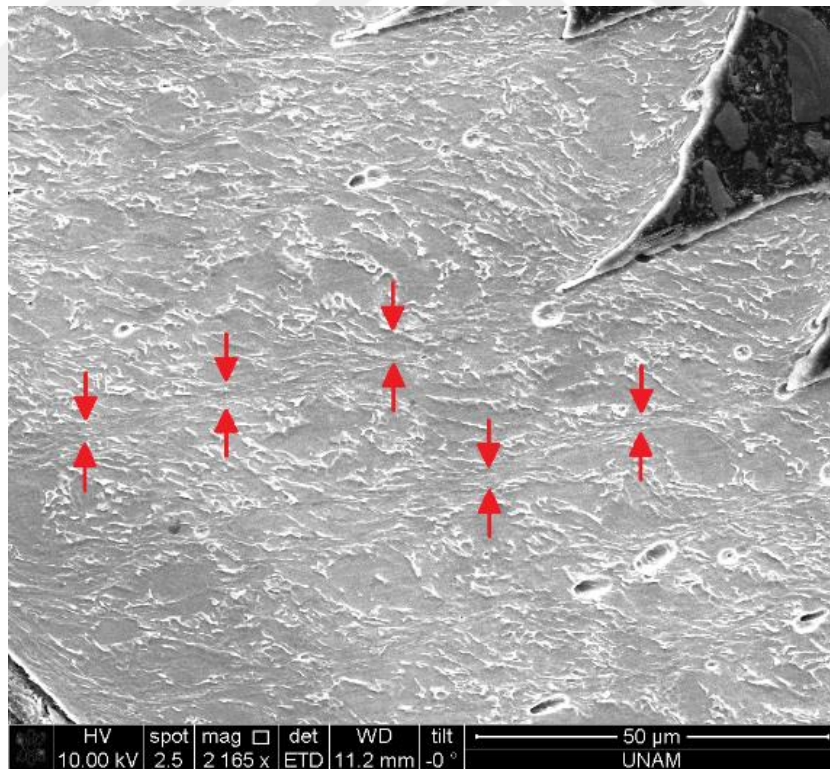


Figure 4.2.3 Chip cross section obtained at a cutting speed of 40 m/min

4.3 Influence of Ploughing Cutting and Thrust Force on Coulomb Friction Coefficient

For different uncut chip thickness (0.05, 0.075, 0.1 and 0.15), the cutting and thrust force were measured in orthogonal cutting of Ti-6Al-4V using modified inserts having different rake angles 0° , 4° and 8° degrees. These inserts have different edge radii of 5,5 and 7.5 micrometers. Both force components increase when increasing uncut chip thickness as expected.

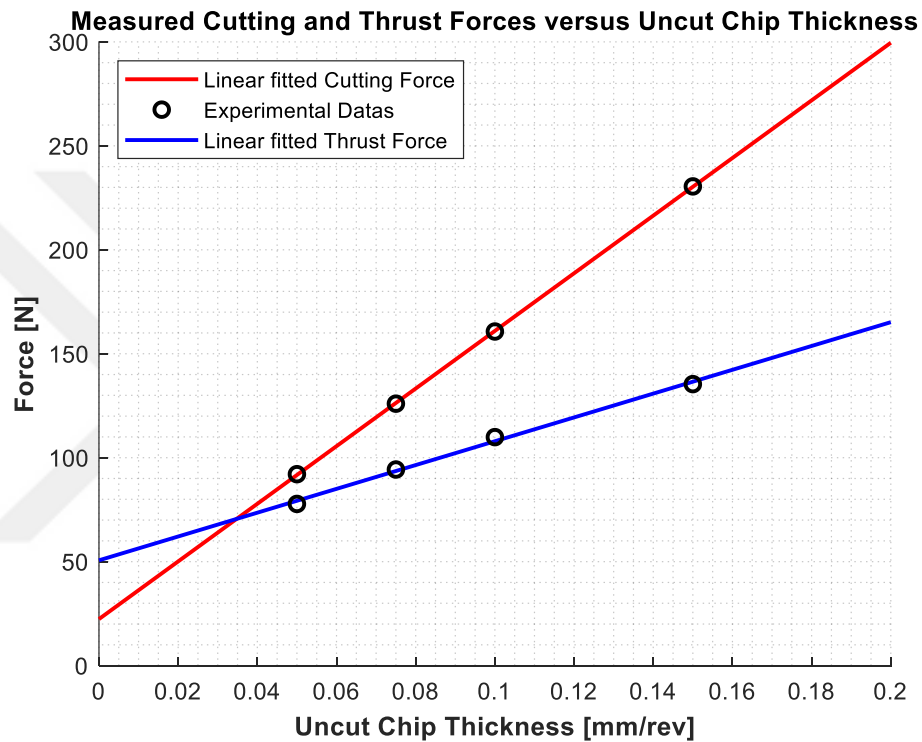


Figure 4.3.1 Extrapolated Cutting and Thrust Forces versus Uncut Chip Thickness with 0° rake angle modified insert, Cutting Speed 40 m/min

Experimental test conditions are represented in Table 4.3.1.

Table 4.3.1 The experimental conditions of orthogonal cutting experiments

Rake Angle	Uncut Chip Thickness [49]	Cutting Edge Radius [μm]	Cutting Speed [m/min]
0° , 4° and 8°	0.05, 0.075, 0.1 and 0.15	5, 5 and 7.5	1 and 40 (for 3 modified inserts)

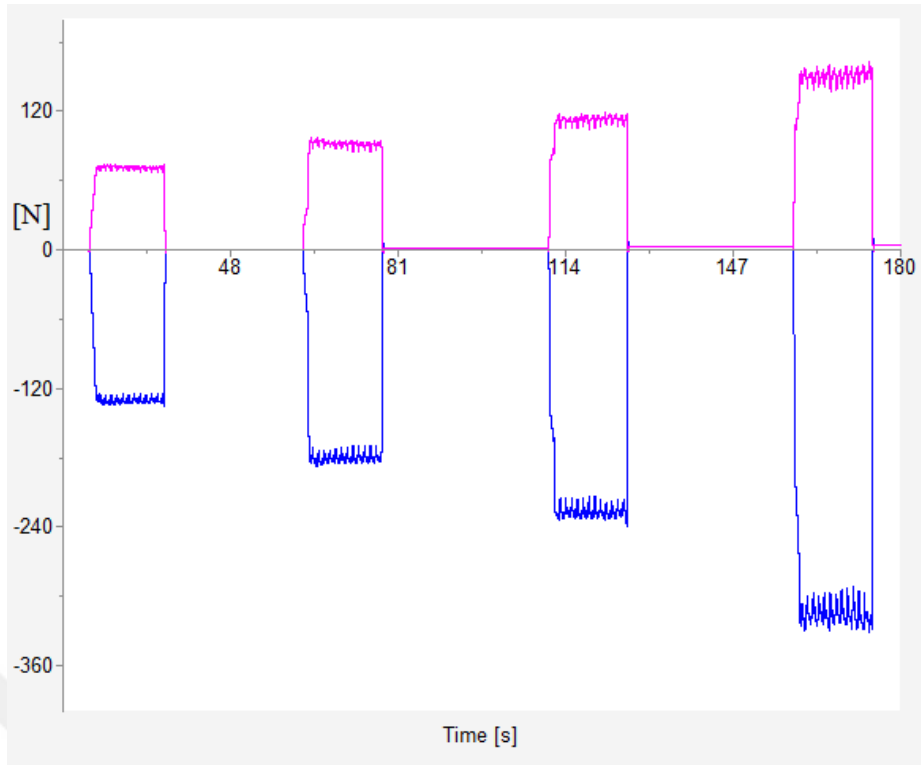


Figure 4.3.2 Measured Cutting (blue) and Thrust Forces (pink) versus Uncut Chip Thickness (0.05, 0.75, 0.1 and 0.15) with 0° rake angle insert, $V_c = 1$ m/min

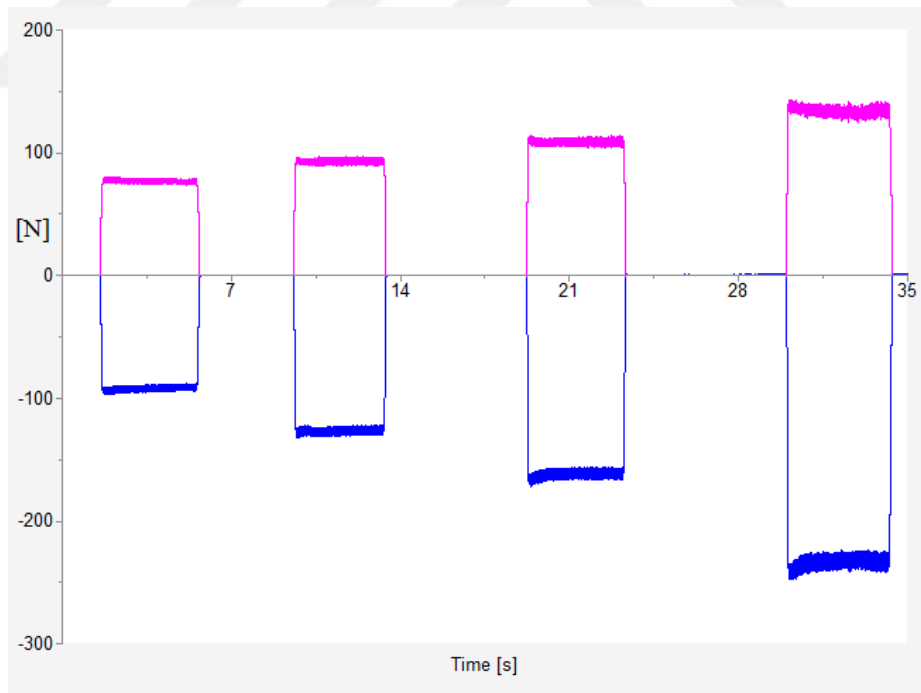


Figure 4.3.3 Measured Cutting (blue) and Thrust Forces (pink) versus Uncut Chip Thickness (0.05, 0.75, 0.1 and 0.15) with 0° rake angle insert, $V_c = 40$ m/min

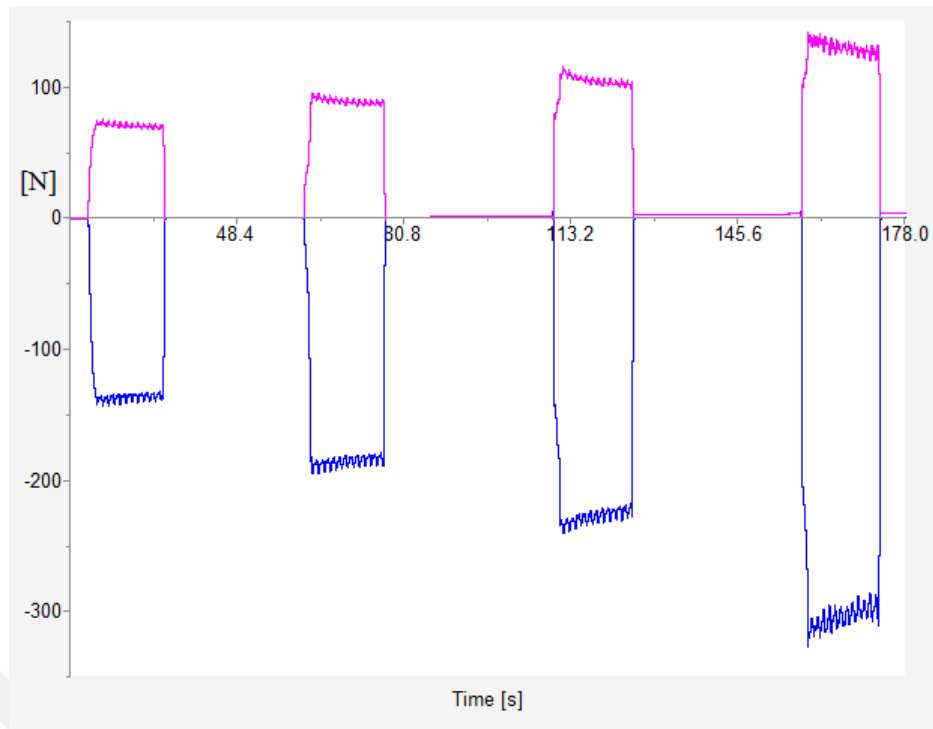


Figure 4.3.4 Measured Cutting (blue) and Thrust Forces (pink) versus Uncut Chip Thickness (0.05, 0.75, 0.1 and 0.15) with 4° rake angle insert, $V_c = 1$ m/min

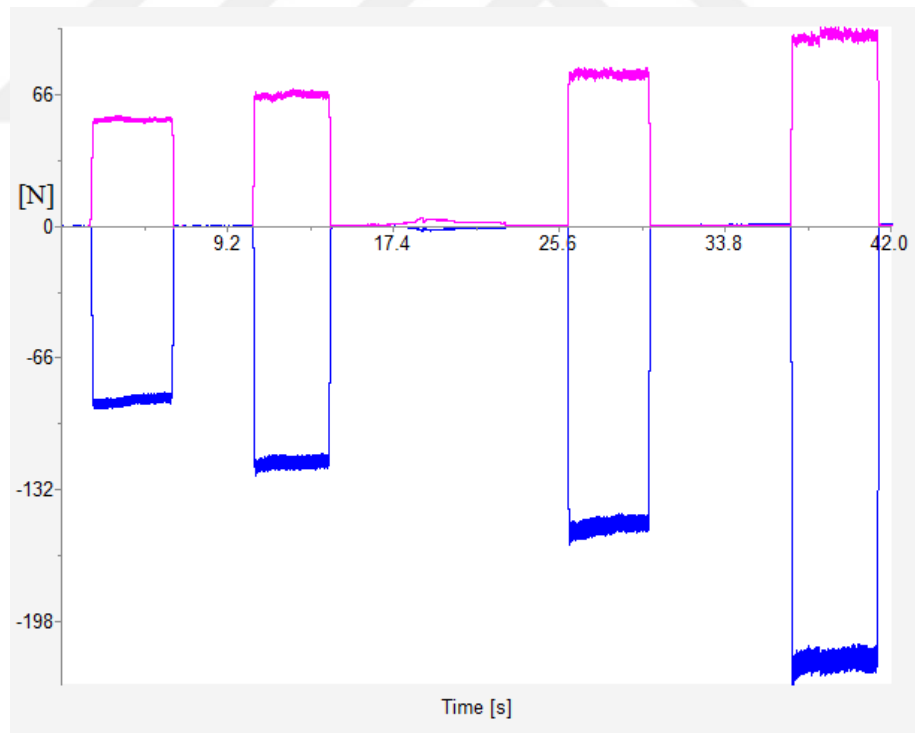


Figure 4.3.5 Measured Cutting (blue) and Thrust Forces (pink) versus Uncut Chip Thickness (0.05, 0.75, 0.1 and 0.15) with 4° rake angle insert, $V_c = 40$ m/min

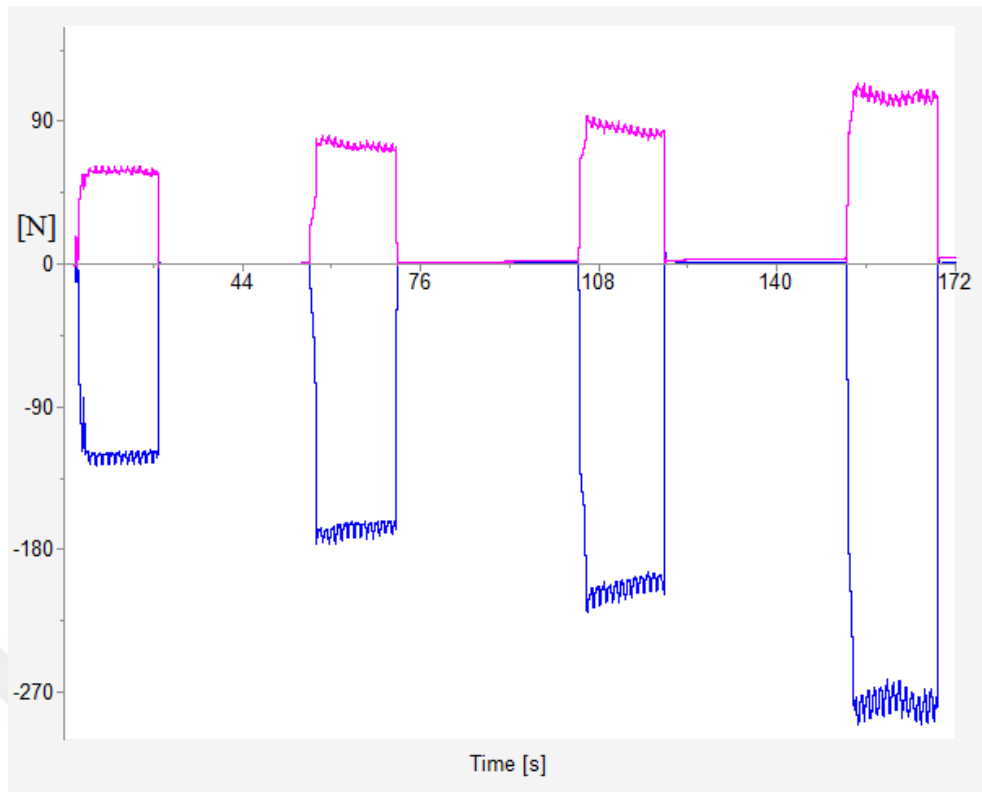


Figure 4.3.6 Measured Cutting (blue) and Thrust Forces (pink) versus Uncut Chip Thickness (0.05, 0.75, 0.1 and 0.15) with 8° rake angle insert, $V_c = 1$ m/min

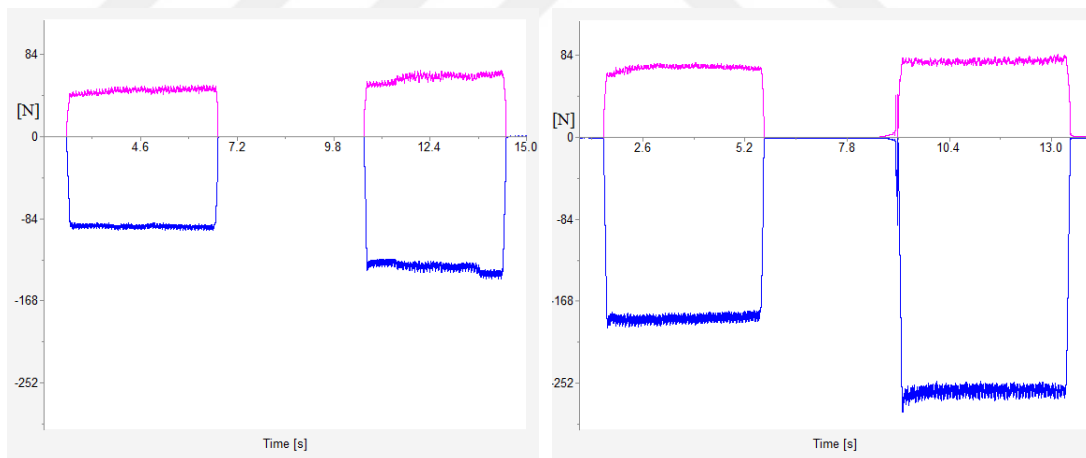


Figure 4.3.7 Measured Cutting (blue) and Thrust Forces (pink) versus Uncut Chip Thickness (0.05, 0.75, 0.1 and 0.15) with 8° rake angle insert, $V_c = 40$ m/min

For the calculation of ploughing forces from measured force data, the linear extrapolation method was used. The method is based on the assumption that the cutting and thrust forces increase linearly while increasing uncut chip thickness. Cutting and thrust forces are influenced by the ploughing forces due to the edge radius of the tool and it is assumed that ploughing force is fully engaged in all orthogonal cutting tests.

Therefore, ploughing forces don't change while increasing uncut chip thickness so friction coefficient on the tool-chip interface is independent of uncut chip thickness.

Table 4.3.2 Coulomb Friction Coefficient using modified inserts with 0°, 4° and 8° rake angle at Cutting Speed of 1 and 40 m/min

	Velocity (m/min)	Uncut Chip Thickness (mm/rev)	Feed Rate (mm/min)	Thrust Force F_t (N)	Cutting Force F_c (N)	Ploughing Forces (N)	Coulomb Friction
Rake Angle 0°	1	0.05	2.65	74.18	132.1	$F_{pt} = 44.47$ $F_{pc} = 33.65$	0.43
		0.075	4	95.1	182.4		
		0.1	5.3	115.7	227.5		
		0.15	7.95	151.9	314.1		
	40	0.05	49	77.77	92.08	$F_{pt} = 22.39$ $F_{pc} = 50.7$	0.41
		0.075	73.5	94.32	126		
		0.1	98	109.9	160.7		
		0.15	147	135.4	230.5		
Rake Angle 4°	1	0.05	2.65	71.84	136.4	$F_{pt} = 44.51$ $F_{pc} = 57.59$	0.44
		0.075	4	90.03	185.1		
		0.1	5.3	106.1	227.4		
		0.15	7.95	131.5	303.9		
	40	0.05	49	54.87	86.79	$F_{pt} = 34.64$ $F_{pc} = 20.82$	0.41
		0.075	73.5	67.7	117.8		
		0.1	98	77.6	149		
		0.15	147	98	216.4		
Rake Angle 8°	1	0.05	2.65	60.92	120.9	$F_{pt} = 42.28$ $F_{pc} = 51.24$	0.45
		0.075	4	77.28	167.3		
		0.1	5.3	88.42	205.2		
		0.15	7.95	105.6	272.4		
	40	0.05	49	49.23	91.17	$F_{pt} = 34.3$ $F_{pc} = 6.1$	0.34
		0.075	73.5	54.94	128.9		
		0.1	98	73.99	184.9		
		0.15	147	79.65	259.2		

Cutting and thrust forces can then be plotted as a linear function to an uncut chip thickness. The ploughing forces can be calculated using a linear function by taking

uncut chip thickness 0 value. For ploughing force values a linear fitting was accomplished. The resulting linear function and line plots can be seen in Figure 4.3.1. The slope of these two lines signifying that the direction of ploughing force changes with the magnitude of the edge radius of the inserts. Measured Cutting and Thrust forces from dynamometers can be seen in Figure 4.3.2, Figure 4.3.3, Figure 4.3.4, Figure 4.3.5, Figure 4.3.6 and Figure 4.3.7.

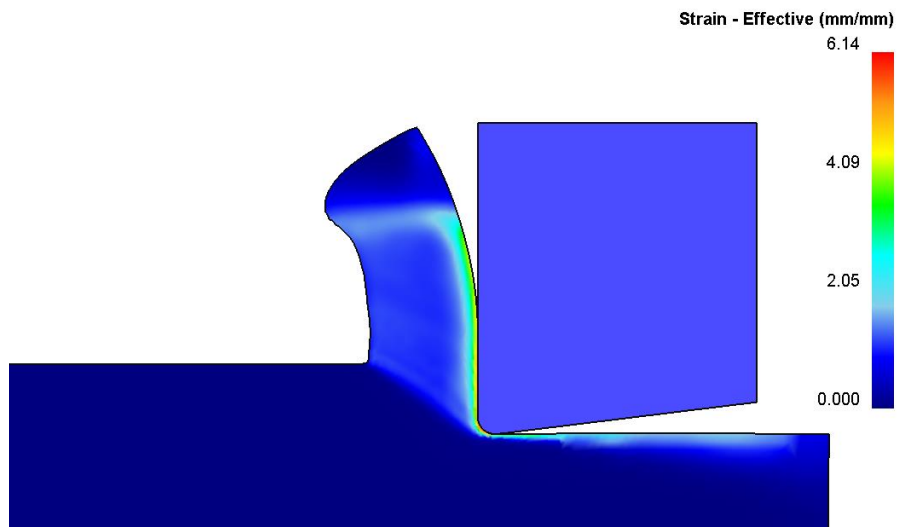
By knowing the magnitude of ploughing cutting and thrust force, it is more accurate to calculate the Coulomb friction coefficient at the tool chip interface. Real chip forming cutting and thrust force are found by subtracting the ploughing forces from measured forces. Now, Coulomb friction at the tool chip interface can be calculated by:

$$\mu = \frac{F_c^c \sin \gamma + F_t^c \cos \gamma}{F_c^c \cos \gamma - F_t^c \sin \gamma}$$

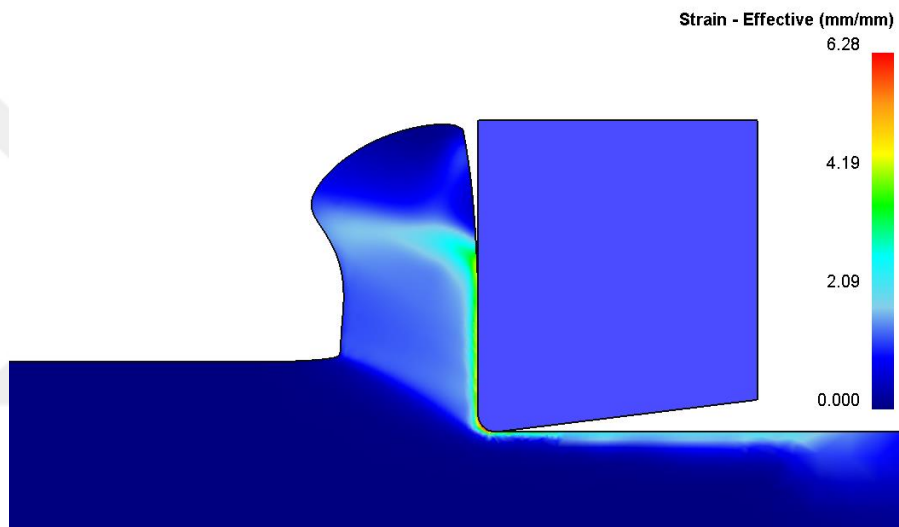
γ is the rake angle of the inserts and forces in the equations are real chip forming force. Table 4.3.2 shows the friction coefficient at different cutting speeds and rake angles. These results are a good agreement with the result NIU et al. [65] where they studied the friction performance of titanium/tungsten carbide pairs under dry sliding conditions using a pin-on-disk method. They obtained dry coefficient friction of 0.42 Titanium/tungsten carbide couple [65].

4.4 Finite Element Simulation of Critical Cutting Speed of Ti-6Al-4V

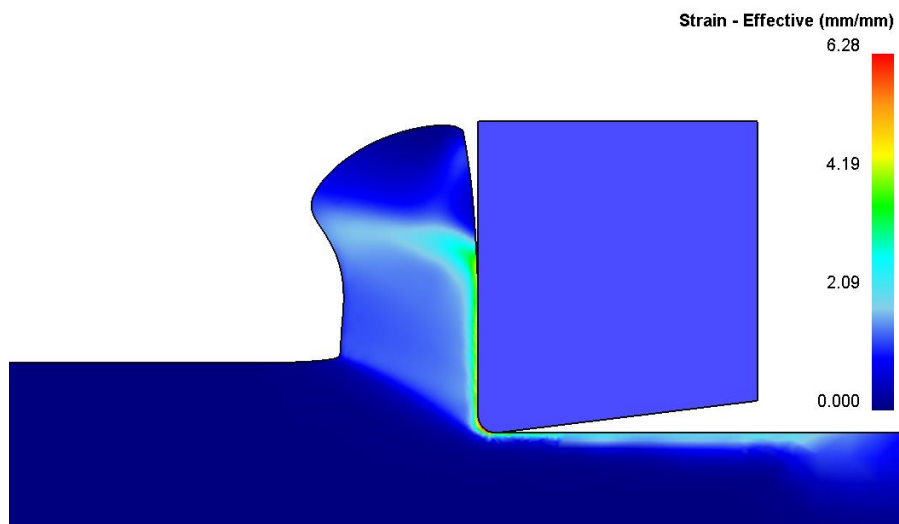
The simulations with Johnson-Cook model show that J-C model alone is not capable of modeling shear localization during machining Ti-6Al-4V. Therefore, this model is excluded from shear localization investigations of this study. Examples could be seen in Figure 4.4.1. Even at very high cutting speeds (120 m/min), no serration has been observed. This is also reported in the work of Calamaz et al. [4], which is attributed to the shortcoming of the J-C relation to model strain-softening effect [4, 49].



a) Johnson and Holmquist [54]



b) Lee and He [42]



c) Lee and He [57]

Figure 4.4.1 Johnson-Cook material model result at a high cutting speed of 120 m/min

To overcome this shortcoming modified J-C material model are proposed by various researchers [4, 47, 49] or damage models are integrated into the J-C constitutive material model [2, 5, 66].

The results of finite element simulations for MJ-C material model proposed by Calamaz et. al [4] for two different d ($d=1$, and $d=1.5$) values are shown in Figure 4.4.2.

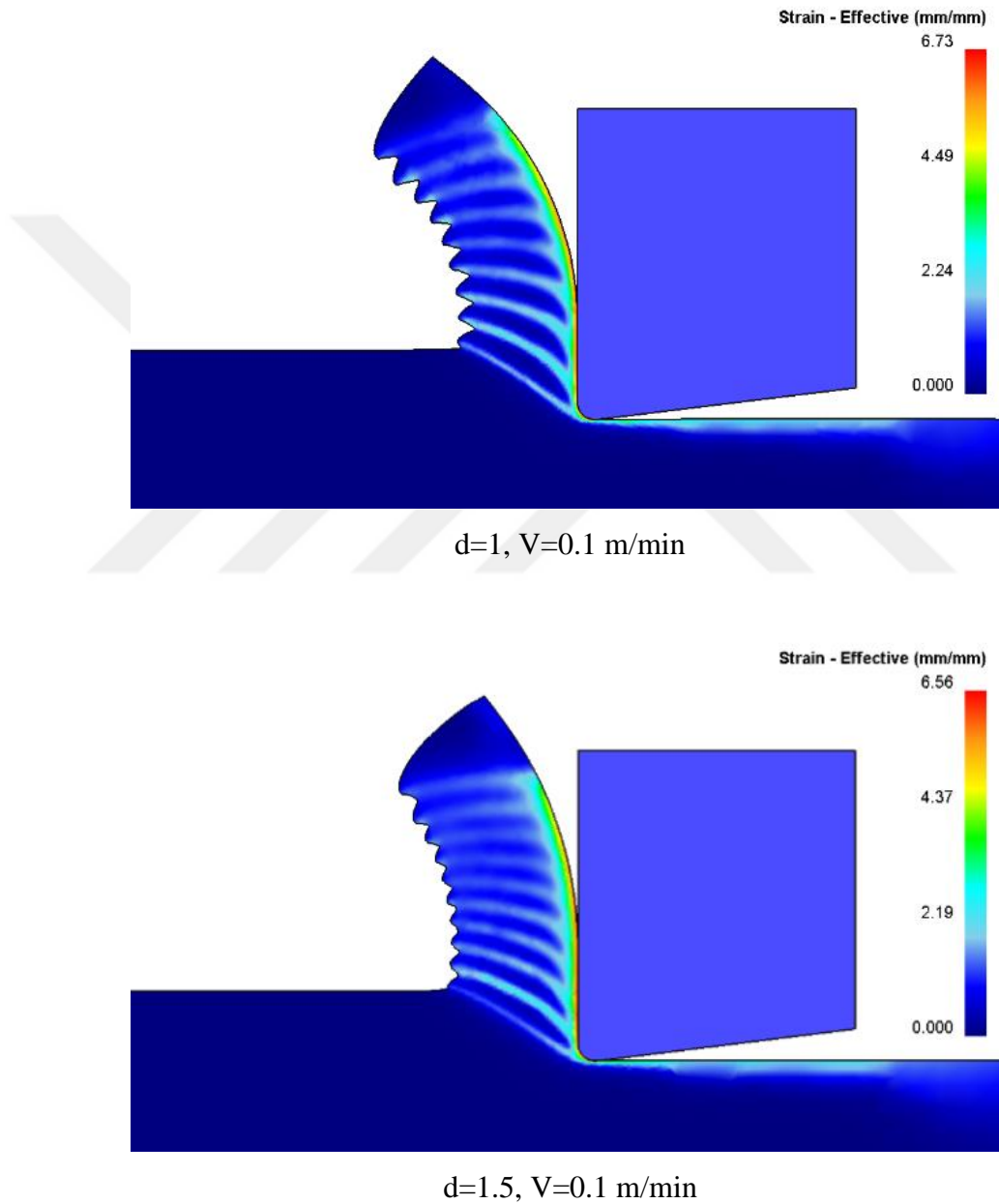


Figure 4.4.2 FEM results using MJ-C model proposed by Calamaz et al. [4]

It can be seen that even at an extremely low cutting speed of 0.1 m/min, the model results in a shear localized chip. So the model proposed by Calamaz et al. [4] is not capable of predicting the onset of shear localization.

The results of the finite element simulations for Sima&Ozel [49] modified models are shown in Figure 4.4.3, Figure 4.4.4 and Figure 4.4.5.

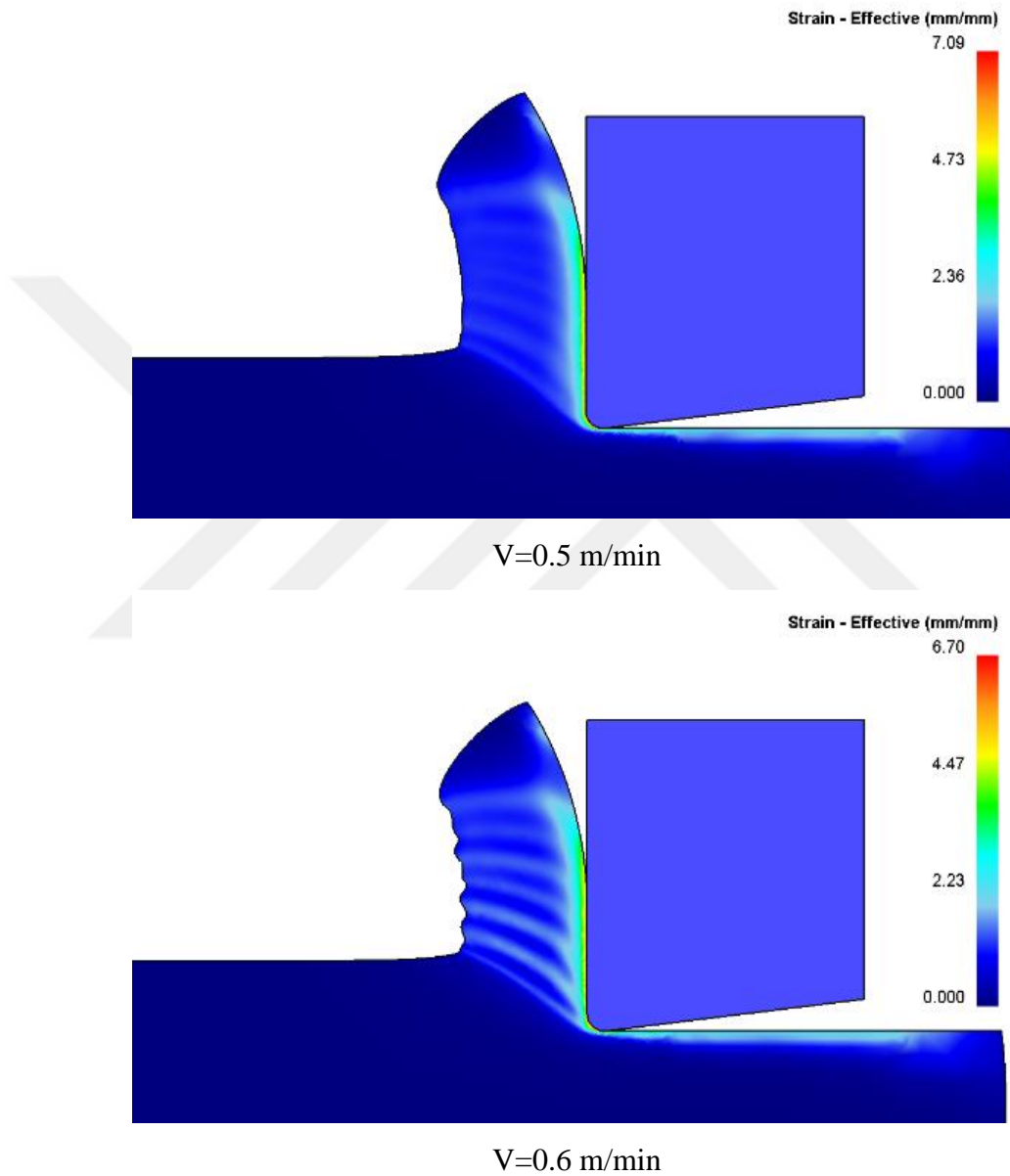
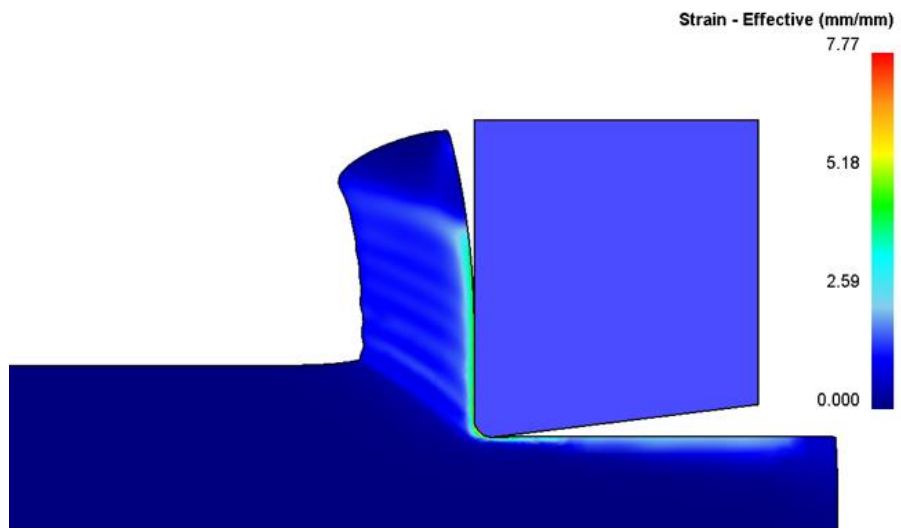
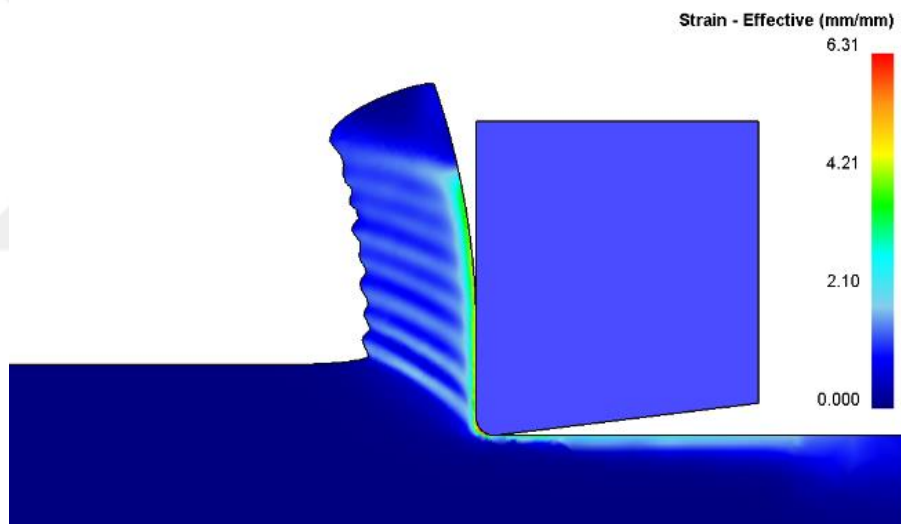


Figure 4.4.3 FEM results using MJ-C model proposed by Sima&Ozel Model I [49]

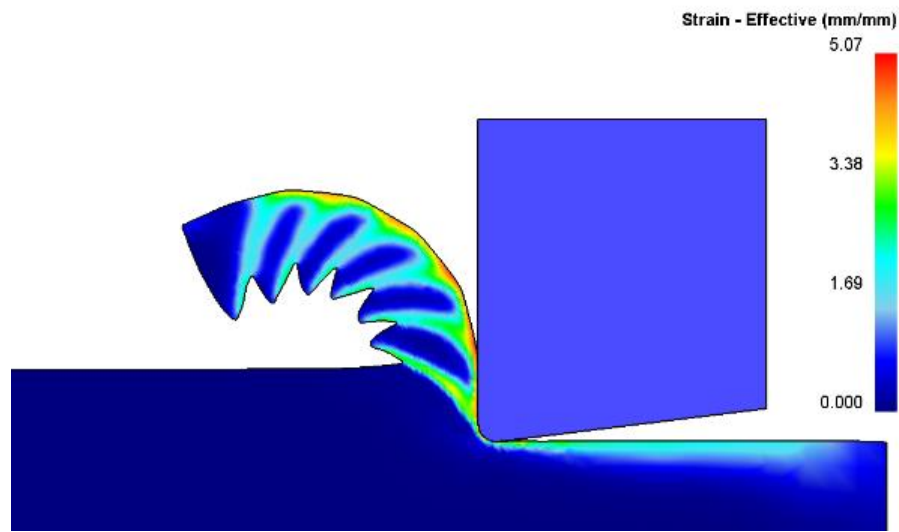


$V=2.7$ m/min



$V=2.8$ m/min

Figure 4.4.4 FEM results using MJ-C model proposed by Sima&Ozel Model II [49]



V=0.1 m/min

Figure 4.4.5 FEM results using MJ-C model proposed by Sima&Ozel Model III [49]. Model I and Model II are shown to be able to predict the shear localization onset. When using Model I a very low cutting speed of 0.5 m/min is obtained for the critical cutting speed, which is too far from the critical cutting speed of 2.82 m/min determined by experiments. Therefore, although Model I shows sensitivity to the variation of cutting speed, its accuracy is very low and is not recommended for the studies related to the prediction of shear localization onset. The Model II reveals a critical cutting speed of 2.7 m/min for the critical cutting speed, which well agrees with the experimental observations. It can be seen that even at a low cutting speed of 0.1 m/min, Model (III) results in a shear localized chip and is not capable to predict shear localization onset.

The results of finite element simulations for the MJ-K model proposed by Karpal [47] is shown in Figure 4.4.6.

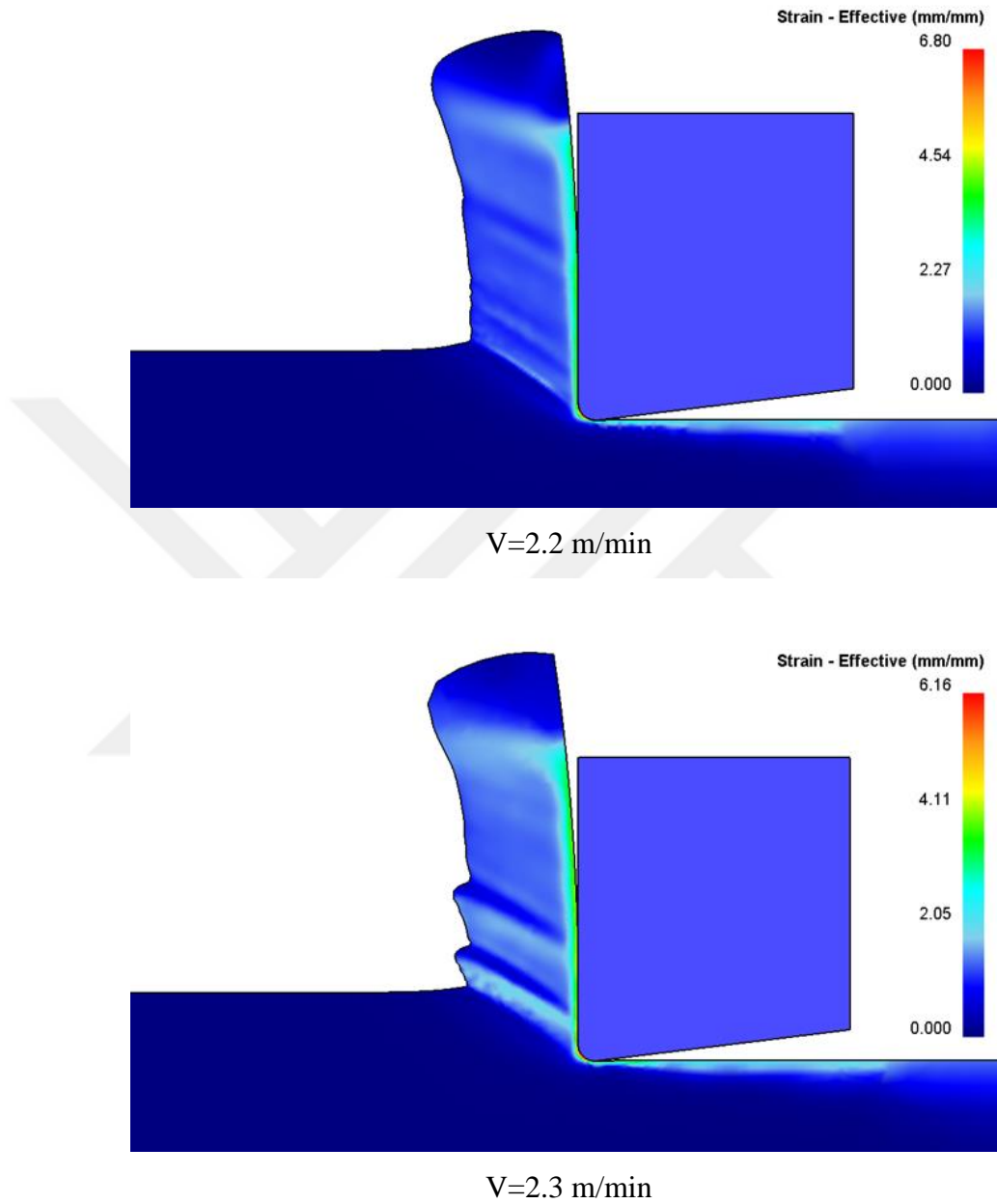
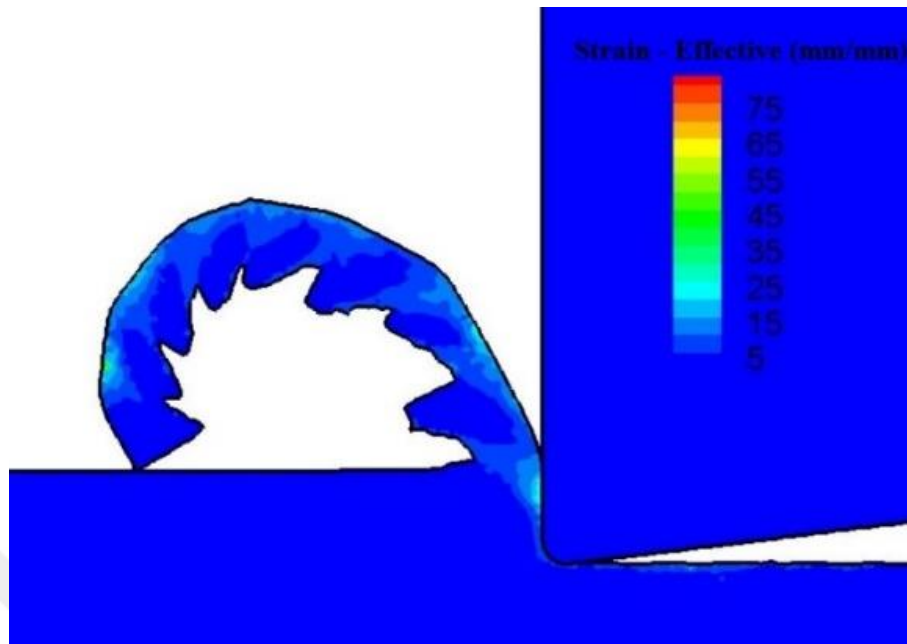


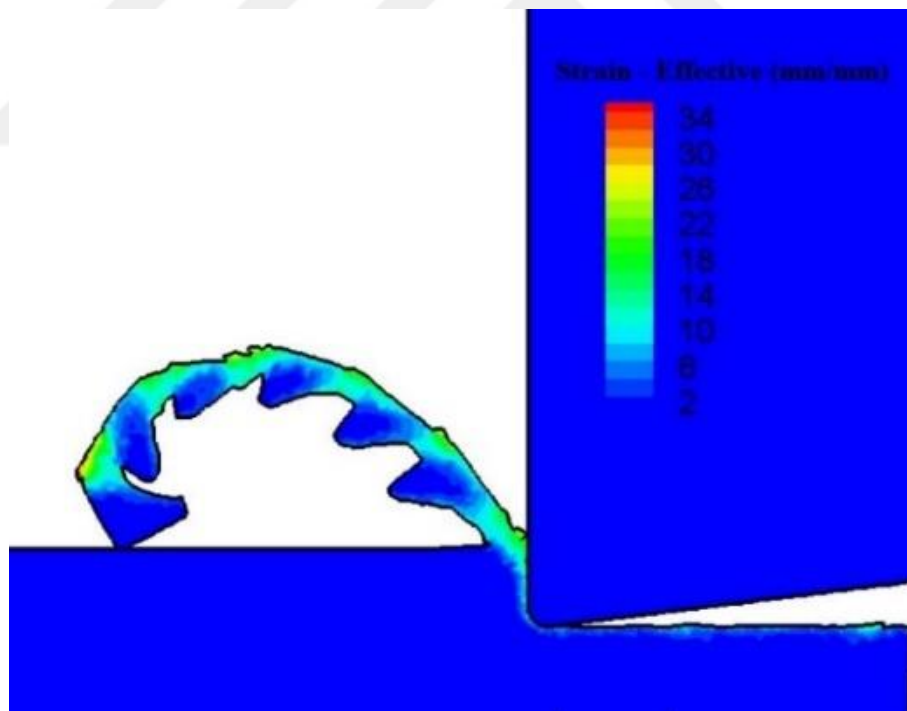
Figure 4.4.6 FEM results using MJ-C model proposed by Karpal [47]

This model predicts a critical cutting speed of 2.2 m/min for the onset of shear localization. A value that is relatively close to the results of experiments.

The results of the finite element analysis for Power-law model with temperature-dependent damage [5] are shown in Figure 4.4.7.



$V=0.1$ m/min



$V=40$ m/min

Figure 4.4.7 FEM results using Power-law material model with temperature-dependent damage: 0.1 and 40 m/min [5]

It can be seen that the model predicts a shear localization at a very low speed of 0.1, which indicates that the model base on power-law strain hardening and power-law

strain rate sensitivity with temperature-dependent damage is not suitable for the prediction of shear localization onset.

The results of the finite element simulations using the J-C material model with two different levels of Cockcroft and Latham (C&L) material failure parameters (90 and 240) are shown in Figure 4.4.8. It can be seen that the model predicts a shear localization at a very low speed of 0.1, which indicates that the J-C model with C&L material failure model is not suitable for the prediction of shear localization onset.

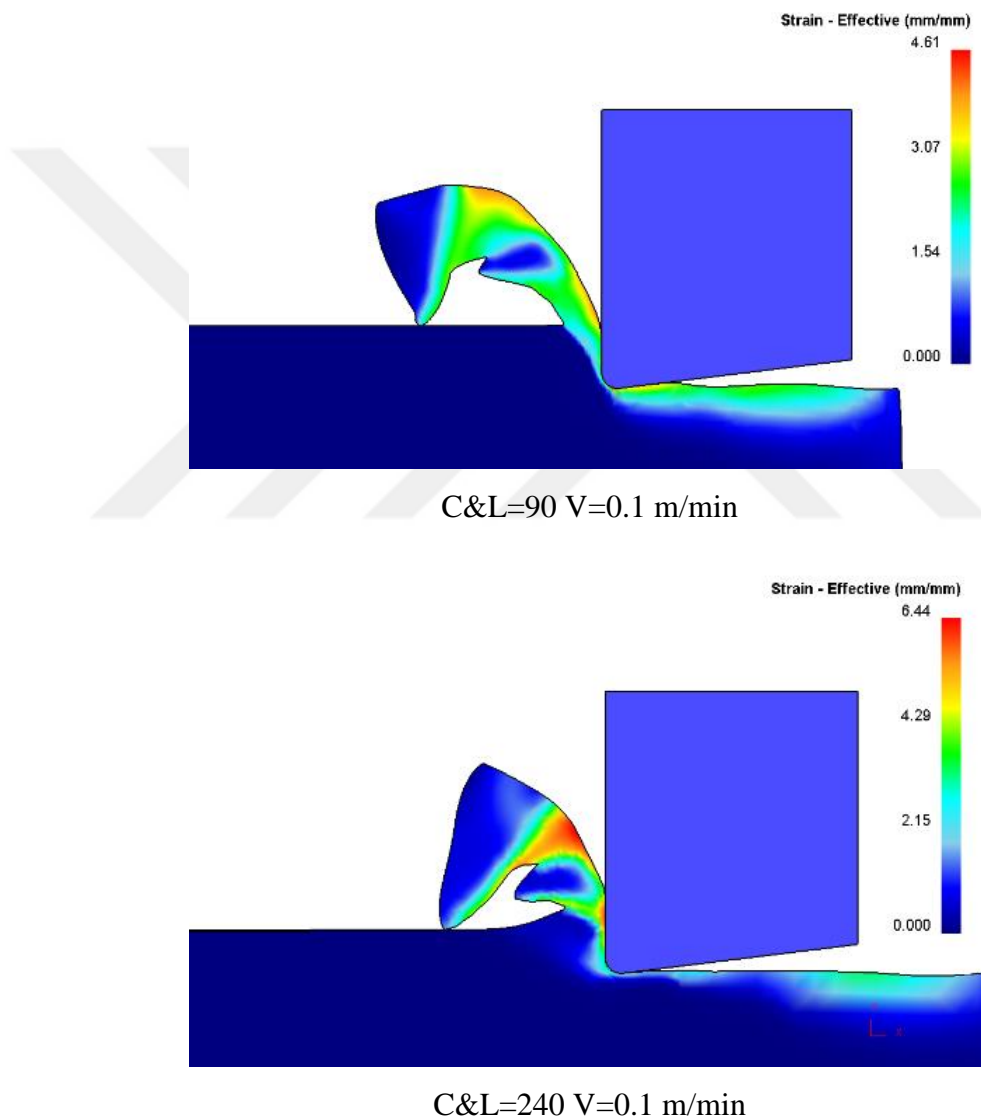
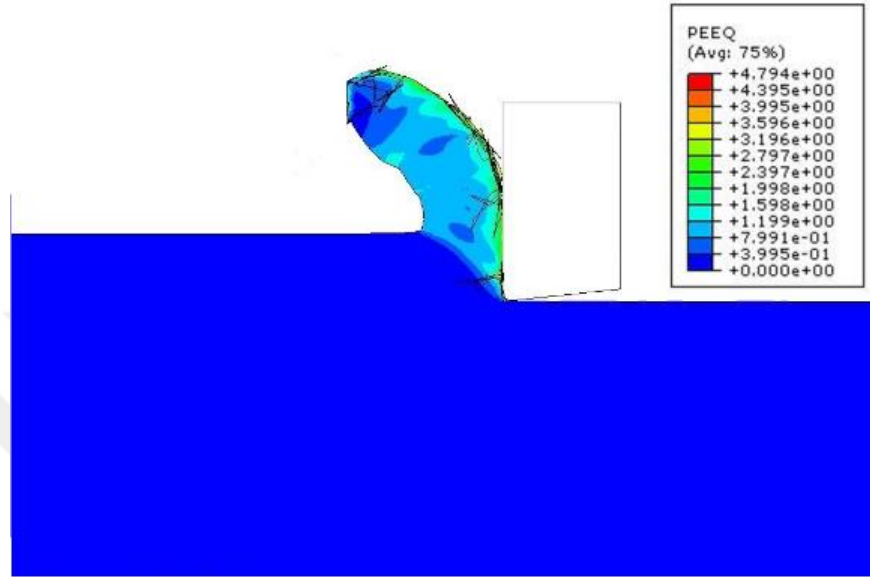


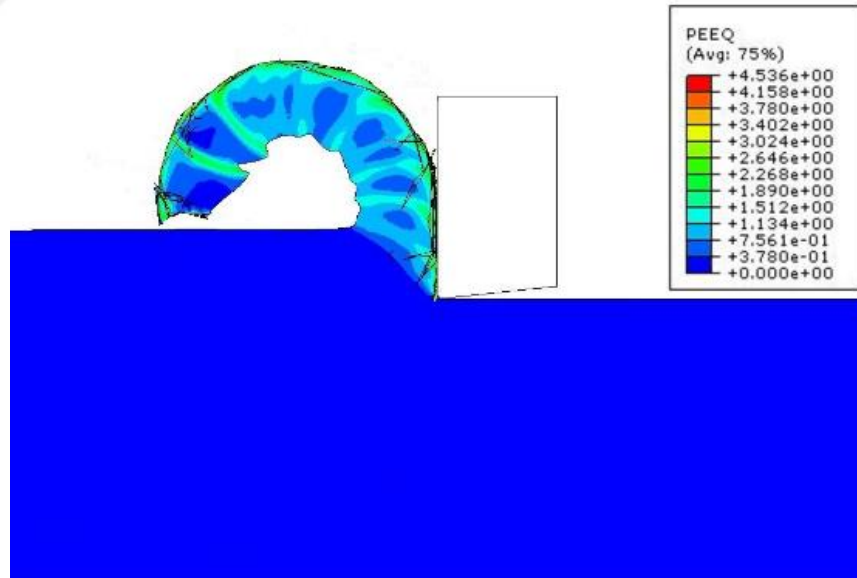
Figure 4.4.8 J-C model with Cockcroft and Latham material failure model result at low cutting speed

The results of FE simulations using J-C material model with J-C damage are shown in Figure 4.4.9. It can be seen that at cutting speed of 3.8 m/min, there is no shear

localization. Therefore, the critical cutting speed for shear localization onset using the J-C Material Model with J-C damage is determined as 3.8 m/min, which shows the capability of the model to predict the onset of shear localization. However, the result is not in a good agreement with the experiments, but still can be used for the studies related to the prediction of shear localization onset.



V=3.8 m/min



V=4 m/min

Figure 4.4.9 Johnson-Cook Material Model with J-C damage results

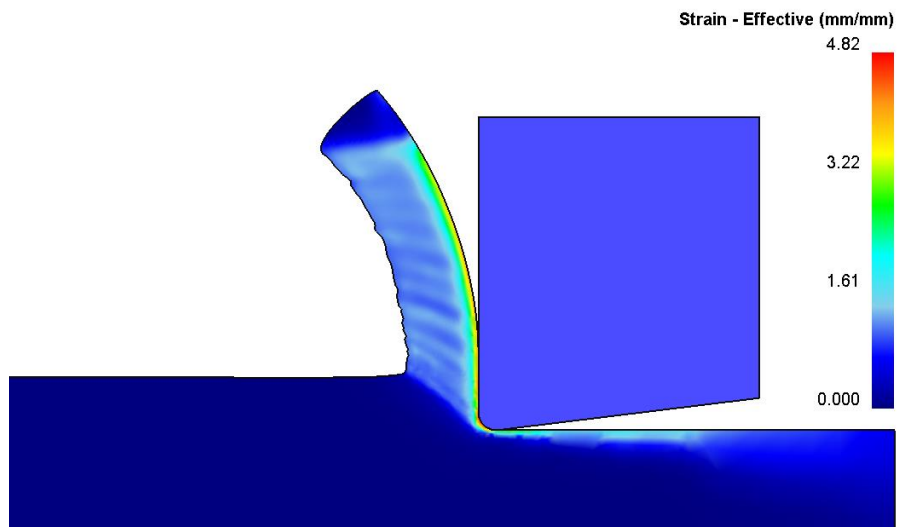
Some of the material models gave the shear localized chips even at extreme low cutting speeds. The shear localization chip formation is hard to model because the shear instability and localization affect the primary shear zone ahead of the tool at first.

It can be seen that not all of the models proposed in the literature to model serrated chip formation are capable of predicting the shear localization onset. When compared with the results of orthogonal cutting experiments the capability and accuracy of different models are summarized in Table 4.4.1.

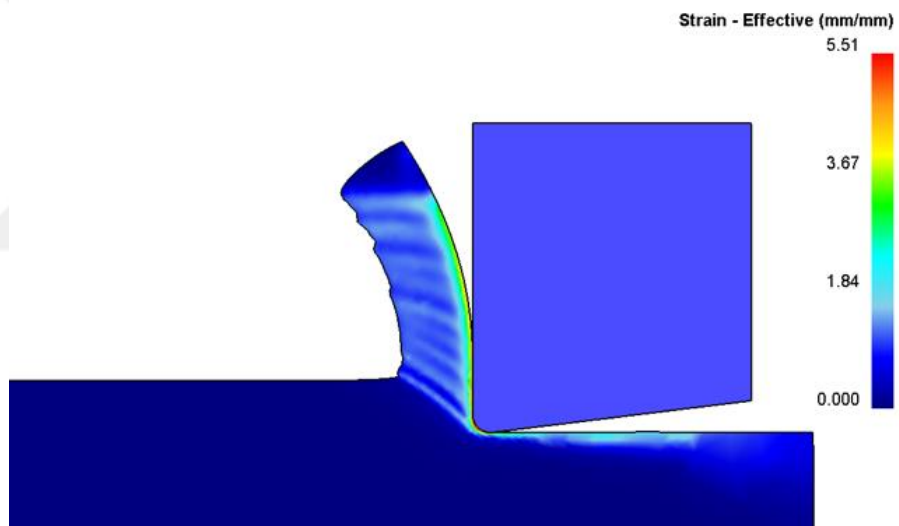
Table 4.4.1 Summary of the capability and accuracy of different constitutive material models

Material Model	The ability to predict shear localization onset	Accuracy
J-C Material Model	✗	N/A
Modified J-C (Calamaz et al.)	✗	N/A
Modified J-C, Sima and Ozel Model (I)	✓	Very Low- Not Acceptable
Modified J-C, Sima and Ozel Model (II)	✓	Very High
Modified J-C, Sima and Ozel Model (III)	✗	N/A
Modified J-C, Karpaz	✓	High
J-C with C&L Damage	✗	N/A
J-C with J-C Damage	✓	Medium- Acceptable

It can be seen that the MJ-C material model II proposed by Sima& Ozel [49] is in a very good agreement with orthogonal cutting experiments. To further analyze the capability of this model to capture the onset of shear localization, simulations are done at two different uncut chip thicknesses of 0.075 mm and 0.125 mm. The results of the simulations are shown in Figure 4.4.10 and Figure 4.4.11. It can be seen that critical cutting speeds of 7.5 m/min and 2.3 m/min are obtained for uncut chip thicknesses of 0.075 and 0.125 mm, respectively. The increase in the critical cutting speed with decreasing uncut chip thickness is reported in the experimental observations of Barry et al. [40].

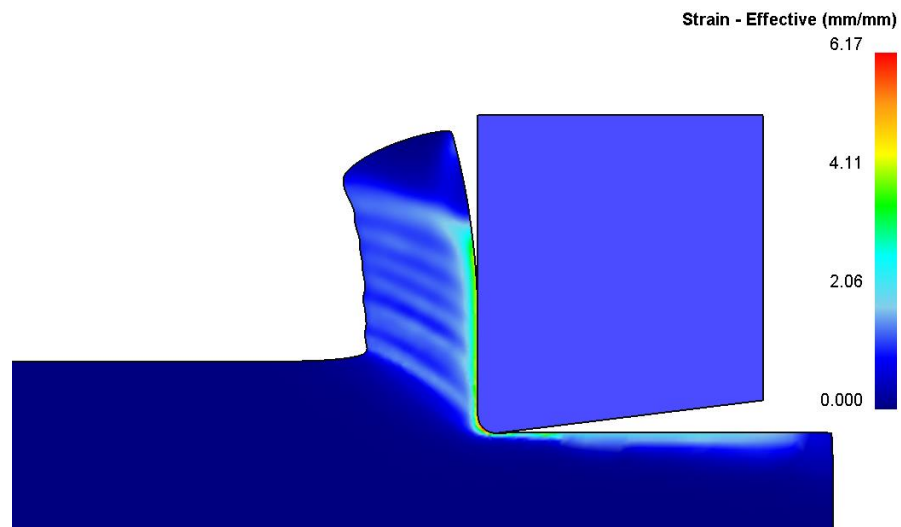


V=7.4 m/min

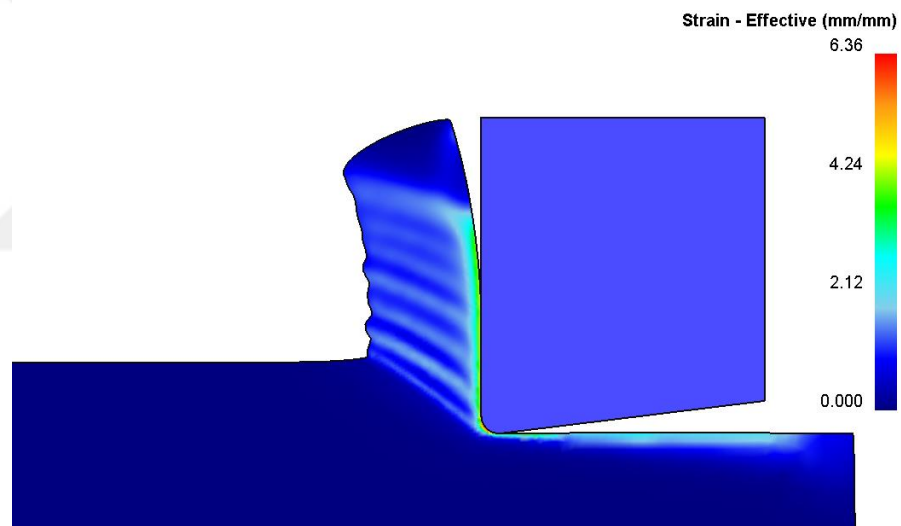


V=7.5 m/min

Figure 4.4.10 The results of FE simulations for different uncut chip thicknesses using MJ-C model proposed by Sima&Ozel model II: Uncut chip thickness of 0.075 mm



V=2.2 m/min

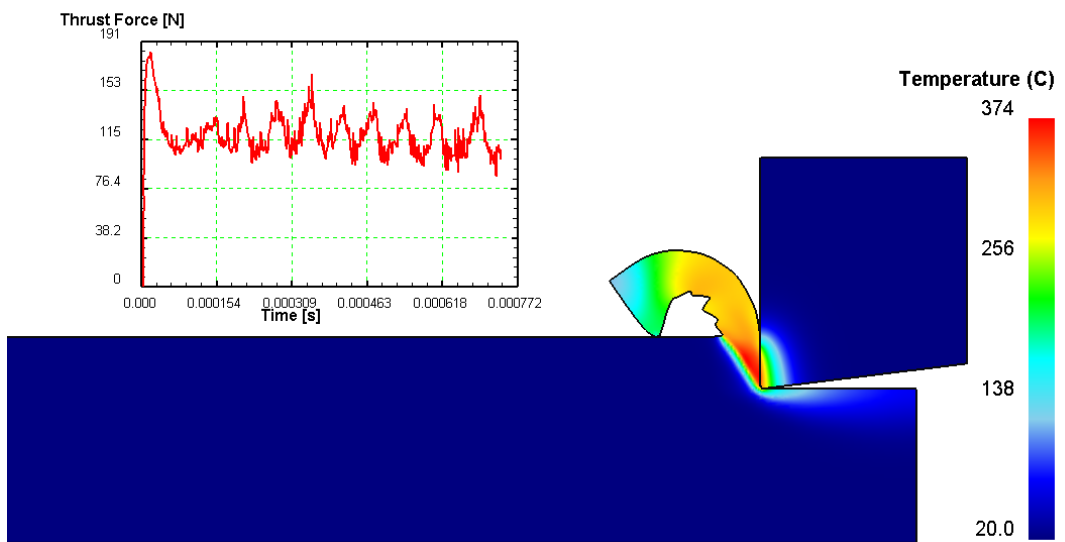
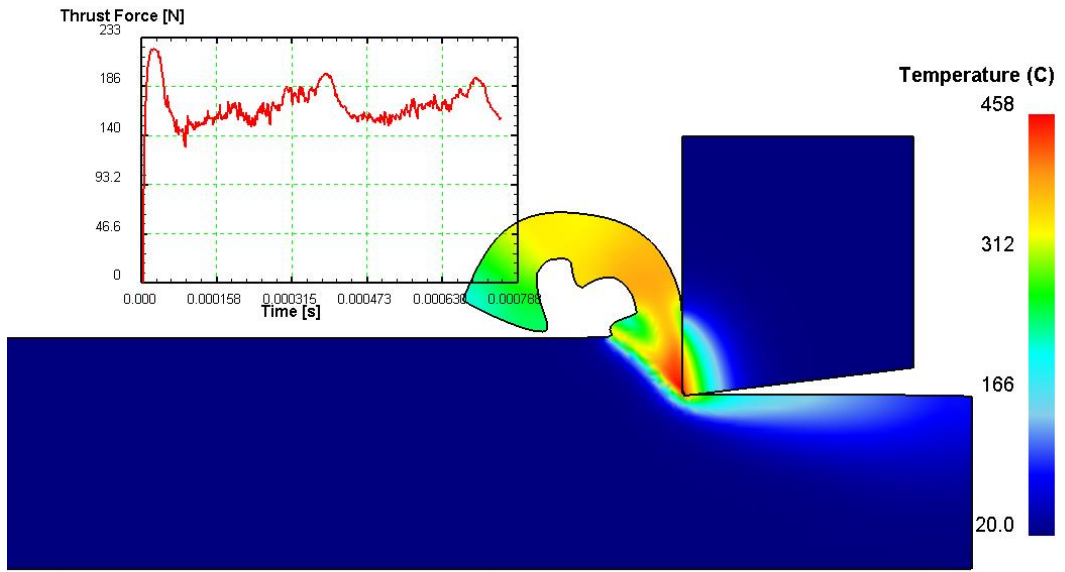


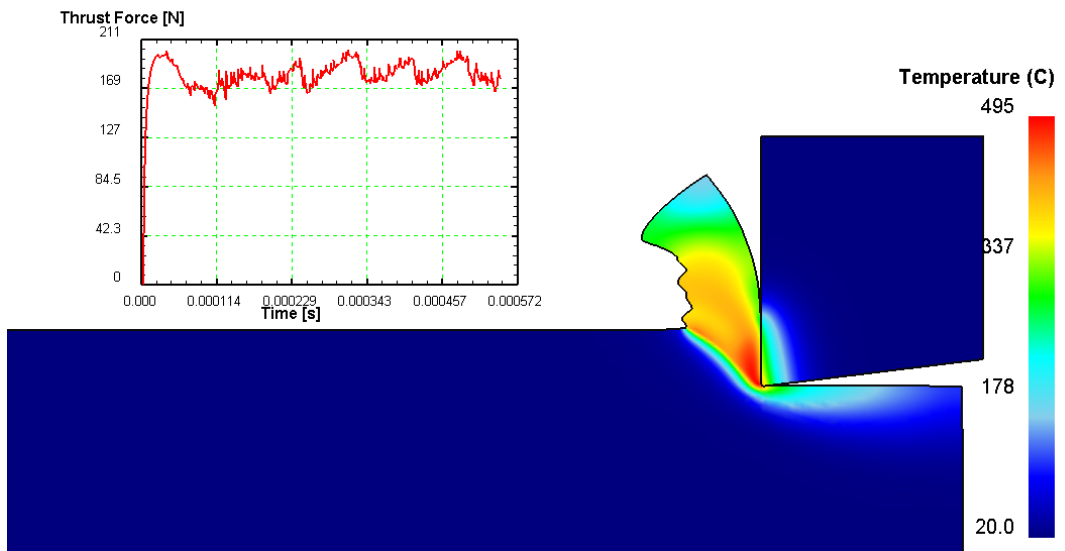
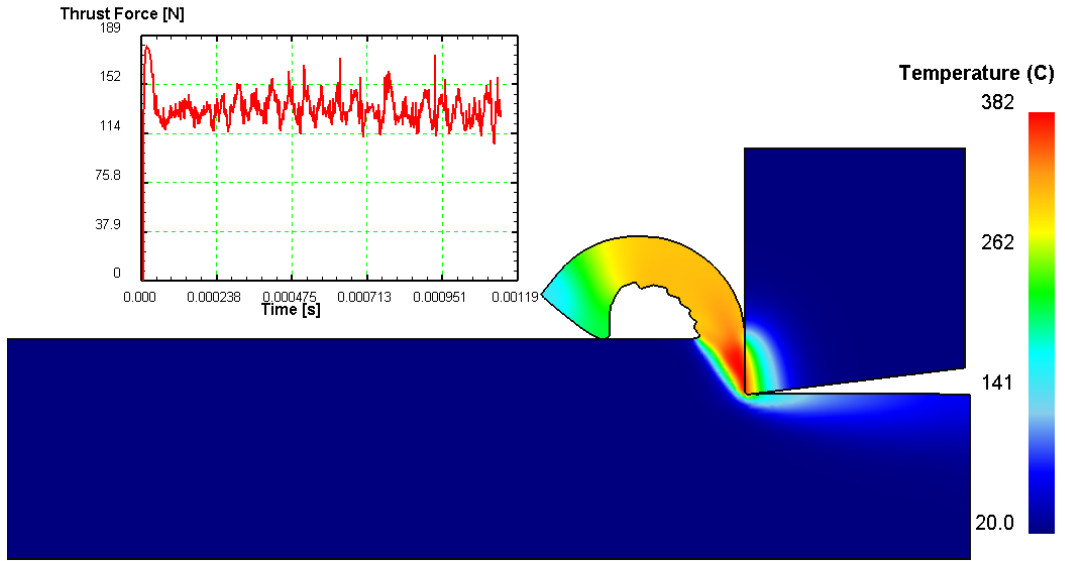
V=2.3 m/min

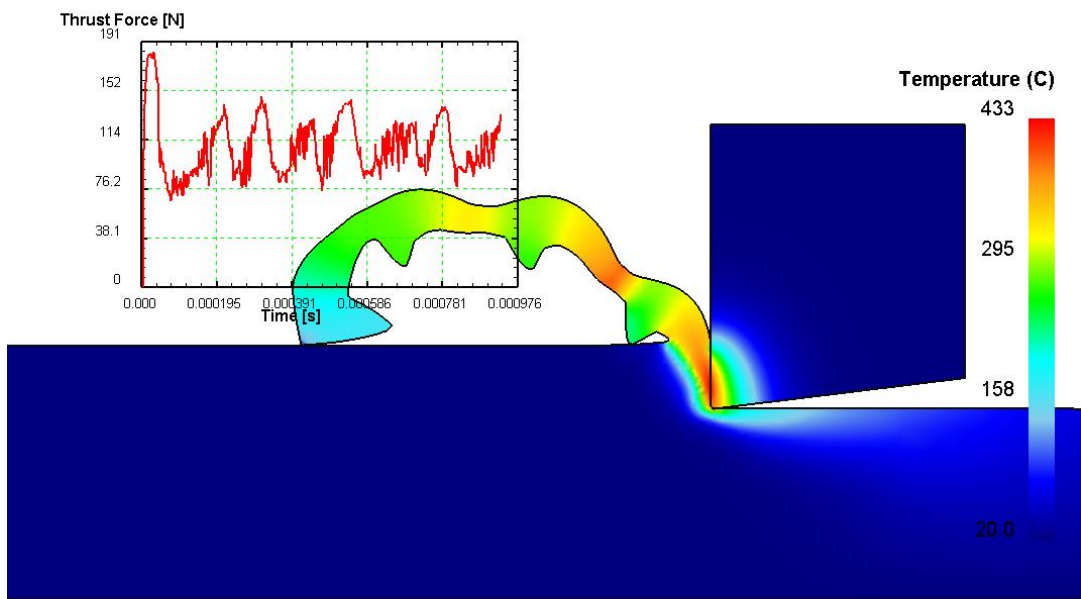
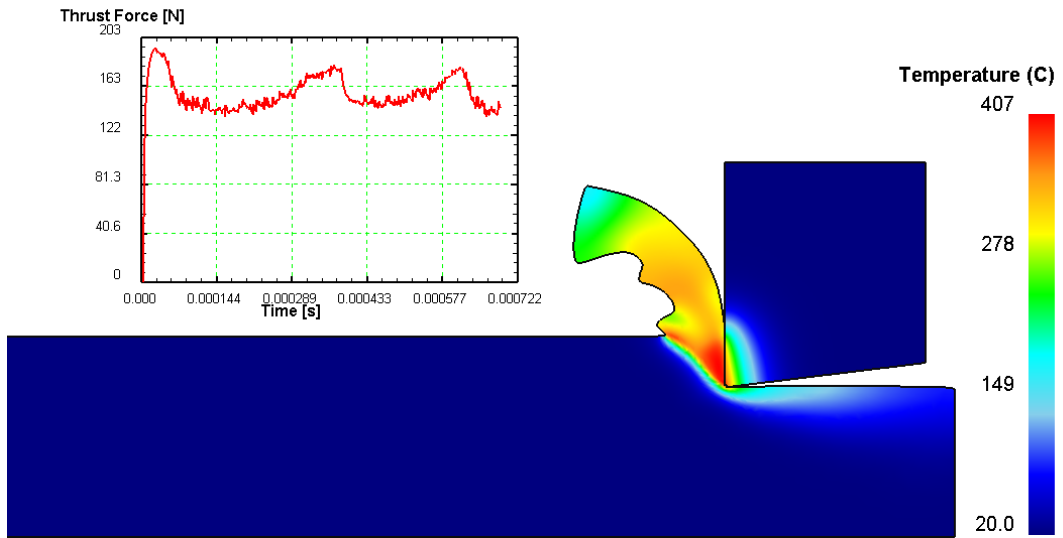
Figure 4.4.11 The results of FE simulations for different uncut chip thicknesses using MJ-C model proposed by Sima&Ozel model II: Uncut chip thickness of 0.125 mm

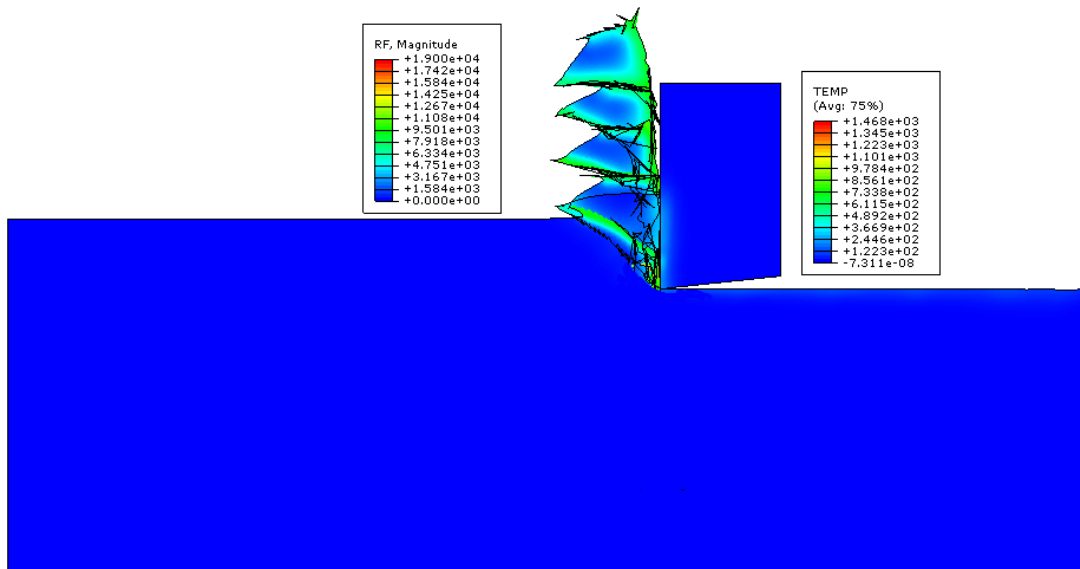
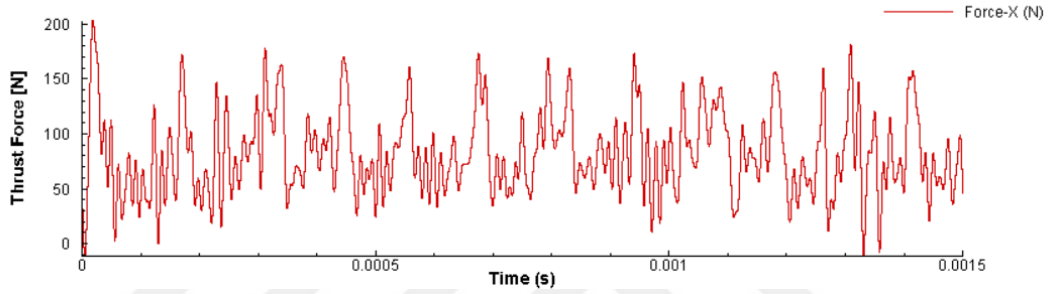
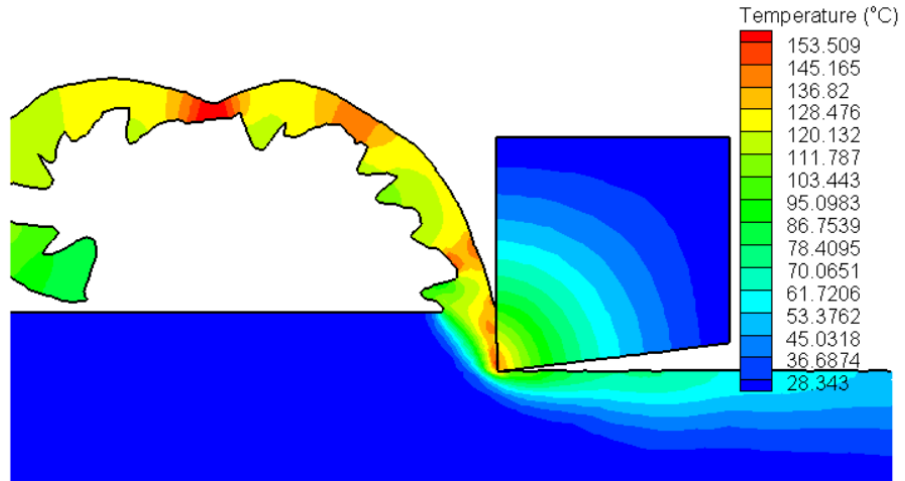
4.5 Temperature and Force Comparison between FEM and Measured Data

The temperature and force distribution graph of shear localization in Ti-6Al-4V alloy machining simulation for 40 m/min cutting speed and 0.1 mm uncut chip thickness with a 0° tool rake angle and $5 \mu\text{m}$ edge radii are shown in Figure 4.5.1. The coefficient of friction is taken 0.41 which is calculated in Chapter 4.3.









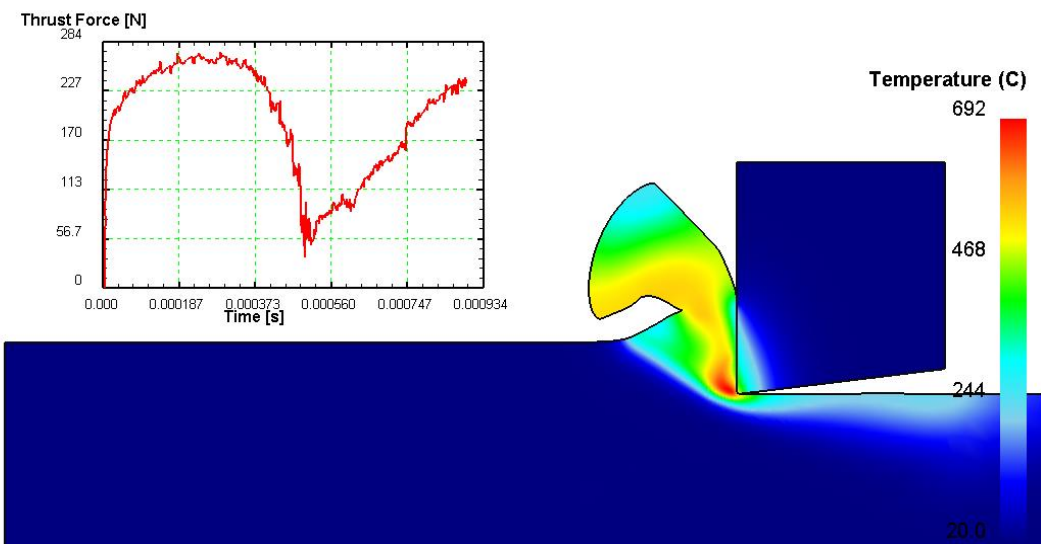
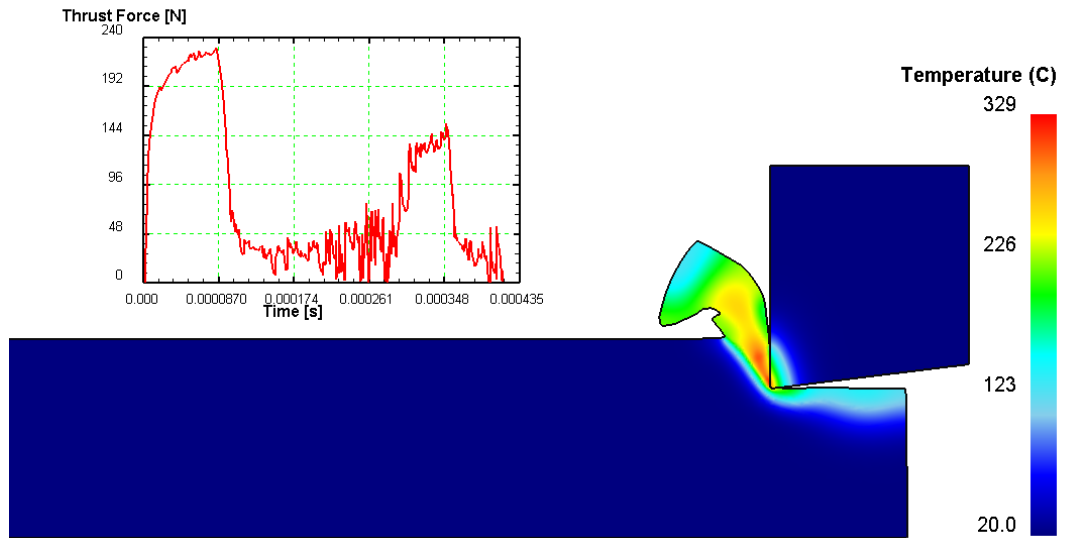


Figure 4.5.1 Temperature and Force Distribution Graph of YK, Calamaz d1, Calamaz d1.5, Ozel Model1, Ozel Model2, Ozel Model3, Power Law, JC-JC Damage, JC C&L90 and JC C&L240 (top to bottom)

Measuring thrust forces during orthogonal cutting experiments allows the investigation of how effective the material model to predict forces. Figure 4.5.2 shows the force measurements obtained from Kistler Dynamometer 9265B+9441B.

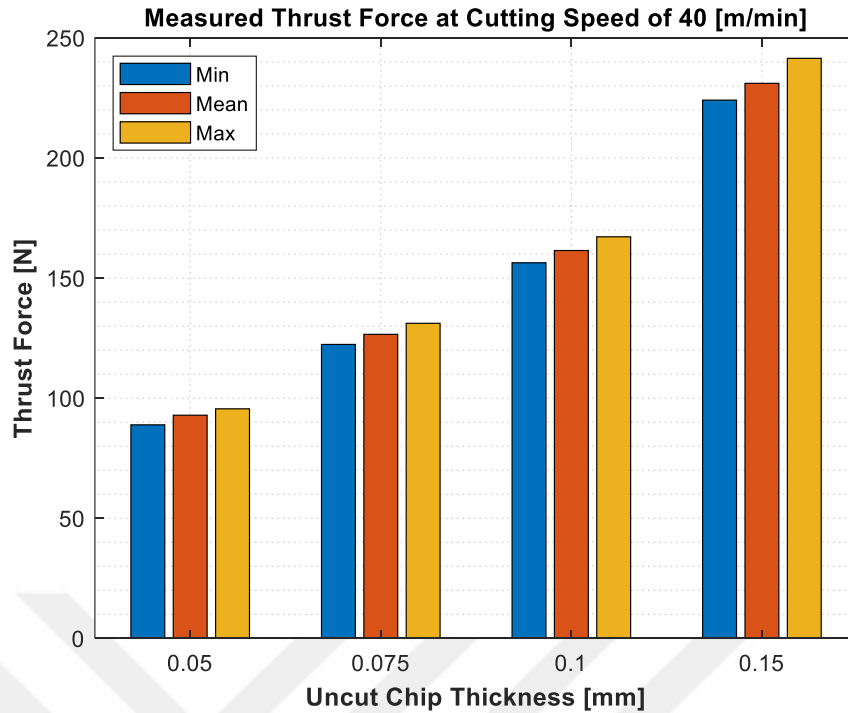


Figure 4.5.2 Measured Thrust Forces at $f=0.1$ mm/rev and $V_c = 40$ m/min with 0° rake, 7° Clearance and 5 micrometer inserts

The measured thrust force was filtered with a low pass filter and average thrust force and its variations around 5.5 Newton. Maximum, mean and minimum thrust forces are measured as 156.4, 161.5 and 167.2 N, respectively. The model proposed by Yigit Karpat [47] and Sima&Ozel model II [49] predict measured thrust force sufficiently. YK and Sima&Ozel model II simulated thrust force are 166.79 N and 155.39 N respectively.

In our orthogonal cutting experiments, we don't have a chance to measure temperature so it is not possible to compare the simulation with the experimental results.

CHAPTER 5

5. CONCLUSION

In this study, the effect of different material models on the prediction of shear localization onset has been studied. The material models under investigations are Johnson-Cook material model, Johnson-Cook material model with Cockcroft and Latham damage model, Johnson-Cook material model Johnson-Cook damage model, models based on modified Johnson-Cook material models with strain softening terms and material model with power-law type strain hardening and strain rate sensitivity, with polynomial thermal softening and polynomial temperature-dependent damage. The results of this study can be summarized as follows:

- The results of orthogonal cutting experiments and SEM observations revealed a critical cutting speed of 2.82 m/min for the shear localization onset when using a cutting tool of 0° rake angle, 7° clearance angle and edge radius of 25 μm for an uncut chip thickness of 0.1 mm.
- Johnson-Cook material model alone cannot be used for shear localization studies using finite element method.
- The results of finite element simulations revealed that three models are capable of predicting the shear localization onset including J-C constitutive material model with J-C damage model and two models based on modified J-C material model with a thermal softening term. Other models are shown to be insensitive to the shear localization onset and they predict a shear localized chips even at a very low cutting speed of 0.1 m/min.
- The J-C constitutive model with J-C type damage model predicts a critical cutting speed of 3.8 m/min for the onset of shear localization, while the model based on modified Johnson-Cook material model with temperature-dependent overarching modifier and temperature-dependent material model parameters (proposed by Sima and Ozel [49]) predicts a critical cutting speed of 2.8 m/min for shear localization onset. Another modified J-C material model with temperature-dependent flow softening behavior (proposed by Karpat [47]) predicts a critical cutting speed of 2.3 m/min for the onset of shear localization. Therefore, based on

the experimental observations, a finite element model that uses a modified Johnson-Cook material model with a temperature-dependent overarching modifier and temperature-dependent material model parameters (proposed by Sima and Ozel [49]) is the suitable model for the prediction of shear localization onset during machining Ti-6Al-4V.

- It has also shown that the critical cutting speed for the onset of shear localization increases with increasing depth of cut.
- Orthogonal cutting experiments are used to record cutting and thrust forces to calculate Coulomb friction coefficients by excluding the effect of ploughing forces using the extrapolation method.
- The cutting force studies have shown that the method of extrapolation to a zero uncut chip thickness can be used for the calculation of the Coulomb friction coefficient. The average Coulomb friction coefficient between titanium alloy and tungsten carbide under dry machining conditions is found as 0.41 by using corrected cutting and thrust force components. The result is in a close agreement with the result of titanium/tungsten carbide pairs under dry sliding conditions using the pin-on-disk method reported in the literature.
- The effectiveness of the aforementioned material models (Karpal [47] and Sima and Ozel Model II [49]) for the prediction of cutting and thrust forces revealed that the results of the models are in an acceptable agreement with the experimental data. However, the model proposed by Sima and Ozel (Model II) [49] revealed the closest results to the experiments.

REFERENCES

- [1] A. O. Tay, M. G. Stevenson, and G. De Vahl Davis, "Using the Finite Element Method to Determine Temperature Distributions in Orthogonal Machining," *Proceedings of the Institution of Mechanical Engineers*, vol. 188, no. 1, pp. 627-638, 1974.
- [2] G. Ye, Y. Chen, S. Xue, and L. Dai, "Critical cutting speed for onset of serrated chip flow in high speed machining," *International Journal of Machine Tools and Manufacture*, vol. 86, pp. 18-33, 2014.
- [3] S. N. B. Oliaei and Y. Karpas, "Built-up edge effects on process outputs of titanium alloy micro milling," *Precision Engineering*, vol. 49, pp. 305-315, 2017.
- [4] M. Calamaz, D. Coupard, and F. Girot, "A new material model for 2D numerical simulation of serrated chip formation when machining titanium alloy Ti-6Al-4V," *International Journal of Machine Tools and Manufacture*, vol. 48, no. 3-4, pp. 275-288, 2008.
- [5] R. Laubscher, G. Styger, and G. Oosthuizen, "A numerical analysis of machining induced residual stresses of grade 5 titanium alloy," 2014.
- [6] X. Xu, J. Zhang, H. Liu, Y. Qi, Z. Liu, and W. Zhao, "Effect of morphological evolution of serrated chips on surface formation during high speed cutting Ti6Al4V," *Procedia CIRP*, vol. 77, pp. 147-150, 2018.
- [7] X. Cui, B. Zhao, F. Jiao, and J. Zheng, "Chip formation and its effects on cutting force, tool temperature, tool stress, and cutting edge wear in high-and ultra-high-speed milling," *The International Journal of Advanced Manufacturing Technology*, vol. 83, no. 1-4, pp. 55-65, 2016.
- [8] E. Ezugwu, J. Bonney, and Y. Yamane, "An overview of the machinability of aeroengine alloys," *Journal of materials processing technology*, vol. 134, no. 2, pp. 233-253, 2003.
- [9] A. Majorell, S. Srivatsa, and R. Picu, "Mechanical behavior of Ti-6Al-4V at high and moderate temperatures—Part I: Experimental results," *Materials Science and Engineering: A*, vol. 326, no. 2, pp. 297-305, 2002.
- [10] A. Vyas and M. Shaw, "Mechanics of saw-tooth chip formation in metal cutting," *Journal of manufacturing science and engineering*, vol. 121, no. 2, pp. 163-172, 1999.
- [11] N. Ueda, T. Matsuo, and K. Uehara, "An analysis of saw-toothed chip formation," *CIRP Annals*, vol. 31, no. 1, pp. 81-84, 1982.
- [12] G. Su, Z. Liu, L. Li, and B. Wang, "Influences of chip serration on micro-topography of machined surface in high-speed cutting," *International Journal of Machine Tools and Manufacture*, vol. 89, pp. 202-207, 2015.

- [13] M. Elbestawi, A. Srivastava, and T. El-Wardany, "A model for chip formation during machining of hardened steel," *CIRP annals*, vol. 45, no. 1, pp. 71-76, 1996.
- [14] B. Li, S. Zhang, Q. Zhang, and L. Li, "Simulated and experimental analysis on serrated chip formation for hard milling process," *Journal of Manufacturing Processes*, vol. 44, pp. 337-348, 2019.
- [15] R. Komanduri and R. Brown, "On the mechanics of chip segmentation in machining," 1981.
- [16] R. Komanduri and Z.-B. Hou, "On thermoplastic shear instability in the machining of a titanium alloy (Ti-6Al-4V)," *Metallurgical and Materials Transactions A*, vol. 33, no. 9, p. 2995, 2002.
- [17] M. A. Davies, Y. Chou, and C. J. Evans, "On chip morphology, tool wear and cutting mechanics in finish hard turning," *CIRP annals*, vol. 45, no. 1, pp. 77-82, 1996.
- [18] R. Komanduri, "Some clarifications on the mechanics of chip formation when machining titanium alloys," *Wear*, vol. 76, no. 1, pp. 15-34, 1982.
- [19] R. Recht, "Catastrophic thermoplastic shear," 1964.
- [20] G. Ye, M. Jiang, S. Xue, W. Ma, and L. Dai, "On the instability of chip flow in high-speed machining," *Mechanics of Materials*, vol. 116, pp. 104-119, 2018.
- [21] B. Wang and Z. Liu, "Evaluation on fracture locus of serrated chip generation with stress triaxiality in high speed machining of Ti6Al4V," *Materials & Design*, vol. 98, pp. 68-78, 2016.
- [22] J. Xie, A. Bayoumi, and H. Zbib, "A study on shear banding in chip formation of orthogonal machining," *International Journal of Machine Tools and Manufacture*, vol. 36, no. 7, pp. 835-847, 1996.
- [23] M. Shaw and A. Vyas, "Chip formation in the machining of hardened steel," *CIRP annals*, vol. 42, no. 1, pp. 29-33, 1993.
- [24] M. G. Cockcroft and D. J. Latham, *A simple criterion of fracture for ductile metals*. 1966.
- [25] E. Ceretti, M. Lucchi, and T. Altan, "FEM simulation of orthogonal cutting: serrated chip formation," *Journal of Materials Processing Technology*, vol. 95, no. 1-3, pp. 17-26, 1999.
- [26] P. Hartley, I. Pillinger, and C. E. Sturgess, *Numerical modelling of material deformation processes: research, development and applications*. Springer Science & Business Media, 2012.
- [27] H. Zhen-Bin and R. Komanduri, "On a thermomechanical model of shear instability in machining," *CIRP annals*, vol. 44, no. 1, pp. 69-73, 1995.

- [28] M. Kassner, M. Wang, M.-T. Perez-Prado, and S. Alhajeri, "Large-strain softening of aluminum in shear at elevated temperature," *Metallurgical and Materials Transactions A*, vol. 33, no. 10, pp. 3145-3153, 2002.
- [29] T. Pettersen and E. Nes, "On the origin of strain softening during deformation of aluminum in torsion to large strains," *Metallurgical and Materials Transactions A*, vol. 34, no. 12, pp. 2727-2736, 2003.
- [30] R. Ding and Z. Guo, "Microstructural evolution of a Ti-6Al-4V alloy during β -phase processing: experimental and simulative investigations," *Materials Science and Engineering: A*, vol. 365, no. 1-2, pp. 172-179, 2004.
- [31] J. Hashemi, A. Tseng, and P. Chou, "Finite element modeling of segmental chip formation in high-speed orthogonal cutting," *Journal of materials engineering and performance*, vol. 3, no. 6, p. 712, 1994.
- [32] T. Obikawa and E. Usui, "Computational machining of titanium alloy—finite element modeling and a few results," 1996.
- [33] W. Rice, "The formation of continuous chips in metal cutting," *Eng J, Englnt of Canada*, vol. 44, pp. 41-45, 1961.
- [34] K. Iwata, K. Osakada, and Y. Terasaka, "Process modeling of orthogonal cutting by the rigid-plastic finite element method," 1984.
- [35] J. Hua and R. Shivpuri, "Prediction of chip morphology and segmentation during the machining of titanium alloys," *Journal of materials processing technology*, vol. 150, no. 1-2, pp. 124-133, 2004.
- [36] D. Owen and M. Vaz Jr, "Computational techniques applied to high-speed machining under adiabatic strain localization conditions," *Computer methods in applied mechanics and engineering*, vol. 171, no. 3-4, pp. 445-461, 1999.
- [37] S. Semiatin and S. Rao, "Shear localization during metal cutting," *Materials Science and Engineering*, vol. 61, no. 2, pp. 185-192, 1983.
- [38] R. Komanduri and B. Von Turkovich, "New observations on the mechanism of chip formation when machining titanium alloys," *Wear*, vol. 69, no. 2, pp. 179-188, 1981.
- [39] A. Molinari, C. Musquar, and G. Sutter, "Adiabatic shear banding in high speed machining of Ti-6Al-4V: experiments and modeling," *International journal of Plasticity*, vol. 18, no. 4, pp. 443-459, 2002.
- [40] J. Barry, G. Byrne, and D. Lennon, "Observations on chip formation and acoustic emission in machining Ti-6Al-4V alloy," *International Journal of Machine Tools and Manufacture*, vol. 41, no. 7, pp. 1055-1070, 2001.
- [41] M. Ribeiro, M. Moreira, and J. Ferreira, "Optimization of titanium alloy (6Al-4V) machining," *Journal of materials processing technology*, vol. 143, pp. 458-463, 2003.

- [42] W.-S. Lee and C.-F. Lin, "High-temperature deformation behaviour of Ti6Al4V alloy evaluated by high strain-rate compression tests," *Journal of Materials Processing Technology*, vol. 75, no. 1-3, pp. 127-136, 1998.
- [43] J. Pérez, J. Llorente, and J. Sanchez, "Advanced cutting conditions for the milling of aeronautical alloys," *Journal of Materials Processing Technology*, vol. 100, no. 1-3, pp. 1-11, 2000.
- [44] K. Maekawa, T. Shirakashi, and T. Obikawa, "Recent progress of computer aided simulation of chip flow and tool damage in metal machining," *Proceedings of the Institution of Mechanical Engineers, Part B: Journal of Engineering Manufacture*, vol. 210, no. 3, pp. 233-242, 1996.
- [45] M. Bäker, J. Rösler, and C. Siemers, "A finite element model of high speed metal cutting with adiabatic shearing," *Computers & Structures*, vol. 80, no. 5-6, pp. 495-513, 2002.
- [46] D. Sandstrom and J. Hodowany, "Modeling the physics of metal cutting in high-speed machining," *Machining Science and Technology*, vol. 2, no. 2, pp. 343-353, 1998.
- [47] Y. Karpát, "A modified material model for the finite element simulation of machining titanium alloy Ti-6Al-4V," *Machining Science and Technology*, vol. 14, no. 3, pp. 390-410, 2010.
- [48] Y. Karpát, "Temperature dependent flow softening of titanium alloy Ti6Al4V: An investigation using finite element simulation of machining," *Journal of Materials Processing Technology*, vol. 211, no. 4, pp. 737-749, 2011.
- [49] M. Sima and T. Özel, "Modified material constitutive models for serrated chip formation simulations and experimental validation in machining of titanium alloy Ti-6Al-4V," *International Journal of Machine Tools and Manufacture*, vol. 50, no. 11, pp. 943-960, 2010.
- [50] S. N. B. Oliaei and Y. Karpát, "Investigating the influence of friction conditions on finite element simulation of microscale machining with the presence of built-up edge," *The International Journal of Advanced Manufacturing Technology*, vol. 90, no. 1-4, pp. 819-829, 2017.
- [51] J. C. Outeiro, D. Umbrello, R. M'Saoubi, and I. Jawahir, "Evaluation of present numerical models for predicting metal cutting performance and residual stresses," *Machining Science and Technology*, vol. 19, no. 2, pp. 183-216, 2015.
- [52] J. Fleischer, J. Schmidt, L. Xie, C. Schmidt, and F. Biesinger, "2D tool wear estimation using finite element method," in *Proc. of the 7th CIRP International Workshop on Modeling of Machining Operations*, 2004, pp. 82-91.
- [53] Y.-C. Yen, A. Jain, and T. Altan, "A finite element analysis of orthogonal machining using different tool edge geometries," *Journal of materials processing technology*, vol. 146, no. 1, pp. 72-81, 2004.

- [54] G. Johnson and T. Holmquist, "Test data and computational strength and fracture model constants for 23 materials subjected to large strains, high strain rates, and high temperatures," *Los Alamos National Laboratory, Los Alamos, NM, Report No. LA-11463-MS*, 1989.
- [55] W.-S. Lee and C.-F. Lin, "Plastic deformation and fracture behaviour of Ti–6Al–4V alloy loaded with high strain rate under various temperatures," *Materials Science and Engineering: A*, vol. 241, no. 1-2, pp. 48-59, 1998.
- [56] R. Shivpuri, J. Hua, P. Mittal, A. Srivastava, and G. Lahoti, "Microstructure-mechanics interactions in modeling chip segmentation during titanium machining," *CIRP Annals*, vol. 51, no. 1, pp. 71-74, 2002.
- [57] L. Li and N. He, "A FEA study on mechanisms of saw-tooth chip deformation in high speed cutting of Ti–6–Al–4V alloy," in *Fifth international conference on high speed machining (HSM), Metz, France*, 2006, vol. 14, p. 16.
- [58] T. Özel and E. Zeren, "Determination of work material flow stress and friction for FEA of machining using orthogonal cutting tests," *Journal of Materials Processing Technology*, vol. 153, pp. 1019-1025, 2004.
- [59] K. Gregory, "Failure modeling of titanium 6Al-4V and aluminum 2024-T3 with the Johnson-cook material model," *Department of Transportation Federal Aviation Administration*, 2003.
- [60] S. Seo, O. Min, and H. Yang, "Constitutive equation for Ti–6Al–4V at high temperatures measured using the SHPB technique," *International journal of impact engineering*, vol. 31, no. 6, pp. 735-754, 2005.
- [61] M. Calamaz, D. Coupard, M. Nouari, and F. Girot, "Numerical analysis of chip formation and shear localisation processes in machining the Ti-6Al-4V titanium alloy," *The International Journal of Advanced Manufacturing Technology*, vol. 52, no. 9-12, pp. 887-895, 2011.
- [62] R. Whirley, B. Engelmann, and J. Hallquist, "'A nonlinear, explicit, two dimensional finite element code for solid mechanics', User Manual UCRL-MA-110630, Lawrence Livermore National Laboratory, CA, USA."
- [63] G. Chen, C. Ren, X. Qin, and J. Li, "Temperature dependent work hardening in Ti–6Al–4V alloy over large temperature and strain rate ranges: Experiments and constitutive modeling," *Materials & Design*, vol. 83, pp. 598-610, 2015.
- [64] Y. Guo and Y. Chou, "The determination of ploughing force and its influence on material properties in metal cutting," *Journal of Materials Processing Technology*, vol. 148, no. 3, pp. 368-375, 2004.
- [65] Q. Niu, X. Zheng, W. Ming, and M. Chen, "Friction and wear performance of titanium alloys against tungsten carbide under dry sliding and water lubrication," *Tribology Transactions*, vol. 56, no. 1, pp. 101-108, 2013.

[66] B. Wang and Z. Liu, "Shear localization sensitivity analysis for Johnson–Cook constitutive parameters on serrated chips in high speed machining of Ti6Al4V," *Simulation Modelling Practice and Theory*, vol. 55, pp. 63-76, 2015.

